

Approval Sheet

This thesis/dissertation/report entitled **Quantum Biomimetic Electronic Nose Sensors** by Ms. Nidhi Pandey is approved for the degree of **Doctor of Philosophy (PhD)**.

Examiners

Mr. Siva Rama Krishna.



Supervisor (s)

Swaroop Ganguly

Chairperson

R. N. D.

Date: 7-8-2024

Place: Mumbai

Abstract

The origin of smell of small hydrophobic volatile organic molecules is not completely understood to the highest level of scientific explanation and prediction. The smell of a molecule cannot be predicted and similarly the structure of a smell. Better understanding of mapping molecular structure to smell and vice versa, is required for designing sensitive, selective and robust sensors.

This thesis can be seen as a combination of three parts, which put together, try to look at the problem of artificial olfaction. The first idea is of odor classification based on their vibrational spectra. This is based on the proposition of Vibrational theory of olfaction, which says that nose recognizes odorant's vibrational spectra through Inelastic Electron Tunneling Spectroscopy (IETS). Chemical Graph Theory is used to connect the vibrational spectrum of an odorant molecule, invoked in the Vibration Theory of Olfaction, to its structure, which is germane to the orthodox Shape Theory. Atomistic simulations yield the Eigen-VValue (EVA) vibrational pseudo-spectra for 20 odorant molecules grouped into 6 different 'perceptual' classes by odour. The EVA is decomposed into peaks corresponding to different *types* of vibrational modes. A novel secondary pseudo-spectrum, informed by this physical insight – the Peak-Decomposed EVA (PD-EVA) – has been proposed here. Unsupervised Machine Learning (spectral clustering), applied to the PD-EVA, clusters the odours into different physical (vibrational) classes that match the perceptual. This establishes a physical basis for vibration-based odour classification, harmonizes the Shape and Vibration theories, and points to vibration-based sensing as a promising path towards a biomimetic electronic nose.

In second part, theory of enantioselective selection in biological systems through Chirality induced spin selectivity is combined with IETS to propose an idea for enantioselective E-nose sensor. With inclusion of spin in charge polarization the electron phonon coupling in IETS gets modified and generates different signal for the pair of enantiomers. In the last part, a real-world application of EN nose sensors, around the freshness detection of Mango, is explored with the help of actual olfactory receptor-based devices. Silicon nanowire (SiNW) based FET was used as a transducer for this use-case. The popularity of SiNW based biosensors was exploited for the purpose to reach a proof-of concept. This thesis tries to understand olfaction from scientific as well as technological point-of -view.

Nobody ever figures out what life is all about, and **it doesn't matter..**

-Richard Feynman

List of Publications

1. N. Pandey, S. Sahoo, S. Ganguly, “Graph theoretic unification of Vibration and Shape theories of olfaction,” Workshop on Quantum Effects in Biological Systems, 2018.
2. S. Sahoo, N. Pandey, S. Ganguly, “Atomistic Modeling of Inelastic Tunneling through Odorant Molecules,” Workshop on Quantum Effects in Biological Systems 2018.
3. S. Sahoo, N. Pandey, S. Ganguly, “Atomistic Design of Quantum Biomimetic Electronic Nose,” 2018 International Conference on Simulation of Semiconductor Processes and Devices (SISPAD), Austin, Texas, USA, 2018.
4. S. Sahoo, N. Pandey, D. Saha, S. Ganguly, “Atomistic Design of Receptor Structure in Quantum Biomimetic Electronic Nose Sensors,” 2018 IEEE Sensors, New Delhi, India, 2018. doi: [10.1109/ICSENS.2018.8589712](https://doi.org/10.1109/ICSENS.2018.8589712)
5. N. Pandey, D. Pal, D. Saha, and S. Ganguly, “Vibration-based biomimetic odor classification” *Sci Rep* vol. 11, no. 11389, 2021.
6. N. Pandey, A. Saha, D. Saha and S. Ganguly, Origin of Spin Polarization in 2-d chiral channel, Joint-MMM Intermag, IEEE, 2022.
7. Digital odour detection and synthesis in the offing, Research Matters, 17 May 2022.
8. Deep learning techniques to understand molecular basis of odor (in preparation).
9. N. Pandey, A. Samal, A. Saha and S. Ganguly, “Artificial Receptor Design for enantioselective E-nose sensor,” Workshop on Quantum Effects in Biological Systems 2022.
10. N. Pandey, A. Samal, A. Saha and S. Ganguly, “Enantioselectivity from Inelastic Electron Tunnelling through a Chiral Sensor,” *J. Phys. D: Appl. Phys.* **57** 285401, 2024 DOI [10.1088/1361-6463/ad3bc4](https://doi.org/10.1088/1361-6463/ad3bc4)
11. N. Pandey, S. Ganguly, “Olfactory Receptor based freshness sensors for *Mangifera Indica* (mango)” (in preparation).

Contents

Acknowledgement	iv
List of Figures	vi
List of Abbreviation	xi
1. Introduction	1
2. Olfaction, biology and beyond	5
2.1 The Olfactory Space	5
2.1.1 The 'lock and key model	6
2.1.2 The odotope theory	8
2.1.3 The vibration theory	8
2.2 Biological background	9
2.2.1 Olfactory Epithelium	10
2.2.2 Olfactory Receptors	10
2.3 Turin's Model	14
3. The physical picture of molecules and Density Functional Theory	16
3.1 Vibration	16
3.1.1 The Born-Oppenheimer Approximation	17
3.1.2 Harmonic Oscillator	19
3.1.3 Quantum Oscillator	20
3.2 Vibrations in small molecules	22
3.2.1 Linear Homo-diatomc	22
3.2.2 Poly-atomics	25
3.3 Vibrational modes of a molecule and Chemical Graph Theory	28
3.3.1 Molecular Graph	28
3.3.2 Adjacency Matrix	29
3.3.3 Degree Matrix	29
3.3.4. Laplacian Matrix	30
3.3.5 Dynamical Matrix and Molecular Vibrational Spectrum	30
3.4 Density Functional Theory	32
3.4.1 The Schrodinger Equation	32
3.4.2 The Hohenburg-Kohn Theorems	36
3.4.3 Approximation for Exchange-Correlation	39
4. Molecular Vibrations, Olfaction and Machine Learning	42
4.1 Algorithm for Odor Recognition	43

4.2 Thermal broadening	48
4.3 Unsupervised Machine Learning: Odor Classification	51
4.4 Results and Analysis	53
4.5 Conclusion.....	56
4.6 Appendix	57
5. Chirality Induced Spin Selectivity (CISS).....	63
5.1 Chiral molecules	63
5.1.1 Manifestation of chirality	64
5.1.2 Chirality Induced Spin Selectivity (CISS).....	65
5.1.3 Rashba SOC.....	66
5.1.4 SOI as a phase.....	70
5.2 Intermolecular Forces.....	72
5.2.1 Types of Intermolecular Energies.....	72
5.2.2 Rayleigh Schrodinger Perturbation Theory	73
5.2.3 Symmetrized RS Approach	78
5.2.4 Levels of SAPT	79
5.2.5 SAPTO.....	80
5.2.6 Other SAPT Levels.....	81
6. Non-Equilibrium Green's function and Inelastic Electron Tunneling Spectroscopy	
82	
6.1 Non-Equilibrium Green's function (NEGF)	82
6.1.1 Coherent and Incoherent Transport	85
6.2 Inelastic Electron Tunnelling Spectroscopy.....	86
6.2.1 Electron-Phonon coupling	88
6.2.2 Transmission with phonon under SCBA.....	94
7. Enantioselective Olfaction within the Vibration Theory	98
7.1 Molecular Interaction and Spin Polarization	99
7.2 Combining Spin selectivity and IETS.....	103
7.2.1 Result and Analysis	104
7.3 Conclusion.....	110
7.4 Appendix	110
8. Towards Application: Identification of Volatile Organic Compounds for quantifying the freshness of Mangoes	113
8.1 Motivation	114
8.2 VOC Profiling and -Bio-active components of Mangifera Indica- Literature Review	115
8.3 Biorecognition Element and Bio-reception	117
8.3.1 Homology Modeling	119

8.3.2 Binding Energy and Prediction of Docking Site	120
8.3.3 Results and Analysis.....	121
8.3.4 Interaction Fingerprinting.....	124
8.4 Relation of physicochemical properties of molecules with their binding score	126
8.5 Sensor Design.....	128
8.5.1 Device Design.....	128
8.5.2 Peptide as Sensing material	129
8.5.3 Computational Methodology.....	131
8.5.4 Electrostatic Potential	131
8.5.4 Transport Calculations	133
8.6 Conclusion.....	136
9. Conclusion and Future Work	138

Acknowledgement

First and foremost, I would like to extend my gratitude to my supervisor, Prof. Swaroop Ganguly, for his invaluable contribution, unwavering support, and patience during this journey. His immense knowledge and experience have encouraged me in my academic research and life. His active interest in my research made the journey exciting and helped me through difficult times. I owe him a special thanks for his support during one of the most trying times of my life.

I express my deepest appreciation to the members of my Research Progress Committee, Prof. Dipankar Saha, Prof. Bhakararn Murlidharan, and Prof. Debasattam Pal, for their suggestions, extensive knowledge, and invaluable insights.

I would also like to thank all the students, Ashutosh Samal, Abhijeet Verma, and Kirti Aggarwal, who worked with me on various projects during this journey. I would also like to thank all my colleagues and lab mates for sharing their experiences and knowledge with me from time to time. Special mention goes to my best friend and IIT Bombay alumnus Tanmay Chavan for his constant support and help.

I express my sincere thanks to University Grants Commission (UGC) for providing the much-needed financial support through Junior and Senior Research Fellowship (JRF, SRF). I would also like to extend my gratitude towards Ministry of Electronics and Information Technology, Department of Science and Technology, Government of India, for providing the required funding through Nanoelectronics Network for Research and Applications (*NNetRA*).

To the people in my life outside of the nano-world who have graciously and humorously shared my odd obsession at times. To my family; my parents (both sets of parents), sister, brother, and my extended family; for how they have helped me in everything, ceaselessly and for all their advice and tolerance. My life is incomplete without my parents' contribution, for

they have moulded me into the person I am today. I hope to become half the person they think I am. My sister and brother-in-law, a new addition to our family, Vrishank, have comforted me and held my hand through the ups and downs. Last but no least, to my husband, Dr. Basant Saini, for understanding and supporting me in every possible way and amazing me every step of the way.

Nidhi Pandey

List of Figures

Figure 2.1: Furan (left) and thiofuran (right) are similar in shape but have a different smells. Furan smells like roasted coffee, whereas thiofuran has a hint of benzene. [24]	6
Figure 2.2: Benzaldehyde (left) and hydrogen cyanide (right) are different structurally but smell similar (smell like rotten almond) [24].	7
Figure 2.3: The unpredictability of smell, a few examples of molecules with different structure, and smell depicting the complexity of perceptual and physicochemical space of olfaction. [24]	7
Figure 2.4: The biological olfactory system showing the odorant's journey from (a) the nasal cavity [33] to (b) the olfactory epithelium [34] to (c) the olfactory sensory neuron [35] and finally to (d) the receptor [36].	9
Figure 2.5: Structure showing the seven trans-membranes alpha helices with an exterior and interior region. E and C are extracellular and intracellular loops.	11
Figure 2.6: The organization of inputs from odorant receptor, present in the olfactory epithelium (OE), to the olfactory bulb (OB), olfactory cortex (OC). Inputs from different ORs are separated in different neurons and glomeruli in the OE and OB. [30].....	12
Figure 2.7: Combinatorial code generated by receptors for different odorants. [30].....	13
Figure 2.8: The receptor takes electrons from NAPDH. When odorant interacts with the receptor the disulphide bond breaks after oxidation and G-protein gets released [26].	15
Figure 3.1: Energy diagram of a classical Simple Harmonic Oscillator.	20
Figure 3.2: Energy diagram of a quantum Harmonic Oscillator.	21
Figure 3.3: A 1-dimensional linear harmonic oscillator.....	23
Figure 3.4: Normal Mode Displacement.....	25
Figure 3.5: Molecule as a network of harmonic Oscillator	30
Figure 3.6: A representation of the relationship between interacting many-body system (left-hand side) and the non-interacting system of Kohn Sham density functional theory (right-hand side).....	39
Figure 4.1: 20 odorant molecules belonging to 6 different perceptual classes are first selected, including Benzene in the <i>Aromatic</i> class (left, centre). The Laplacian Matrix (left bottom), a mathematical description of the structure, is shown (for Benzene here) to be proportional to the Dynamical Matrix \mathbf{D} (right, bottom) – which describes the equation of vibrational motion of a molecule in terms of coupled oscillators. This mapping harmonizes the Vibrational and Shape theories of Olfaction. The eigen-frequencies of the Dynamical Matrix lead to a vibrational spectrum – the Peak-Decomposed EigenValue (PD-EVA) – with peaks corresponding to different vibrational mode types, demarcated by frequency ranges (right, centre) – shown here for Benzene. <i>Clustering</i> based on <i>Similarity</i> in the odorants' PD-EVA leads to the same classes as perceptual, with the revelation of subclasses within <i>Garlicky</i> and <i>Aromatic</i> . This mapping suggests that vibration-based odour sensing and classification may have the potential to emulate the power of biological olfaction.....	43
Figure 4.2: The flowchart for the calculation of the molecular vibrational spectra from the Dynamical Matrix in QuantumATK.....	46
Figure 4.3: EVA plot obtained from convolution of Gaussian function.	49
Figure 4.4 (a): The ‘EigenValue’ (EVA) pseudo-spectrum for the molecule Furan (shown in inset), constructed by broadening the calculated vibrational peaks (stems in red) with Gaussian functions (in blue) of suitable σ (here 100cm^{-1}) and summing up the contributions from all of them at each frequency point. (b): The EVA pseudospectrum, of Furan Methanethiol (inset) as an example, with the partitioning of the frequency scale by types of vibrational modes. From left to right: Torsional modes, Ring Torsion and C-H rocking, Ring Deformation, C-H wagging, C-C stretch, C=C stretch, C=O stretch, S-H stretch, C-H stretch. Similar broad classification of modes can be done so the entire convolved EVA spectra can be deconvolved into broad peaks to identify the regions. This suggests the classification of odorant molecules by broad separation of the vibrational spectrum into	49

these regions, accomplished through the ‘peak-decomposed EVA’.	(c): Peak Decomposition of the EVA spectrum of Furan (shown in inset).	(d): Construction of the Peak-Decomposed EVA (PD-EVA) spectrum by following the same procedure as for EVA (illustrated in Fig. 4.4(a)).....	50
Figure 4.5: The flowchart explains the process of clustering used to classify the odorant molecules based on their PD-EVA pseudo-spectra.....			52
Figure 4.6: the clusters obtained in spectral clustering. The molecules in same cluster have similar smell.....			55
Figure 5.1: The splitting of energy of up-spin and down spin electrons due to chirality of the channel and choosing the direction of propagation.....			69
Figure 5.2: (a) shows the 2d channel with γ as onsite energy, (b) field used to probe the chirality of the channel			71
Figure 5.3: Spin Polarization in chiral channel (spin polarity gets reversed on reversing the chirality of channel).....			72
Figure 6.1: In the NEGF-based quantum transport model, Hamiltonian matrix [H] describes the channel, the self-energy matrices $[\Sigma]$ and the connection between the channel and contacts, and $[\Sigma_0]$ describes interactions inside the channel.....			83
Figure 6.2: Quantum treatment of filling and emptying a channel in a device with a channel and two reservoirs.....			85
Figure 6.3: Schematic illustration of phonon-assisted tunneling in the two-probe molecular junction system. An electron incoming from the left lead emits a phonon (quantized molecular vibrational mode) in the molecular junction and propagates to the right lead with lower energy.			87
Figure 6.4: Schematic I-V, G-V, and IETS-V curves are shown with the existence of electron-phonon coupling. A delta-function peak in the dG/dV curve results from the conductance suddenly increasing as the phonon-assisted transport process becomes viable (the step-function increase only occurs at zero-temperature conditions and will be smoothed out at finite temperature).			89
Figure 6.5: Flow chart for DFT-NEGF-SCBA self-consistent cycle. Electron self-energies due to the phonons are calculated from the electron Green’s functions from the previous self-consistent cycle.			95
Figure 7.1: (a) The splitting of energy of up-spin and down spin electrons due to chirality of the channel vis a vis the direction of propagation. (b) (i) The illustration shows how two molecules with the same handedness interact via generated dipoles. The same spin is polarised in both molecules as charge q moves from one side to the other of the molecule, as shown by the red ball and black arrow. Due to the opposite spin polarization of the electron density that was left behind, the interaction between the molecules is therefore defined by two opposite spins, as seen by the singlet region in the dotted circle. (ii) When two molecules are interacting and have opposing chiralities, their interaction is characterized by two spins that are parallel to one another (in the dotted circle triplet region) [87]..			101
Figure 7.2: The two enantiomers of Limonene molecule are R-(+)-Limonene and (S)-(-)-Limonene. R-(+)-Limonene: This is found naturally in rind of oranges and has a pleasant, orange-like odor. S-(-)-Limonene: This is found in lemon peels and has a harsh turpentine-like odor with lemon note. [89]			102
Figure 7.3: Carvone: The two enantiomers of Carvone molecule are (R)-(-)-Carvone and (S)-(+)-Carvone. (R)-(-)-Carvone: It is extracted from spearmint leaves and smells like spearmint. (S)-(+)-Carvone: It is extracted from caraway seeds and smells like caraway. [90]			102
Figure 7.4: The plots of the values of exchange-dispersion energy for (a) limonene (obtained from SAPTO simulation) and (b) carvone, as the function of intermolecular distance. The blue curve in these plots show similar spin interaction (SS component of exchange-dispersion energy), which is equivalent to the interaction between enantiomers of opposite handedness. Meanwhile, the orange curve indicates the opposite spin interaction (OS component of exchange-dispersion energy), which is equivalent to the interaction between enantiomers of same handedness.			103
Figure 7.5: Simulation set-up with source, drain and channel. The channel is chiral and the odorant molecule is also chiral.....			104

Figure 7.6: The plots of the values of derivative of exchange-dispersion energy with coordinate for (a) limonene (obtained from SAPT0 simulation) and (b) carvoneas the function of intermolecular distance (absolute value). The blue curve in these plots show similar spin interaction (SS component of exchange-dispersion energy), which is equivalent to the interaction between enantiomers of opposite handedness. Meanwhile, the orange curve indicates the opposite spin interaction (OS component of exchange-dispersion energy), which is equivalent to the interaction between enantiomers of same handedness.	106
Figure 7.7: The Current vs Voltage plot showing the current through the sensor when no foreign molecule (odorant) is there, when a foreign molecule of different handedness interacts (black curve) and when a foreign molecule of same handedness interacts (red curve).	108
Figure 7.8: The double derivative of Current vs Voltage plot showing the current through the sensor when a foreign molecule of different handedness interacts (black curve) and when a foreign molecule of same handedness interacts (red curve).	108
Figure 7.9: The contour plot shows the IETS peak spin polarization index as function of electron-phonon coupling for similar handed molecules vs opposite handed molecules (a) The point on contour plot shows maximum enantioselectivity. Receptor is L and odorant is L. (b) This point shows minimum enantioselectivity. Receptor is L and odorant is R or Receptor is R and odorant is L. (c) The point on contour plot shows maximum enantioselectivity. Receptor is R and odorant is R.	109
Figure 7.10: Alignment of the Receptor (peptide) and R-(+)-Limonene3.3.2	112
Figure 7.11: Exchange-dispersion Energy Plot for Receptor-Odorant Interaction	112
Figure 8.1: Identification of VOCs for measuring the quality of fruits or vegetables.	115
Figure 8.2: Class of compounds emitted by different cultivars of Mangifera Indica [96]	116
Figure 8.3: Schematic of a biosensor	117
Figure 8.4: Response of Drosophila to 5 different fruits [94]	118
Figure 8.5: Schematic of flow of steps in Homology Modeling	119
Figure 8.6: Predicted 3-D structures of (a) Or98a and (b) Or19a from Alphafold database.....	120
Figure 8.7: The binding site as identified by AutoDock	121
Figure 8.8: (a) Plot of Variance Vs principle components. PC1 comprises of almost 87% variance in the data. (b) Loadings of PC1, the cut-off for the 16 x 25 matrix comes out to be 0.2. All the points above 0.2 dominate the response of this matrix.	123
Figure 8.9: (a) 16 molecules visualized in the 2-D space of PC1 vs PC2 . (b)The hierarchical clustering of molecules with respect to PC1.....	124
Figure 8.10: (a) Correlation of the binding score of ligand and Or2a with molecular volume and (b) lipophilicity of ligands.	127
Figure 8.11: ATK-VNL view of SiNW-FET composed of source, drain, and channel. The source and drain are doped with n-type dopants. Silicon—yellow; hydrogen—white	129
Figure 8.12: Peptide obtained from Or2a receptor around the binding pocket. Peptide is build in the builder of UCSF Chimera.	130
The generated peptide is then docked with VOC (3-carene) in AutoDock VINA. The peptide was placed on the silicon and geometry optimization was performed before generating the electronic transport properties for the developed sensor.....	131
Figure 8.15: Electrostatic Potential difference from left electrode to the right electrode (z-direction) for pristine SiNW.....	132
Figure 8.16: (a) Electrostatic Potential difference from left electrode to the right electrode (z-direction) for peptide on top of SiNW. (b) Electrostatic Potential difference from left electrode to the right electrode (z-direction) for docked peptide on top of SiNW. (c) Electrostatic Potential difference from left electrode to the right electrode (z-direction) for peptide (black) and docked peptide (red) on top of SiNW.....	133
Figure 8.17: The current (log I) -voltage plot of the SiNW nano-transistor for three different cases, pristine SiNW, SiNW with peptide and SiNW with VOC docked-peptide.	135

Figure 8.18: The conductance ($\log G$) -voltage plot of the SiNW nano-transistor for three different cases, pristine SiNW, SiNW with peptide and SiNW with VOC docked-peptide..... 136

List of Tables

Table 4.1: Set of odorant molecules used in this study, showing their structure, and perceptual (odour) class – namely, Aromatic, Roasted Coffee, Moth Ball, Fruity, Musk and Garlicky [54].	44
Table 4.2: Vibrational Spectrum of Benzene	46
Table 4.3: Vibrational Spectrum of Allicin (data available for select modes only)	47
Table 4.4: Set of initial odorant molecules used in this study, showing their structure, and perceptual (odour) class – namely, Aromatic, Roasted Coffee, Moth Ball, Musk and Garlicky	53
Table 4.5: Molecules with their Perceptual classes and the dominant vibrational modes (in cm ⁻¹) identified by peak-decomposition of EVA pseudo-spectrum. A, B: Low-frequency torsional modes. C, D: Ring torsion and C-H rocking. E, F: Ring deformation, C-H wagging, and C-C stretch. G: C=C stretch. H: C=O stretch. I: S-H stretch. J: C-H stretch.	56
Table 4.6: Molecular structure of all 20 molecules with their EVA and peak decomposition (for generating PD-EVA)	58
Table 8.1: VOC profile of mangoes	116
Table 8.2: Protein- peptide based biosensors for VOC detection [101]	119
Table 8.3: The Binding Map obtained in AutoDock VINA, each OR of drosophila was docked with all the 16 molecules from VOC profile of MI.....	122
Table 8.4 Types of Interaction in AutoDock VINA	125
Table 8.5 Interaction Fingerprint of Or2a receptor with 16 odorant molecules, the rows are the molecules of VOC profile of MI and columns represent the binding pocket of OR2.....	125
Table 8.6 Molecular weight, Volume and hydrophobicity of molecules in VOC profile of MI	126
Table 8.7: Correlation values of the binding score of ligand and ORs with molecular volume (right) and lipophilicity of ligands (left). The values in red show low correlation	127

List of Abbreviation

VTO	Vibrational Theory of Olfaction
IETS	Inelastic Electron Tunnelling Spectroscopy
EN	Electronic Nose
MOS	Metal Oxide Semiconductor
NIR	Near Infrared
OBP	Odorant Binding Protein
OSN	Olfactory Sensory Neuron
cAMP	Cyclic Adenosine Monophosphate
CNG	Cyclic Nucleotide Gated
GPCR	G-protein Coupled Receptor
PDB	Protein Data Bank
OE	Olfactory Epithelium
OC	Olfactory Cortex
OB	Olfactory Bulb
NADPH	Nicotinamide Adenine Dinucleotide Phosphates
DFT	Density Functional Theory
LDA	Local Density Approximation
GGA	Generalised Gradient Approximation
QSAR	Quantitative Structure-Activity Relation
EVA	EigenVAlue
PD-EVA	Peak-Decomposed EigenVAlue
CISS	Chirality Induced Spin Selectivity
SOC	Spin-orbit Coupling
SOI	Spin-orbit Interaction
SAPT	Symmetry Adapted Perturbation Theory
FCI	Full configuration Interaction
RS	Rayleigh Schrodinger
NEGF	Non-Equilibrium Greens Function
SCBA	Self-consistent Born Approximation
MI	Mangifera Indica
VOC	Volatile Organic Compound
OR	Olfactory Receptor
PCA	Principal Component Analysis
SiNW	Silicon Nanowire
FET	Field-effect Transistor
VNL	Virtual Nano-lab
EH	Extended Huckel

Chapter 1

1. Introduction

"If you are ambitious to find a new science, measure a smell," – said Alexander Graham Bell in 1914 [1]. What is smell? The smell is some sensation perceived when an odorant molecule interacts with a receptor. However, what physicochemical property of the molecules defines its odor has a non-obvious answer. Scientists have long speculated on two possibilities regarding the essential property of a molecule deciding its odor: geometric shape and vibrational energies. The Vibration Theory of olfaction (VTO), first proposed by Dyson [2], suggests that the olfactory receptors work like chemical spectrometers, sensing the localized vibrations of odorant molecules. The Shape Theory, which has gained wider acceptance, states that the odorants bind to the receptors, after which the receptors undergo a conformational change from inactive to an active state - a so-called *docking* or *lock-and-key* mechanism [3]. VTO was revived by Turin by postulating Inelastic Electron Tunneling Spectroscopy (IETS) as the mechanism for detecting vibrational energies [4]. VTO has positioned Olfaction as a prototypical system within the new field of Quantum Biology [5]. While the Vibration Theory has been debated vigorously [6-8], some experiments [9-11] suggest that molecular vibrations play a part in odor perception. It is not new to look beyond conventional theories; complex activation mechanisms beyond docking occur in biology, e.g., in cancer immunology [12].

The relation between the stimulus and response is well mapped in vision and audition. Also, the visual and audio senses technology has evolved a lot. However, the machines developed regarding chemical senses like olfaction or gustation (taste) still need to be improved. Olfaction is a primary sense as it is important for the fundamental capabilities of a human. It can help us in many ways, from identifying food, realizing a memory, feeling pleasure, and avoiding danger. Biological olfactory systems, humans, insects, and dogs are much more sophisticated than the artificial nose sensors developed so far; for instance a polar bear can smell a seal from a distance of 20 miles away from it and 3 feet beneath the ice from a distance of 1km [12]. An understanding of the existing superior system is important to mimic them. These chemical senses are also important for cyberspace, which mainly depends upon

visual and auditory senses and is incomplete or will lack reality until and unless they include these senses.

The first artificial olfaction machine was first proposed 30 years ago. The research progressed, and a whole lot of sensors emerged. Academic research has advanced, but its application to the industry still needs to be improved. The sensitivity, selectivity, and robustness of such sensors should be much improved for the actual application. *Electronic nose (EN) sensors* try to recognize and classify complex odors. The device offers fast and non-invasive methods for odor recognition. Each chemical has a unique fingerprint that an EN sensor can identify. EN sensors have transducers that act as receptors and convert the chemical signal into an electrical signal [13]. Different types of sensors, such as fiber optics, piezoelectric crystal, metal oxide, and conductive polymers, are used in electronic nose technology. Pattern recognition systems are also used to identify and classify different odors. Here are a few examples of most used EN sensors applied in various practical applications [14]:

Metal-oxide sensors

Metal Oxide Semiconductor (MOS) sensors are the popular electronic nose sensor because of their affinity for all types of gases. The operational principle of MOS sensors is based on the reaction between odorant molecules present in the air and its surface. The interaction changes the gate potential that produces conductance change. These sensors are frequently used because of their high selectivity and sensitivity, and they can operate at high temperatures.

Conducting Polymer Sensor:

When an analyte interacts with the conducting polymer, the change in the resistance of the sensor leads to the detection of the analyte. Conducting polymers sensors are used in many artificial noses in the medical, beverage, food and pharmaceutical industries because of their low cost, fast response to odorants, and resistance to sensor poisoning. There are many processes to manufacture polymer films, like vapor deposition polymerization, thermal evaporation, electrochemical deposition, layer-by-layer (LbL) self-assembly technique, etc.

Several conducting polymers are used in sensors, such as polypyrrole, polyaniline, and polythiophene.

Electrochemical gas sensors

In these electrochemical gas sensors, the oxidation and reduction of the molecules on the electrode's surface led to the current flow. EC sensors are used by security and industrial applications.

Optical Sensors

Optical sensors measure fluorescence, polarization, absorbance, and colorimetric changes, and any of these changes can be used to detect odorants. These sensors are made up of chemically responsive dyes. Fluorescence sensors are more sensitive than colorimetric sensors and identify fluorescent light emitted by the samples.

Infra-red Spectroscopy

Near-infrared spectroscopy (NIRs) can acquire information about the nature of the functional groups present in a molecule by understanding the interaction between the light and the structure of the molecule. Because each material has a unique combination of atoms, and no two compounds produce the same spectra. NIRs techniques have been applied to a wide range of agri-food applications, and the feasibility of NIRs spectroscopy to measure quality attributes of fruits and vegetables has been shown for many products [15].

In EN technology, Machine learning algorithms are used to process large amounts of data collected from the sensor array. Pattern recognition algorithms are used for quantifying and classifying chemicals detected by an EN. Usually, classification algorithms are combined with data analysis techniques to recognize distinct aromas.

The progress of any sensing technology depends upon the research of new sensing material, new transduction techniques, and new pattern recognition techniques. As mentioned above, Inelastic electron tunneling is the transduction mechanism in VTO, and with the ongoing

research in inelastic electron tunneling spectroscopy (IETS), it might be possible in the coming future to realize IETS-based sensors [16]. IET Spectroscopy (IETS) is the simplest way to try to realize a biomimetic nose. It is a non-optical, all-electrical spectroscopic technique [17]. In the basic IETS device, electrons traverse a potential barrier by quantum mechanical tunneling, losing some energy to vibrational modes in the barrier material. This leaves signatures of the vibrational modes on the transport. However, at higher temperatures, the electron energy distribution broadens out, thereby washing out the IET peaks.

To make IETS based electronic nose sensors within the context of VTO, it is important to understand the mechanism and the theory behind it. **Chapter 2** gives a theoretical background before diving into the problem. It introduces the basic concept of olfaction, related theories of transduction in olfaction, and biological background. **Chapter 3** explains the vibrational spectrum of molecules and introduces the Density Functional theory, which can be further used to understand VTO. **Chapter 4** uses the techniques described in chapter 3 and combines physics and machine learning in the simplest way to understand pattern recognition in VTO based sensors.

To move beyond conventional VTO, **Chapter 5** introduces Chirality and theory around enantio-selection in bio-recognition, Chirality Induced Spin Selectivity (CISS). It also explains Symmetry Adapted Perturbation theory (SAPT), which elucidated the path for including spin in charge polarization and making the process enantioselective. This chapter tries to look beyond the shortcomings of VTO. To simulate transport in nanoscale devices, it is important to understand the physics and techniques behind quantum transport. **Chapter 6** gives a brief insight into the Non-Equilibrium Green's Function (NEGF) technique. It also explains transport in Inelastic Tunneling Spectroscopy (IETS) by introducing phonons and electron-phonon coupling. **Chapter 7** combines CISS and IETS to design an enantio-selective E-nose sensor.

One of the real-world uses of an EN sensor is the detection of fruit freshness. **Chapter 8** talks about the approach used to design this sensor. The chapter explains the importance of small organic molecules (whether odorants or Volatile Organic Compounds (VOC)) in the freshness monitoring of fruits and vegetables and a way to design sensors around these molecules. In the end, we summarize the findings and look toward the future.

Chapter 2

2. Olfaction, biology and beyond

This chapter introduces the phenomenon of olfaction, the biology of olfactory system and various theories around its transduction mechanism.

2.1 The Olfactory Space

Perception (any perception) works by mapping the objects in the stimulus set to the perceptual set through some underlying function. This mapping between the stimulus and response is not well-defined in olfaction as it is in vision and audition. It is elusive to understand this mapping because from a psychological point of view, the classification of odors in perceptual space reflects more on the behavioural needs and responses of individuals, than on the physical similarities among the stimuli [18]. Nevertheless, part of the olfactory percept is innate and hard wired into the olfactory system. For example, laboratory rodents will react dreadfully to the cat odor though it has never seen or experienced the presence of cat in its lifetime [19].

Smell is considered as the most intimate sense of all because of its strong connection with memories, emotion, and behaviour. Nose connects us with the outer world as soon as the odorant molecule enters the nasal cavity. The complexity of the response of our Central Nervous System makes it also necessary to understand the anatomy of the biological system. The complexity of the perceptual space and lack of clarity in the stimulus space only adds to the grand problem of olfaction. The perceptual space comprises verbal descriptors like sweet, sour, musky, garlic etc., and stimulus space comprises the small, volatile hydrophobic molecules called odorants. There are different theories regarding the mapping between the stimulus space and the perceptual space in olfaction.

2.1.1 The 'lock and key model'

In 1899 German chemist Emil Fischer proposed the lock and key model for enzymes [20] which later formed the basis of the shape theory of olfaction. R. W. Moncrieff extended these shape-based molecular interactions in olfactory systems [21]. This theory has a wider acceptance under the docking theory and accurately reflects a range of non-covalent interactions along with shape. This theory is mainstream in the fragrance industry and academic molecular biology. Years after this, Amoore speculated that the thousands of smells distinguishable by a human nose are a combination of seven basic primary odors correlating to respective receptors, the same as colors in visible light are generated by the activation of three primary color receptors. The most convincing work was done on the camphoraceous odor, for which he positioned a hemispherical socket in which spherical molecules, such as camphor, cyclooctane, and naphthalene, could bind [22].

There is plenty of evidence that the docking theory stands correct. Ethyl citronellyl oxalate and cyclopentadecanolide are structurally similar and have similar smells [23]. Nevertheless, there are noticeable evidence against the structure-fit theory of olfaction:

1. Same structure, different smell

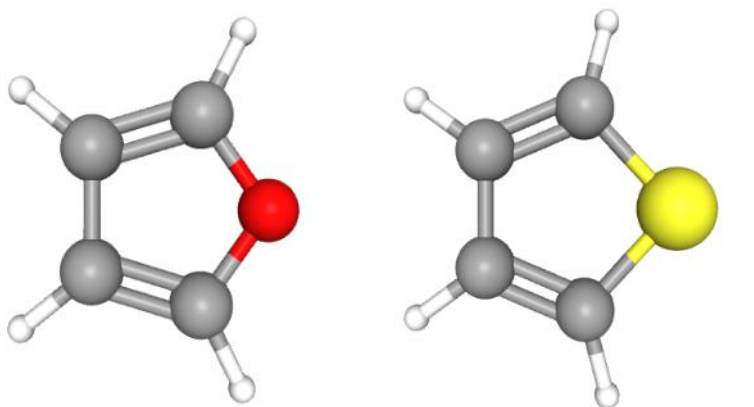


Figure 2.1: Furan (left) and thiofuran (right) are similar in shape but have a different smells. Furan smells like roasted coffee, whereas thiofuran has a hint of benzene. [24]

2. Different structures, similar smell

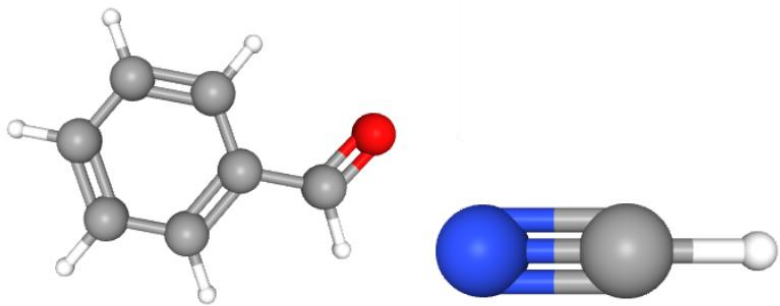


Figure 2.2: Benzaldehyde (left) and hydrogen cyanide (right) are different structurally but smell similar (smell like rotten almond) [24].

There are some intuitive problems with the structure-fit theory, the biological system being prone to thermal fluctuations which can alter the shape of a molecule. This may compromise the conformational orientation at the interaction site. There are ample examples that exhibit the uncertainty of the smell, as shown in Figure 2.3, and the complexity of mapping between shape and odor.

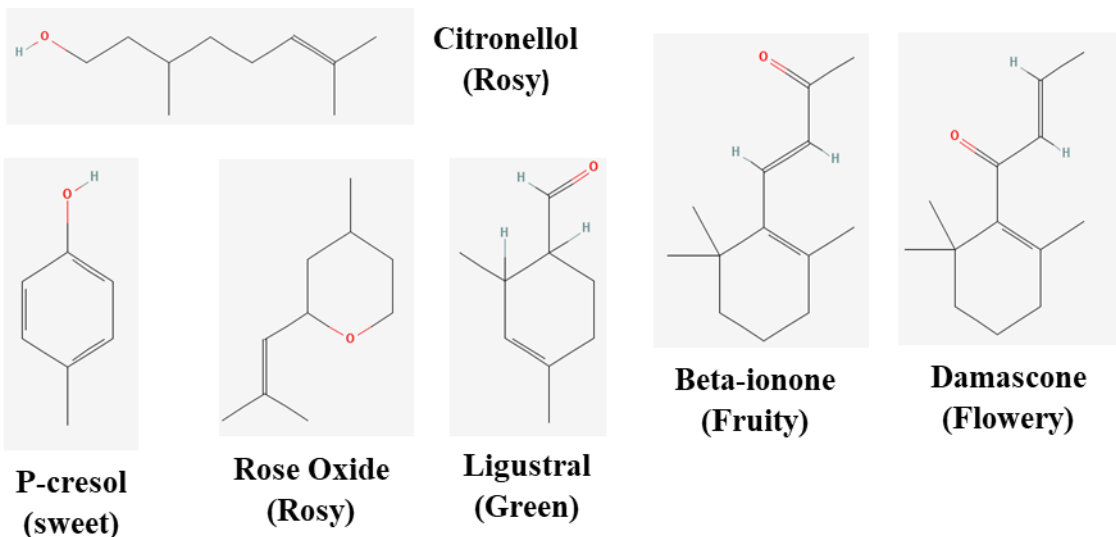


Figure 2.3: The unpredictability of smell, a few examples of molecules with different structure, and smell depicting the complexity of perceptual and physicochemical space of olfaction. [24]

2.1.2 The odotope theory

According to this theory, the molecule's shape plays a key role in its recognition. In the odotope theory, a molecule's shape affects how it is initially received even though the receptor is not required to do so. After initial reception, the receptors respond to some local structural features like functional groups instead of the whole shape of the molecule [25]. The thought gives more importance to the atoms present in the molecule rather than their position in the molecule. But again, this theory has too many combinations and variables. If the receptors are not particular, it may lead to many signals and unnecessary noise in the system [26].

2.1.3 The vibration theory

It was Malcolm Dyson who first proposed the concept of osmic frequencies [2]. Robert H. Wright in 1954 revived the vibrational theory by suggesting a mechanical way of signal transduction [27]. The Vibrational Theory of Olfaction states that the signature of the scent of a molecule is identified by its unique vibrational spectrum and not its structure or shape. The unique smell is mapped to the unique vibrational spectrum of the molecule as the color of light is mapped to the frequency of light. The simple intuition behind this phenomenon is projecting olfaction as a spectral sense, similar to vision and audition.

The main detriment to the VTO was the need for more clarity on a biological mechanism that could behave spectroscopically. In a laboratory setup, the vibrational spectrum of a molecule is measured by probing the molecular vibration with an infrared (IR) source of the correct frequency. The scientific community found it difficult to imagine a biological system capable of probing molecular frequencies spectroscopically. A biological olfactory system cannot irradiate a molecule with infrared light to probe the vibrational frequencies. How to probe the vibrational spectrum in a biological environment? Optical spectroscopy is impossible. Wright thought of thermal vibrations and detecting vibrations mechanically [27]. A thermal energy-based mechanical system can detect vibrations only below 500 cm^{-1} , which contradicts the basic nature of the olfactory objects. Inorganic molecules like hydrogen cyanide have a strong bitter almond smell and vibrate way above 500 cm^{-1} . So, this mechanism cannot be facilitated by our olfactory systems.

2.2 Biological background

To understand the feasibility of VTO, it is important to understand the basic anatomy of the olfactory system as found in nature. Figure 2.4 shows the journey of odorant in the human olfactory system. The first step in the journey of the odorant is to meet the olfactory mucus, which covers the olfactory epithelium. The thickness of olfactory epithelium is about 10-40 μm [28]. The main function of the mucus is to act as the separating column between the outer world and epithelium as it moderates the amount of odorant reaching the epithelium [26]. The mucus also contains small carrier proteins called odorant binding proteins (OBPs). The OBPs mainly transport the hydrophobic odorants across the wet mucus layer [29]. The Olfactory Sensory Neurons (OSNs) traverse the epithelium and extent to the mucus terminating in cilia that protrudes from the dendritic knob [30]. The number of cilia is between 10-50 for each neuron and is about 0.3 μm in diameter. The type and number of ORs on the cilia vary depending on the species. The OSN is a bipolar cell whose depolarization is responsible for generating the electrical signal.

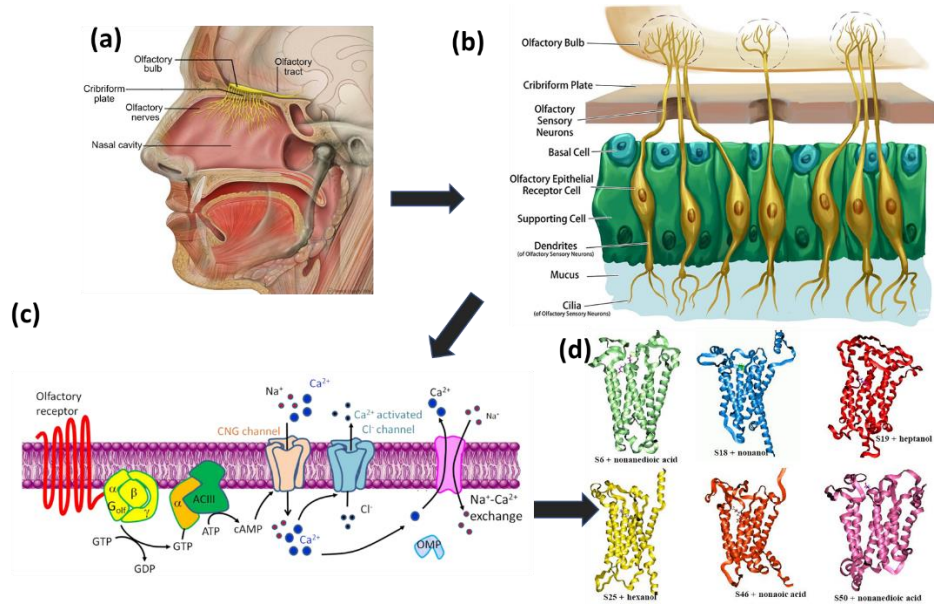


Figure 2.4: The biological olfactory system showing the odorant's journey from (a) the nasal cavity [33] to (b) the olfactory epithelium [34] to (c) the olfactory sensory neuron [35] and finally to (d) the receptor [36].

OSNs, like other parts of the Central Nervous System, have re-generational abilities, with regeneration occurring at a timescale of 30-45 days [26]. The axons of the olfactory receptors extend directly into the highly organized olfactory bulb, where the odor information is further processed. A polymerase chain reaction found that one receptor is encoded per olfactory cell. [31,32]

2.2.1 Olfactory Epithelium

The olfactory epithelium is 30-200 μm thick and has an area of 2-20 cm^2 ; the area and thickness depending upon the species [37]. Figure 2.4 (b) shows that the epithelium is structurally adapted to work as a sensory system; it has three types of cells: the olfactory sensory neurons, basal cells, and sustentacular cells. There are 50-100 million OSNs with an estimated 45000 OR's corresponding to a surface density of 100 receptors per μm^2 (in humans). In OSN, the cilia contain the olfactory receptor, which is bound to G-proteins (G_{olf}); hence the name G-protein coupled receptors. When the odorant binds to the receptor, it releases a G_{alpha} subunit, activating adenyl cyclase III formation. Adenyl cyclase is an enzyme that activates the formation of second messenger cyclic adenosine monophosphate (cAMP) [38]. The cAMP binds cationic channels, and cyclic nucleotide-gated (CNG) signal is released, resulting in the opening of the Ca^{2+} and Na^{2+} channels. The opening of the channel depolarizes the cell. In a secondary transduction mechanism, G-proteins couple to phospholopase C (PLC). PLC triggers the production of inositol trisphosphate (IP3), which activates the IP3- gated Ca^{2+} channel, and the cell membrane depolarizes. The change in receptor potential fires an action potential to the brain [26].

2.2.2 Olfactory Receptors

Olfactory receptors are receptors responsible for the chemoreception of molecules in the olfactory system. They are called membrane proteins because they are expressed in the cell membranes of olfactory sensory neurons. The olfactory signal initiates when the odorant molecule comes and interacts with the olfactory receptor. The activation of olfactory receptors triggers the neural impulse, which transmits information about odor from the nose to the brain [31]. The information about the 3-dimensional structure of these receptors is very limited. Only 85 high-resolution membrane protein structures have been determined to date, although

the Protein Data Bank (PDB) contains nearly 250,000 protein structures. None of the 85 membrane proteins are olfactory receptors, but they can assume to be ORs since they are the largest multigene family in multicellular organisms [32]. Determining the structure is difficult because GPCRs are difficult to crystallize. However, the discovery of the genomic sequence of ORs allows the evaluation of its structure through homology modeling techniques, where the amino acid sequence can be compared against the sequence of related and already known proteins [39]. Bovine rhodospine is the obvious candidate since it is a GPCR and its structure is known accurately [40].

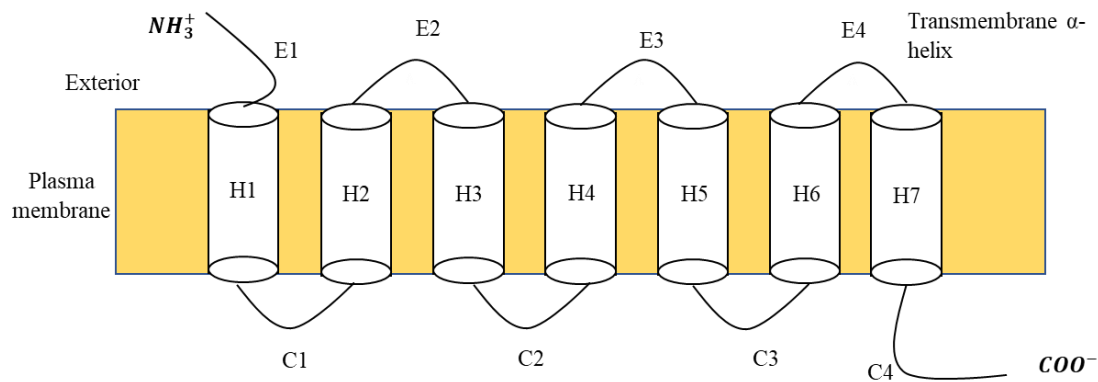


Figure 2.5: Structure showing the seven trans-membranes alpha helices with an exterior and interior region. E and C are extracellular and intracellular loops.

A GPCR has seven trans-membrane helices that cross a hydrophobic region stabilized by a lipid layer [41], as shown in Figure 2.5. These helices are linked by loops that end in a carboxyl group inside the cell and a nitryl group outside the cell. The hydrophobic lipid layer contains the main body of the receptor protein. The ligand (odorant) binding site can be presumed to be within the hydrophobic layer. It has been shown that odorants induce a GTP-dependent increase in adenylyl cyclase activity in the cilia, suggesting intracellular G-proteins' involvement. G-proteins were highly expressed in the olfactory sensory neurons. At room temperature, the receptors are dynamic and take some conformations. The binding of the ligand can either stabilize the receptor or partially stabilize the receptor or stabilizes an inactive conformation of the receptor.

The olfactory receptors are present in the olfactory epithelium, and their signal goes to multiple regions in the olfactory bulb. As shown in Figure 2.6, an olfactory bulb, in turn,

illuminates different parts of the olfactory cortex, a portion of the cortical region on the ventral surface of the forebrain concerned with generating the sense of smell.

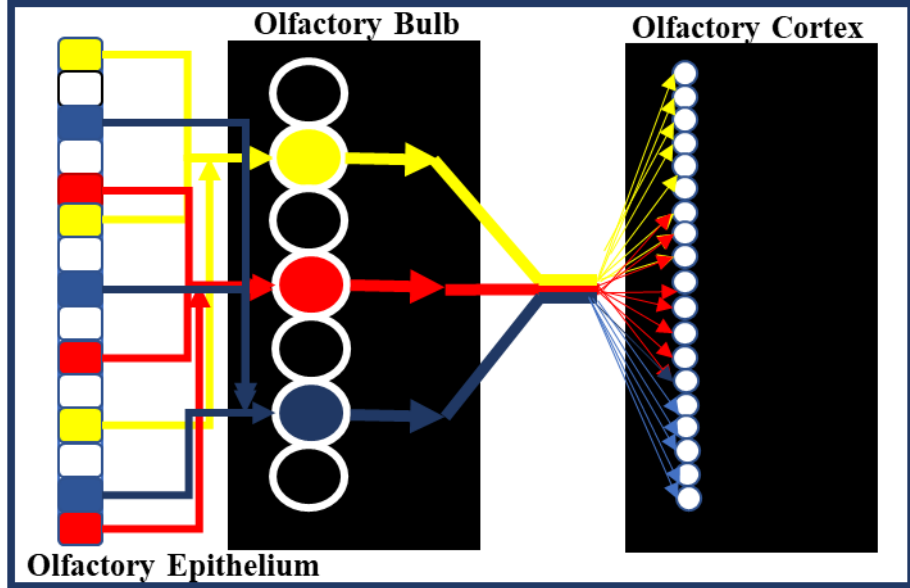


Figure 2.6: The organization of inputs from odorant receptor, present in the olfactory epithelium (OE), to the olfactory bulb (OB), olfactory cortex (OC). Inputs from different ORs are separated in different neurons and glomeruli in the OE and OB. [30]

The interaction between protein and ligand is an induced fit, where the presence of the ligand induces a conformational change in the protein and makes it active. The fitting of ligand and protein unites them in a preferred geometry due to the presence of each other. This conformational change is small, but it makes the receptor active. There is a different idea of conformational selection in which the presence of the ligand selects a higher energy state, and equilibrium shifts towards that conformation. Before this meeting, the protein can exist in many states in dynamic equilibrium. As discussed in the literature, the second idea works well in cases where the interaction of ligand and receptor can directly deionize the cell. However, in GPCRs, an interim step of G_{olf} activation complicates the matter. [26]

Olfactory receptors are used combinatorially to encode odor identities, shown in Figure 2.7, and since different odorants can be identified, different combinations of ORs should be used. The combinatorial coding can provide discrimination of an almost infinite number of odorants. Changing the structure of the molecule can alter its perceived odor. Even the

concentration of an odorant can change its receptor code and perception. It has been found that receptors respond to more than one odorant [30]. So as receptors discriminate many odorants, it cannot be simply correlated to the shape.

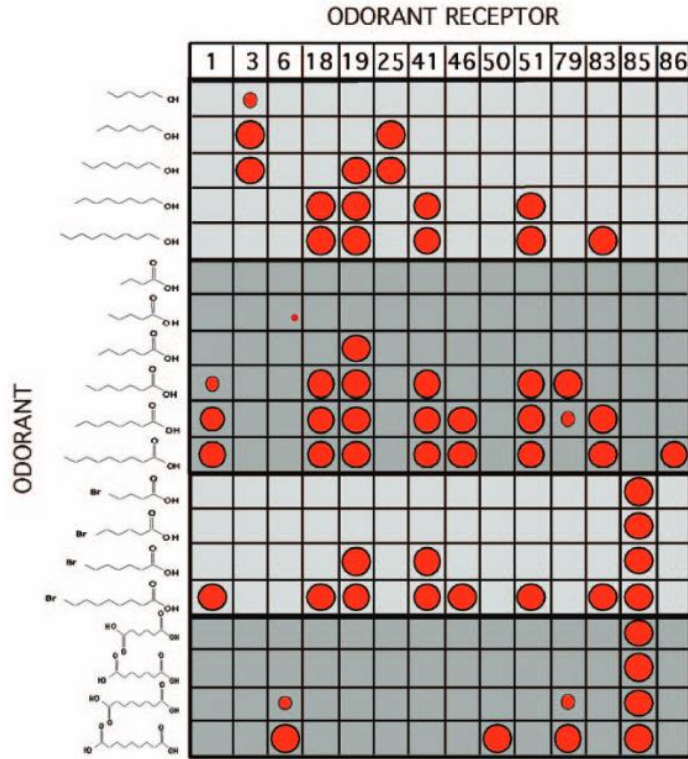


Figure 2.7: Combinatorial code generated by receptors for different odorants. [30]

Identifying binding sites in the olfactory receptor is still an open problem, explored from all angles. Odorants are typically small, light, hydrophobic and stable molecules. At the binding site, also called the binding pocket, it is assumed that the ligand interacts with the receptor protein via physical forces like hydrophobic forces and van der Waal forces. However, the exact method of interaction has yet to be determined. These physical forces can stabilize the ligand in the pocket by restricting its translation or rotation. The presence of transition metals also stabilizes the ligand. In a present structure-activity relationship, it is assumed that the binding of ligand and receptor activation are independent of each other. In the list of all unanswered questions about olfaction, affinity versus efficacy is important. The difference in activity of a receptor towards a ligand is due to affinity or efficacy? The different OR structures affect the binding of ligand and protein or does it affect the actuation of the signal? The change in concentration also alters the perception of the odor. The odorant must eventually leave the binding site in olfaction as the process is completely physical. What

explains the difference in affinity of GPCRs towards ligands in the binding and release state? [26]

2.3 Turin's Model

In an article published in Chem. Senses in 1999, named 'A spectroscopic mechanism for primary olfactory reception,' Luca Turin proposed his theory of the nose as a working spectroscope [4]. He proposes a mechanism of signal transduction based on inelastic electron tunneling. His theory postulates that an electron tunnels from an acceptor state to a donor state facilitated by the odorant molecule. As illustrated in Figure 2.8, the energy difference between the donor and acceptor energy state is equal to the localised vibrational mode of the odorant. The receptor will have to act as a source and sink of electrons. In a laboratory setup of inelastic electron tunnelling spectroscopy, current flows through an insulating material from one electrode to another through tunnelling.

To convert this laboratory setup of IETS into a biological system, the system will need an source and sink of electron, appropriate levels of energy and a donor and an acceptor. Turin suggests that nicotinamide adenine dinucleotide phosphates (NADPH) act as the source of electrons. It binds to the receptor via amino acids present in the system. Turin asserts the importance of zinc at the acceptor site, inferred from the fact that deficiency of zinc can cause anosmia. Turin proposed that zinc docks the G_{olf} which forms a disulphide bridge between receptor and G-protein [4]. The disulphide bridge gets oxidized due to the transfer of electrons and releases the G-protein. But how does the G-protein know when to get released?

Turin suggests that about ten broadly tuned receptors produce signals that overlap with each other. It has been found that the resting potential of olfactory cells is about 50-65 mV and the capacitance of 4 pF. Turin estimates that at the receptor site, the required emf for NAPDH is also around 50-65 mV, which corresponds to the energy of the vibrational frequencies of molecules up to 4000cm^{-1} . Turin proposed that the receptors can be tuned to a band of frequencies. Also, the donor and acceptor energy levels can be susceptible to the thermal broadening of the range $2kT$ (400 cm^{-1}). There are ten kinds of receptors which can sweep the whole spectrum $0-4000\text{ cm}^{-1}$, if they overlap to produce signals as it happens in the three receptors in vision [26]. The electron transfer can take place if there are donor and acceptor

empty energy levels. Sequence homology tells us that amino acid residues can act as the donor and acceptor states. The most likely explanation can be that the availability of amino acids can tune the donor-acceptor states similar to frequency modulation of receptor in visual processes. [42]

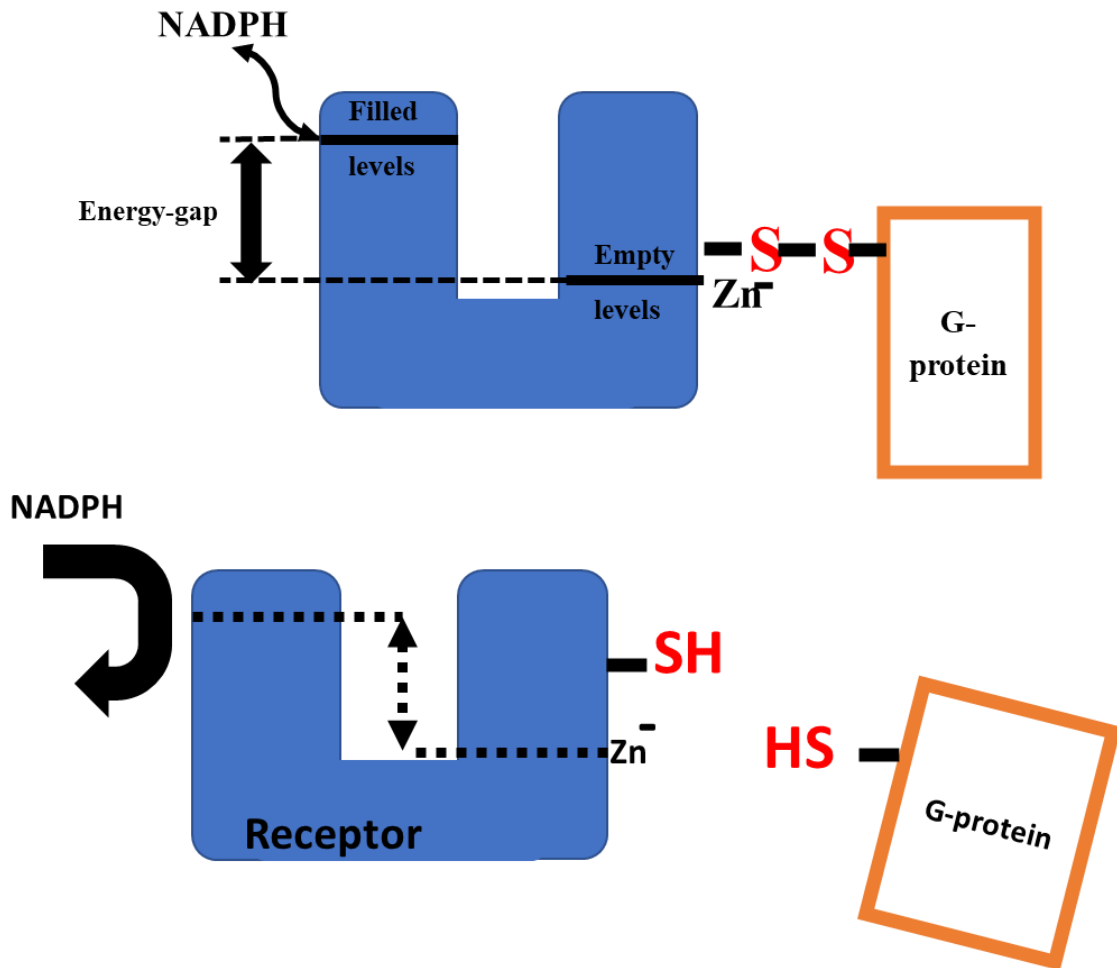


Figure 2.8: The receptor takes electrons from NAPDH. When odorant interacts with the receptor the disulphide bond breaks after oxidation and G-protein gets released [26].

Chapter 3

3. The physical picture of molecules and Density Functional Theory

To understand the VTO, it is important to know what a molecule's vibration and vibrational spectrum mean. This chapter explains the theory of the vibrational spectrum of molecules, chemical graph theory, and DFT, which can act as tools to understand the following work in the thesis.

3.1 Vibration

What is a molecule?

A molecule is a collection of interacting nuclei and electrons given by the Hamiltonian:

$$H = -\frac{1}{2} \sum_i^N \nabla_i^2 - \frac{1}{2} \sum_A^M \frac{\nabla_A^2}{M_A} - \sum_i^N \sum_A^M \frac{Z_A}{r_{iA}} + \sum_i^N \sum_{i \neq j}^N \frac{1}{r_{ij}} + \sum_A^M \sum_{A \neq B}^M \frac{Z_A Z_B}{R_{AB}}$$

Eq. 3.1

where i,j are the N electrons, A,B are the M nuclei and M_A is the ratio of mass of nucleus and mass of electron [43]. Z_A is the atomic number of the nucleus A , Laplacian operators over i and A indicate differentiation with respect to the position of i^{th} electron and A^{th} nucleus. R_{AB} is the distance between A^{th} and B^{th} nucleus, r_{ij} is the distance between i^{th} and j^{th} electron and r_{iA} is the distance between i^{th} electron and A^{th} nucleus. The first term is the kinetic energy of electrons, second term is the kinetic energy of nuclei, third term is the attraction energy between electron and nucleus and fourth and fifth terms are the coulomb repulsions between

two electrons and two nuclei. This description of Hamiltonian will be used in solving the time-independent Schrodinger equation

$$H|\Psi\rangle = E|\Psi\rangle$$

Eq. 3.2

3.1.1 The Born-Oppenheimer Approximation

The Born-Oppenheimer approximation reduces complexity by separating nuclear and electronic motion [44]. Mathematically,

$$\Psi(r; R) = \Psi_{elec}(r; R)\Psi_{nuc}(R)$$

Eq. 3.3

where r , R denotes electronic and nuclear coordinates respectively. The electronic wavefunction depends on nuclear coordinates parametrically and nuclear wavefunction depends directly on the nuclear coordinates. The approximation seems reasonable because the nuclei are significantly heavier than the electrons, so the electrons are much faster, and the nuclei appear stationary. In the electron frame of reference, the nucleus is stationary so the kinetic energy can be neglected and the interaction between the nuclei can be treated as a constant.

$$H_{elec} = -\frac{1}{2} \sum_i^N \nabla_i^2 - \sum_i^N \sum_A^M \frac{Z_A}{r_{iA}} + \sum_i^N \sum_{i \neq j}^N \frac{1}{r_{ij}}$$

Eq. 3.4

The Schrodinger equation becomes,

$$H_{elec}|\Psi_{elec}(r; R)\rangle = E_{elec}|\Psi_{elec}(r; R)\rangle$$

Eq. 3.5

The equation 3.5 implies that electron adiabatically follows the nuclei, they rapidly adjust to the new nuclear coordinates. These wavefunctions are orthonormal and depend on r for a particular value of R . The electronic solution can be substituted into the equation for nuclear motion. The motion of electron can be represented as an average with respect to the nuclei, the Schrodinger equation becomes

$$H_{nuc} = -\frac{1}{2} \sum_A^M \frac{\nabla_A^2}{M_A} + \left\langle -\sum_i^N \sum_A^M \frac{Z_A}{r_{iA}} - \frac{1}{2} \sum_i^N \nabla_i^2 + \sum_i^N \sum_{i \neq j}^N \frac{1}{r_{ij}} \right\rangle + \sum_A^M \sum_{A \neq B}^M \frac{Z_A Z_B}{R_{AB}}$$

Eq. 3.6

This reduces to a motion of the nucleus in a time-averaged field of electrons

$$H_{nuc} = T_N + E_{total}(R)$$

Eq. 3.7

The potential energy experienced by the nucleus can be expressed as,

$$E_{total}(R) = E_{elec}(R) + \sum_A^M \sum_{A \neq B}^M \frac{Z_A Z_B}{R_{AB}}$$

Eq. 3.8

$$[T_N + E_{total}(R)]|\Psi_{nuc}(R)\rangle = E_{nuc}(R)|\Psi_{nuc}(R)\rangle$$

Eq. 3.9

The solution of the above equation can be used to describe the vibrational, rotational and translational motion of the molecule, which is quite different from the electronic transitions. The plot of E_{total} with respect to R gives the potential energy surface (PES) or adiabatic surface. Electronic energy has a kinetic energy component but as it is averaged over so it behaves as a potential energy hence the name PES.

3.1.2 Harmonic Oscillator

The classical Oscillator is a very common and very relevant problem in physics. The nuclei is massive as compared to other quantum mechanical objects; the motion of nuclei can be described harmonically and classically. The classical Harmonic Oscillator has a system where a restoring force acts on a particle of some mass bound to the origin, given by Hooke's Law, $F = -kx$. The potential energy, Figure 3.1, corresponding to this force will be $V = \frac{1}{2}kx^2$, where k is the spring constant and x is the displacement from the equilibrium. The energy vs. displacement plot is parabolic, whose negative differentiation at any point with respect to x gives the force, $F = -\frac{dV}{dx}$. The potential energy is minimum at $x=0$ and hence the energy is purely kinetic at this point. Far away from the $x=0$ point, the energy is purely potential, and the particle is stationary at this extremum point. The vibration is between these two extremum points [40]. The energy at any point can be written as the sum of potential and kinetic energy.

$$E = \frac{1}{2}m\dot{x}^2 + \frac{1}{2}kx^2$$

Eq. 3.10

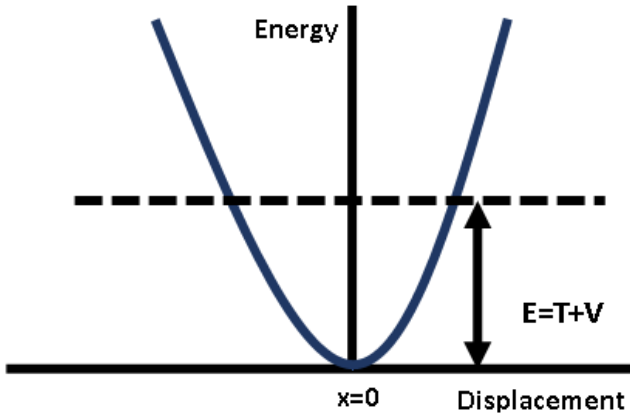


Figure 3.1: Energy diagram of a classical Simple Harmonic Oscillator.

3.1.3 Quantum Oscillator

Quantum mechanically, the total energy can be represented as the sum of kinetic and potential energy. The Schrodinger Equation becomes

$$-\frac{1}{2\mu} \frac{d^2\Psi(x)}{dx^2} + V(x)\Psi(x) = E(x)\Psi(x)$$

Eq. 3.11

The potential energy operator is $V(x) = \frac{1}{2}\mu\omega^2x^2$ where $\omega = \sqrt{\frac{k}{\mu}}$ and μ is the reduced mass.

The Taylor expansion of the potential energy around displacement $x = a$.

$$V(x) = V(a) + V'(a)(x - a) + \frac{1}{2}V''(a)(x - a)^2 + \dots$$

Eq. 3.12

At equilibrium for $x=0$, $V'(a) = 0$ so $V(x) = \frac{1}{2}V''(0)(x)^2 = \frac{1}{2}kx^2$, which implies that the spring constant is nothing but the second derivative of the potential energy $k = V''(x = 0)$.

$$\frac{d^2\Psi(x)}{d\xi^2} + \left[\frac{2E}{\hbar\omega} - \xi^2 \right] \Psi(x) = 0$$

Eq. 3.13

$$\xi = \sqrt{\frac{\mu\omega}{\hbar}} x$$

The energy eigen values or the above equation come out to be $E_n = \hbar\omega \left(n + \frac{1}{2} \right)$; this gives discrete allowed energy levels, and n is the quantum number. As shown in Figure 3.2, the zero-point energy is the energy corresponding to $n = 0$, $E_0 = \frac{\hbar\omega}{2}$. The energy levels in the spectrum are equidistant from each other and separated by $\hbar\omega$ [40].

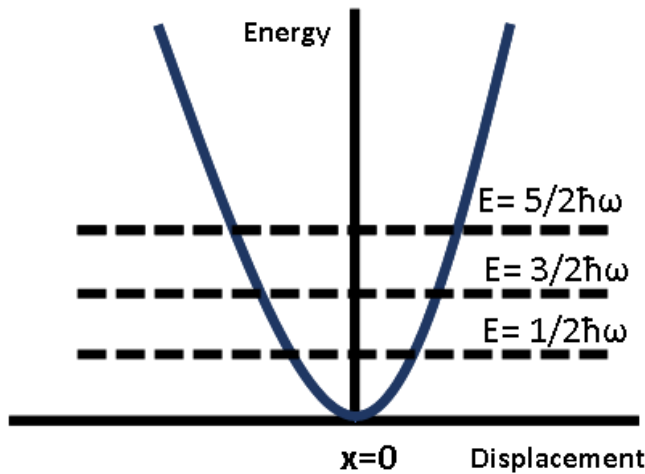


Figure 3.2: Energy diagram of a quantum Harmonic Oscillator.

The displacement at any instant cannot be greater than the maximum displacement allowed, called the amplitude. In quantum mechanics particle moves into the classically forbidden

region, but the more the penetration, the less likely the particle will be found, so $\Psi(x) \rightarrow 0$ as $|x| \rightarrow \infty$. The solution requirements of the Quantum Harmonic Oscillator are met by Hermite functions [44]; they are exponential functions with polynomial terms in them. The general formula for the eigenfunction is

$$\Psi_n(x) = \left[\frac{1}{2^n n!} \left(\frac{\hbar}{\mu\omega} \right)^n \right]^{\frac{1}{2}} \left(\frac{\mu\omega}{\pi\hbar} \right)^{\frac{1}{4}} \left[\frac{\mu\omega}{\hbar} x - \frac{d}{dx} \right]^n e^{-\frac{\mu\omega}{2\hbar}x^2}$$

Eq. 3.14

If the atoms are displaced from their equilibrium position, they oscillate, and this can be described by a harmonic oscillator using parabolic potential around the minimum if the displacement is small. In fact, any potential around a stable equilibrium can be approximated to have a harmonic behavior. The more accurate representation of atomic potential is given by Lennard-Jones potential. However, the parabolic approximation is sufficient to describe atomic potential energy if deformations from the equilibrium are small.

3.2 Vibrations in small molecules

The nuclei and electrons in a molecule vibrate at their positions; the nuclei are heavier in their mass and tend to restore their equilibrium position when displaced. The arrangement of atoms connected through bonds in a molecule can be approximated as a system of balls connected through springs. It is easier to write and solve the equations for smaller molecules, but as the molecules become bigger, the equations become complicated, and the help of some computer package will be required.

3.2.1 Linear Homo-diatomlic

The simplest case of vibration can be found in a small molecule containing two atoms connected through a single, linear bond, shown in Figure 3.3. Only one degree of freedom is considered, and for simplicity, assume that the masses of atom in this diatomic molecule are

identical. The natural vibration of the molecule can be calculated by finding the equation of motion and approximating the solutions [26].

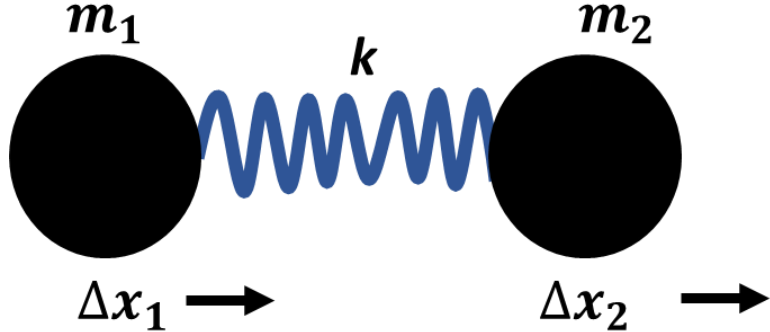


Figure 3.3: A 1-dimensional linear harmonic oscillator

For a diatomic molecule, the kinetic energy and potential energy will be

$$T = \frac{1}{2}m_1(\Delta\dot{x}_1)^2 + \frac{1}{2}m_2(\Delta\dot{x}_2)^2$$

Eq. 3.15

$$V = \frac{1}{2}k(\Delta x_2 - \Delta x_1)^2$$

Eq. 3.16

where $\Delta x_2, \Delta x_1$ is the displacement of atom 2 and 1 and $\Delta x_2 - \Delta x_1$ is the extension of the spring with force constant k. The Lagrange equation will be $L = T - V$, which can be substituted in the Euler-Lagrange equation to obtain the equation of the motion.

$$\frac{d}{dt} \frac{\partial T}{\partial \dot{u}_i} + \frac{\partial V}{\partial u_i} = 0$$

Eq. 3.17

The equations of motion become,

$$m_1 \Delta \ddot{x}_1 + k \Delta x_1 - k \Delta x_2 = 0$$

Eq. 3.18(a)

$$m_2 \Delta \ddot{x}_2 + k \Delta x_2 - k \Delta x_1 = 0$$

Eq. 3.18(b)

Using Fourier transformation, the solution $\Delta x_{1,2} = A_{1,2} e^{i\omega t}$ where A_1 is the amplitude and ω is the frequency of oscillation. Substituting

$$-\omega^2 A_1 m_1 + A_1 k - A_2 k = 0$$

Eq. 3.19(a)

$$-\omega^2 A_2 m_2 + A_2 k - A_1 k = 0$$

Eq. 3.19(b)

The system of the equation reduces to

$$\begin{vmatrix} -\omega^2 m_1 + k & -k \\ -k & -\omega^2 m_2 + k \end{vmatrix} = 0$$

Eq. 3.20

The solution of this determinant gives $\omega^2 = \frac{m_1 + m_2}{m_1 m_2} k = \frac{k}{\mu}$ where μ is the reduced mass. In homo-diatomc molecule $m_1 = m_2 = m$, so $\omega = \sqrt{\frac{2k}{m}}$. Substituting the value of ω in the

above equations $A_1 = -A_2$, it implies that the displacements are equal in magnitude but opposite in direction. These displacements are called normal mode displacement [26].



Figure 3.4: Normal Mode Displacement

3.2.2 Poly-atomics

In a perfect lattice, each atom at the v^{th} site will vibrate at its equilibrium position such that $R_v = R_{0v} + u_v$, where R_v is the position vector of v^{th} atom in the lattice l , R_{0v} is the equilibrium position and u_v is the displacement. The kinetic energy and potential energy will be

$$T = \frac{1}{2} \sum_{v=1}^N m_v [(\Delta \dot{x}_v)^2 + (\Delta \dot{y}_v)^2 + (\Delta \dot{z}_v)^2]$$

Eq. 3.21

$$V = \frac{1}{2} \sum_{l'v'l'v'} u_{lv} K_{l'v'l'v'} u_{l'v'} + O(u^3)$$

Eq. 3.22

If this equation is compared with Taylor expansion of the potential energy, the only term quadratic in displacement is considered, and the linear term is zero because force is zero at equilibrium and higher order terms are ignored within the limit of harmonic approximation [26]. The force constant matrix is defined as:

$$K_{l\nu l'\nu'} = \left(\frac{\partial^2 V}{\partial u_{l\nu} \partial u_{l'\nu'}} \right)_0$$

Eq. 3.23

This matrix is called the Hessian matrix, which can be calculated by using molecular mechanics or molecular orbital calculations. The Hessian matrix is obtained by calculating the potential energy as a function of the position of the atoms and then double differentiating that potential energy with respect to the position. Calculation of the Hessian matrix is important in some energy minimization techniques, also important for frequency analysis which must be done at a relaxed geometry.

After obtaining Lagrange and substituting it in the Euler-Lagrange equation, the equation of motion can be written as:

$$m_\nu \ddot{u}_{l\nu} = - \sum_{l'\nu'} K_{l\nu l'\nu'} u_{l'\nu'}$$

Eq. 3.24

The solution to this equation will give the displacement; it can be assumed to be time-dependent and related to the normal mode via a unitary transformation.

$$u_{l\nu} = \sum_{\alpha} m_\nu^{-\frac{1}{2}} e_{\nu}^{\alpha}(k) \exp(i(k \cdot l - \omega_{\alpha} t)) Q^{\alpha}(k)$$

Eq. 3.25

k is the 3-dimensional wave-vector α is the label on the phonon branch. If there are N atoms, there will be $3N$ vectors and thus $3N$ modes, $e_{\nu}^{\alpha}(k)$ is the normalization constant. The transformation matrix is

$$\chi_{lv}^{\alpha}(k) = m_v^{-\frac{1}{2}} e_v^{\alpha}(k) \exp(i(k.l - \omega_{\alpha}t))$$

$$u_{lv} = \sum_{\alpha} \chi_{lv}^{\alpha}(k) Q^{\alpha}(k)$$

Eq. 3.26

The normal modes are

$$Q(k) = \sum_{lv} \chi_{lv}^{\alpha*}(k) m_v u_{lv}$$

Eq. 3.27

Substituting the value of displacement in the equation of motion, we get

$$-m_v^{1/2} \omega_{\alpha}^2 e_v^{\alpha}(k) + \sum_{l'v'} m_v^{-\frac{1}{2}} K_{vv'}^{l-l'} e_v^{\alpha}(k) \exp(-ik(l-l')) = 0$$

Eq. 3.28

If the sum is taken over all the lattice vectors, $L = l - l'$

$$K_{vv'} = \sum_L K_{vv'}^L \exp(-in.L)$$

Eq. 3.29

$$\sum_{v'} D_{vv'}(k) e_{v'}^{\alpha}(k) = \omega_{\alpha}^2 e_v^{\alpha}(k)$$

$$D_{vv'}(k) = (m_{lv}m_{l'v'})^{-1/2} \sum_L K_{vv'}^L \exp(-ik \cdot L)$$

Eq. 3.30

Dropping the subscripts in matrix notation

$$De = \omega^2 e$$

Eq. 3.31

$$|D - \omega^2 I| = 0$$

Eq. 3.32

D is the Dynamical Matrix whose eigenvalues give square of the 3N *normal mode frequencies*. The eigenvectors give normal mode coordinates [45].

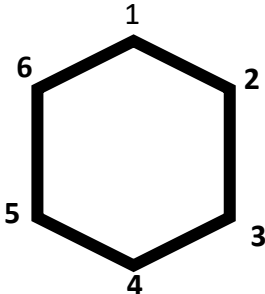
3.3 Vibrational modes of a molecule and Chemical Graph Theory

Chemical graph theory is the branch of chemistry wherein chemical objects like molecules, crystals, polymers, clusters etc., are represented as mathematical objects called graphs. A graph is a collection of nodes and edges connecting them. For a chemical graph, the nodes correspond to atoms, and the edges correspond to the bonds between them. *Molecular descriptors* are obtained as logical and/or mathematical operations on molecular graphs, transforming their chemical information into mathematical form [46]. They are expected to correlate with physical observables measured by standard experiments.

3.3.1 Molecular Graph

For molecular graph $G = (N, E)$, having $n=[N]$ nodes and $m=[E]$ edges, the nodes $v_i \in N$ represent non-hydrogen atoms, and the edges $(v_i, v_j) \in E$ represent covalent bonds between

the corresponding atoms [46]. In particular, hydrocarbons are formed only by carbon and hydrogen atoms and their molecular graphs represent the carbon skeleton of the molecule. The molecular graph for benzene is illustrated below as an example.



3.3.2 Adjacency Matrix

Derived from a molecular graph, the Adjacency Matrix A represents the set of connections between the adjacent pair of atoms. The entry a_{ij} is non-zero if nodes (atoms) v_i and v_j are adjacent to each other and zero otherwise [46].

Going by this, the Adjacency Matrix A for the benzene molecule above is seen to be:

$$A = \begin{matrix} 0 & 1 & 0 & 0 & 0 & 1 \\ 1 & 0 & 1 & 0 & 0 & 0 \\ 0 & 1 & 0 & 1 & 0 & 0 \\ 0 & 0 & 1 & 0 & 1 & 0 \\ 0 & 0 & 0 & 1 & 0 & 1 \\ 1 & 0 & 0 & 0 & 1 & 0 \end{matrix}$$

The Adjacency Matrix for a molecular graph is commonly weighted by atomic properties, such as atomic mass, or electronegativity.

3.3.3 Degree Matrix

The Degree Matrix represents the degree of a node in the molecular graph, calculated by taking the sum of all elements in a single row in the Adjacency Matrix [46].

$$V = \begin{matrix} 2 & 0 & 0 & 0 & 0 & 0 \\ 0 & 2 & 0 & 0 & 0 & 0 \\ 0 & 0 & 2 & 0 & 0 & 0 \\ 0 & 0 & 0 & 2 & 0 & 0 \\ 0 & 0 & 0 & 0 & 2 & 0 \\ 0 & 0 & 0 & 0 & 0 & 2 \end{matrix}$$

3.3.4. Laplacian Matrix

The Laplacian Matrix of a graph is defined as $L = V - A$, where V is the Degree Matrix and A is the Adjacency Matrix of the graph [46]. For the graph above, the Laplacian Matrix is thus:

$$L = \begin{matrix} 2 & -1 & 0 & 0 & 0 & -1 \\ -1 & 2 & -1 & 0 & 0 & 0 \\ 0 & -1 & 2 & -1 & 0 & 0 \\ 0 & 0 & -1 & 2 & -1 & 0 \\ 0 & 0 & 0 & -1 & 2 & -1 \\ -1 & 0 & 0 & 0 & -1 & 2 \end{matrix}$$

3.3.5 Dynamical Matrix and Molecular Vibrational Spectrum

To derive the vibrational modes of the molecule, the molecule can be treated as a network of harmonic oscillators, Figure 3.5 [46].

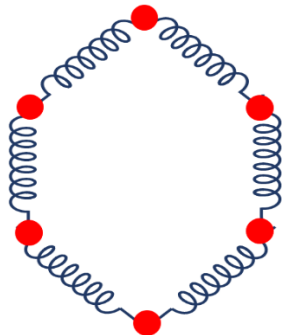


Figure 3.5: Molecule as a network of harmonic Oscillator

Newton's equation of motion for each atom (node) may be written as:

$$m_i \frac{d^2 u_i}{dt^2} = - \sum_{i \neq j} K_{ij} (u_i - u_j)$$

Eq. 3.33

where K is the spring constant of the Oscillator, m is the mass of the atoms and u_i is the displacement of the i^{th} atom. In this section the K are assumed simplistically, for illustrative purposes, to be the same for each Oscillator. The next section will elucidate how the K is evaluated in terms of interatomic forces for a realistic calculation of the vibrational modes of an actual molecule.

This can be written in the following matrix form:

$$\begin{bmatrix} \frac{K}{m} & -\frac{2K}{m} & 0 & 0 & 0 & -\frac{K}{m} \\ -\frac{K}{m} & \frac{2K}{m} & -\frac{K}{m} & 0 & 0 & 0 \\ 0 & -\frac{K}{m} & \frac{2K}{m} & -\frac{K}{m} & 0 & 0 \\ 0 & 0 & -\frac{K}{m} & \frac{2K}{m} & -\frac{K}{m} & 0 \\ 0 & 0 & 0 & -\frac{K}{m} & \frac{2K}{m} & -\frac{K}{m} \\ -\frac{K}{m} & 0 & 0 & 0 & -\frac{K}{m} & \frac{2K}{m} \end{bmatrix} \begin{bmatrix} u_1 \\ u_2 \\ u_3 \\ u_4 \\ u_5 \\ u_6 \end{bmatrix} = \omega_v^2 \begin{bmatrix} u_1 \\ u_2 \\ u_3 \\ u_4 \\ u_5 \\ u_6 \end{bmatrix}$$

which can be compactly expressed as:

$$\sum_j D_{ij} u^v_j = \omega_v^2 u^v_i$$

Eq. 3.34

Here D is called the Dynamical Matrix and ω_v^2 is the v^{th} eigenvalue (necessarily real) which is the square of the vibrational eigenfrequency of the molecule. Comparing with the Laplacian Matrix for the above graph, we find that:

$$[D] = \frac{K}{m} [L]$$

Eq. 3.35

This establishes a direct relation between the vibrational modes of a molecule – obtained through its Dynamical Matrix, and its structure – captured mathematically through its Laplacian Matrix

3.4 Density Functional Theory

In DFT, the ground state electron density is the primary physical quantity that can determine all the properties of the system. The ground state energy and the Hamiltonian are the functionals of the electron density. The exact form of the function has yet to be discovered, but the results achieved with these approximate forms of DFT achieve results in good agreement with experiments. For a system of interacting electrons, Density functional theory (DFT) accurately describes the total ground-state energy, as a position of the nuclei. The types of calculations in this thesis where DFT can be appropriate are for:

- i. Building molecular geometries (chapter 4) and optimized devices (Chapter 8)
- ii. Calculating Vibrational frequencies (chapter 4)
- iii. Calculating electrical properties of devices (chapter 8)

Quantum ATK is a commercial package [47] available which has been used to do DFT calculations throughout this thesis.

3.4.1 The Schrodinger Equation

The solution of the Schrodinger equation gives the ground state energy for the collection of atoms. The Schrodinger equation is the time-independent, non-relativistic equation [48],

$$\hat{H}\Psi = E\Psi$$

Eq. 3.36

The Hamiltonian consists of three terms, the kinetic energy term, the external potential, and the electron-electron interaction term. If any bias is not applied, then external potential is only the interaction of the electrons with the atomic nuclei.

$$\hat{H} = -\frac{1}{2} \sum_i^N \nabla_i^2 + V_{ext} + \sum_i^N \sum_{i \neq j}^N \frac{1}{r_{ij}}$$

Eq. 3.37

$$V_{ext} = - \sum_i^N \sum_A^M \frac{Z_A}{r_{iA}}$$

Eq. 3.38

The Hamiltonian depends on the electron (r_i) and nuclei (R_A) coordinates. The solution of the Schrodinger equation gives the wavefunction subject to the constraint that the wavefunction is anti-symmetric; they change sign if the coordinates of any two electrons are interchanged. The ground state energy E_0 is the lowest energy eigenvalue and the probability density corresponding to finding the electron in the ground state is $|\Psi_0|^2$

The expectation value of the Hamiltonian in that state gives the average energy of a state specified by Ψ [49].

$$E[\Psi] = \langle \Psi | \hat{H} | \Psi \rangle$$

Eq. 3.39

The notation $E[\Psi]$ is used to emphasize that energy is the functional of the wave function. The energy is higher than ground state energy if the wave function does not correspond to the ground state Ψ_0 . This is the variational theorem.

$$E[\Psi] \geq E_0$$

Eq. 3.40

The ground state wave function and energy can be found by minimizing the total energy. Hartree-Fock theory consists of an assumption that the wavefunction is the anti-symmetric product of the functions Ψ , each of which depends upon the coordinates of the single electron [48].

$$\Psi_{HF} = \frac{1}{\sqrt{N!}} \det [\varphi_1 \varphi_2 \varphi_3 \dots \varphi_N]$$

Eq. 3.41

Substitution of this wavefunction into the Schrodinger equation gives

$$\begin{aligned} E_{HF} = & \int \varphi_i^*(r) \left(-\frac{1}{2} \sum_i^N \nabla_i^2 + V_{ext} \right) \varphi_i(r) dr + \frac{1}{2} \sum_{i,j}^N \int \frac{\varphi_i^*(r_1) \varphi_i(r_1) \varphi_j^*(r_2) \varphi_j(r_2)}{r_{ij}} dr_1 dr_2 \\ & - \frac{1}{2} \sum_{i,j}^N \int \frac{\varphi_i^*(r_1) \varphi_j(r_1) \varphi_j^*(r_2) \varphi_i(r_2)}{r_{ij}} dr_1 dr_2 \end{aligned}$$

Eq. 3.42

The first term is the kinetic energy and external potential; the second term is the classical Coulomb interaction written in terms of orbitals, and the last term is the exchange energy. The ground state is determined by applying the variational theorem to the above energy expression under the constraint of orthonormality of orbitals [48]. These are called Hartree-Fock equation:

$$\left[-\frac{1}{2} \nabla^2 + v_{ext}(r) + \int \frac{\rho(r')}{|r-r'|} dr' \right] \varphi_i(r) + \int v_X(r, r') \varphi_i(r') dr' = \varepsilon_i \varphi_i(r)$$

Eq. 3.43

$$\int v_X(r, r') \varphi_i(r') dr' = - \sum_j^N \int \frac{\varphi_j(r) \varphi_j^*(r)}{|r-r'|} \varphi_i(r') dr'$$

Eq. 3.44

The Hartree-Fock equations describe non-interacting electrons under the influence of a mean-field potential consisting of a classical Coulomb potential and a non-local exchange potential.

The Hamiltonian operator consists of a single electron and bi-electron-dependent terms. For solving the Schrodinger equation, complete knowledge of 3N dimensional wavefunction is not required. Rather the knowledge of two-particle probability density is sufficient. The second-order density matrix is defined as,

$$P_2(r'_1, r'_2; r_1, r_2) = \frac{N(N-1)}{2} \int \Psi^*(r'_1, r'_2, \dots, r'_N) \Psi(r_1, r_2, \dots, r_N) dr_3 dr_4 \dots dr_N$$

Eq. 3.45

The diagonal elements of this density matrix are referred to as the two-particle density or pair density,

$$P_2(r_1, r_2) = P_2(r_1, r_2; r_1, r_2)$$

Eq. 3.46

$$P_1(r'_1; r_1) = \frac{2}{N-1} \int P_2(r'_1, r'_2; r_1, r_2) dr_2$$

Eq. 3.47

The total energy is given by

$$E = \int [(-\frac{1}{2} \nabla_1^2 - \sum_A^M \frac{Z_A}{r_{iA}}) P_1(r'_1; r_1)] dr_1 + \int \frac{1}{|r_1 - r_2|} P_2(r_1, r_2) dr_1 dr_2$$

Eq. 3.48

The diagonal elements of the first and second-order density matrix completely define the total energy. The problem in the space of 3N coordinates reduces to a problem in 6-dimensional space. The direct minimization of the total energy dependent on P_1 and P_2 depends on the fact that the density matrix should be legal; it must be constructed from an anti-symmetric wavefunction. The basic principle behind the density functional theory is that even the second-order density matrix is not required, and the ground state energy can be fully determined with the help of diagonal elements of the first-order density matrix- the charge density.

3.4.2 The Hohenburg-Kohn Theorems

In 1964 Hohenburg and Kohn proved the two theorems [50]; the first theorem was that the electron density determines the external potential (to within an additive constant). It immediately follows from this statement that the electron density uniquely determines the Hamiltonian operator. The first theorem can be summarised by stating that energy is the functional of the density.

The second theorem establishes a variational principle, for any positive definite trial density, ρ_t , such that $\int \rho_t(r)dr = N$, then $E[\rho_t] \geq E_0$. This theorem limits density functional theory to studies of the ground state. A slight extension allows variation to excited states that can be guaranteed orthogonal to the ground state, but to achieve this, knowledge of the exact ground state wavefunction is required.

The fundamental theorem of the density functional theorem is

$$\delta[E[\rho]] - \propto (\int \rho(r)dr - N) = 0$$

Eq. 3.49

The ground state energy and density correspond to the minimum of some functional $E[\rho]$ subject to the constraint that the system contains a correct number of electrons. The Lagrange multiplier is the electronic chemical potential \propto . There is a universal functional $E[\rho]$ that can be minimized to obtain the ground state density and energy.

The energy functional depends on a kinetic energy term, an external potential, and electron-electron interaction [48],

$$E[\rho] = T[\rho] + V_{ext}[\rho] + V_{e-e}[\rho]$$

Eq. 3.50

The form of the kinetic energy functional and electron-electron functional are unknown. To overcome this Kohn and Sham proposed an approach, a system of N non-interacting electrons to be described by N orbitals φ_i . The kinetic energy and electron density are obtained from these orbitals

$$T_s[\rho] = -\frac{1}{2} \sum_i^N \langle \varphi_i | \nabla^2 | \varphi_i \rangle$$

Eq. 3.51

This kinetic energy is not the true kinetic energy because this energy expression is for a non-interacting electron system, which reproduces the true ground state electron density;

$$\rho(r) = \sum_i^N |\varphi_i|^2$$

Eq. 3.52

The classical Coulomb's interaction or Hartree energy is the other significant component of the electron-electron interaction.

$$V_H = \frac{1}{2} \int \frac{\rho(r_1)\rho(r_2)}{|r_1 - r_2|} d r_1 d r_2$$

Eq. 3.53

The Energy functional becomes

$$E[\rho] = T_s[\rho] + V_{ext}[\rho] + V_H[\rho] + E_{XC}[\rho]$$

Eq. 3.54

$$E_{XC}[\rho] = (T[\rho] - T_s[\rho]) + (V_{e-e}[\rho] - V_H[\rho])$$

Eq. 3.55

The exchange energy is simply the error made in calculating the kinetic and electron-electron between interacting and non-interacting systems. The utility of the Density Functional theory rests on the approximation used for $E_{XC}[\rho]$.

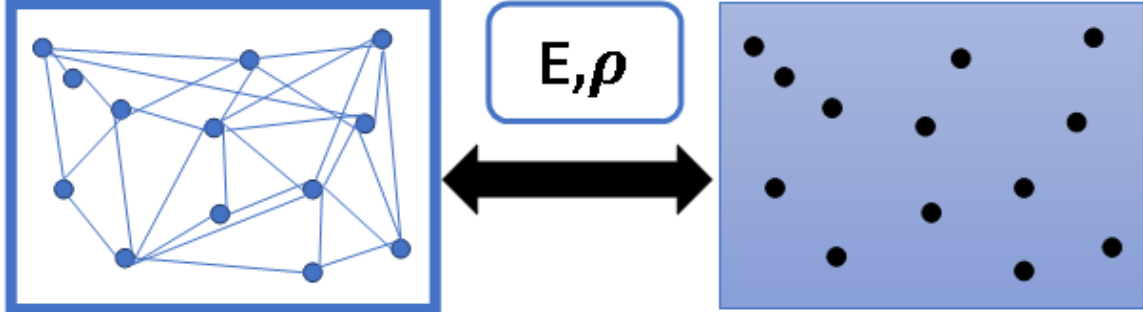


Figure 3.6: A representation of the relationship between interacting many-body system (left-hand side) and the non-interacting system of Kohn Sham density functional theory (right-hand side)

3.4.3 Approximation for Exchange-Correlation

Local Density Approximation

The local exchange-correlation energy per electron might be approximated as a function of the local charge density [48]. An approximation of the form

$$E_{XC}[\rho] = \int \rho(r) \varepsilon_{xc}(\rho(r)) dr$$

Eq. 3.56

In Local-density approximation (LDA), ε_{xc} is the exchange and correlation energy density of the uniform electron gas of density ρ . Within LDA, ε_{xc} is a function of only the local value of the charge density. It can be separated into exchange and correlation contribution:

$$\varepsilon_{xc}(\rho) = \varepsilon_x(\rho) + \varepsilon_c(\rho)$$

Eq. 3.57

The LDA has proven to be a remarkable approximation. Properties like structure, vibrational frequencies, elastic moduli, and phase stability (of similar structures) can be defined reliably for many systems. However, LDA can have significant errors in computing energy differences between different structures [48]. Nevertheless, LDA works well as it gives the reduction of the energy functional to a simple local density function.

The Generalised Gradient Approximation

The LDA is the zeroth order approximation to the semi-classical expansion of the density in terms of density and its derivatives. The natural extension to LDA would include first-order derivatives of the expansion [48]. The typical form of GGA is

$$E_{XC}[\rho] = \int \rho(r) \varepsilon_{xc}(\rho, \nabla\rho) dr$$

Eq. 3.58

The GGA significantly improves over the LDA description of the binding energy of the molecules, which leads to a wide range acceptance of DFT in the chemistry community.

Meta-GGA functional

The functionals have been developed that depend on the semi-local information in the Laplacian of the spin density or the local kinetic energy density. Such functionals are called the Meta-GGA functionals [48].

$$E_{XC}[\rho] = \int \rho(r) \varepsilon_{xc}(\rho, \nabla\rho, \nabla^2\rho, \tau) dr$$

Eq. 3.59

where τ is the kinetic energy density.

Chapter 4

4. Molecular Vibrations, Olfaction and Machine Learning

Molecular vibrations are fingerprints of the molecules that can impart information about the molecular properties, in particular biological activity, of the molecules. As discussed in chapter 3 molecular vibrations are directly related to the molecular structure, and the type of atoms present in the molecule. It is important to understand the molecular vibrations in the context of olfactory activities of the molecules. A first approximation that is made in the process of calculating odour is that the effect of the receptor is neglected and input (molecular physicochemical property) is directly mapped to the olfactory output (perception). It is also a standard practice in Quantitative Structure-Activity Relation (QSAR) studies for biochemical molecules, in contexts such as drug design, to use their vibrational spectra as a proxy to structure [51].

Now, the perception of odor has been shown to be correlated with the physico-chemical properties of odorant molecules, in particular, the atomic mass distributions therein [52]. Since the mass distribution in a molecule relates both to its shape and its vibrational spectrum, this creates a path to link the lock-and-key and the vibration pictures of olfaction. To formally unify these two, apparently orthogonal, pictures using the apparatus of Chemical Graph Theory [53], and Figure 4.1 demonstrates the formulation used to unify these theories. The odorant molecule is treated as a graph with the atoms as its nodes and attached weights corresponding to relevant atomic properties. Calculation of associated matrices then relates the structure of the graph to its functional properties, such as the vibrational spectrum – which is derived from the eigenvalues of the Laplacian matrix weighted by stiffness.

4.1 Algorithm for Odor Recognition

If odorants are sensed by the means of electron tunnelling in the biological olfactory systems (according to the Vibrational theory of Olfaction), then their tunnelling spectra, as measured by the biological detector, should correlate with their odour. Spectral comparison has three important aspects, frequency, intensity, and resolution [4].

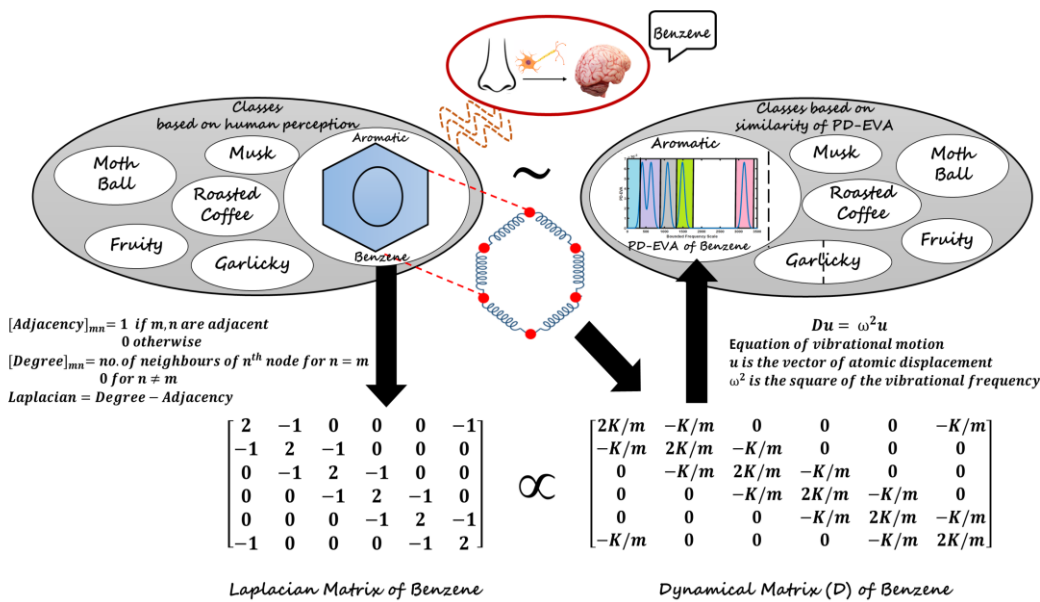
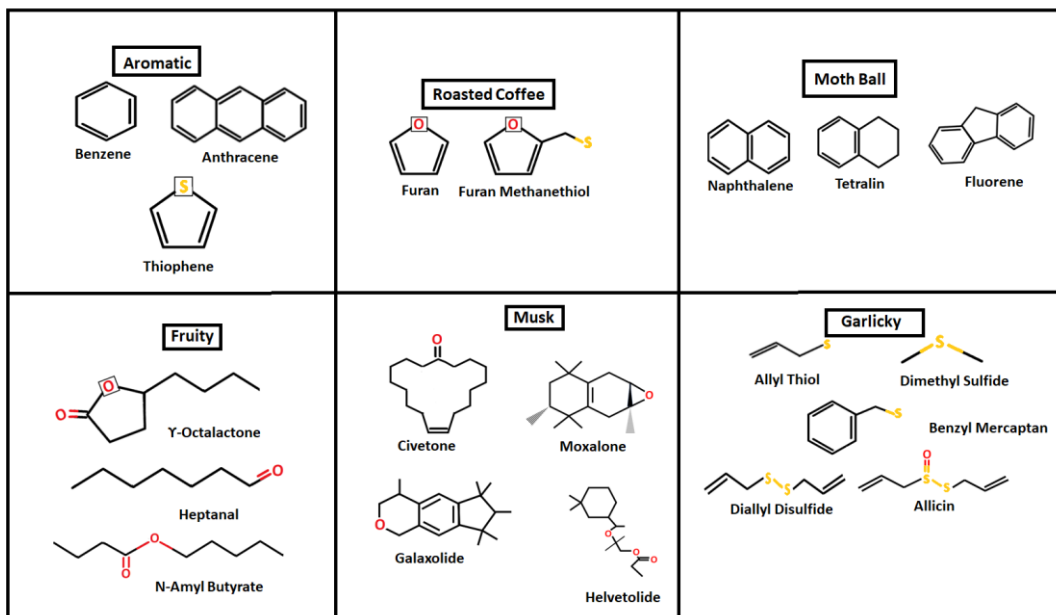


Figure 4.1: 20 odorant molecules belonging to 6 different perceptual classes are first selected, including Benzene in the *Aromatic* class (left, centre). The Laplacian Matrix (left bottom), a mathematical description of the structure, is shown (for Benzene here) to be proportional to the Dynamical Matrix D (right, bottom) – which describes the equation of vibrational motion of a molecule in terms of coupled oscillators. This mapping harmonizes the Vibrational and Shape theories of Olfaction. The eigen-frequencies of the Dynamical Matrix lead to a vibrational spectrum – the Peak-Decomposed EigenValue (PD-EVA) – with peaks corresponding to different vibrational mode types, demarcated by frequency ranges (right, centre) – shown here for Benzene. *Clustering* based on *Similarity* in the odorants' PD-EVA leads to the same classes as perceptual, with the revelation of subclasses within *Garlicky* and *Aromatic*. This mapping suggests that vibration-based odour sensing and classification may have the potential to emulate the power of biological olfaction

The frequency can be calculated using some quantum-calculation package (in this case, QuantumATK [47]) up to an accuracy of the order of 50 cm^{-1} . The IETS spectra of an odorant molecule measure by a system depends upon the resolution of the set-up and might not correlate well with the one measured by a biological system.

To begin the design of the algorithm, a small proof-of-concept experiment, a dataset of 20 odorant molecules is chosen, divided into 6 classes based on human perception of their smell. These are shown in Table 4.1 below. While smell can be complex, and somewhat subjective, there is agreement on the dominant smell of these molecules. To match the sensory input to the olfactory output, the developed algorithm should accommodate the intricacies of the actual system.

Table 4.1: Set of odorant molecules used in this study, showing their structure, and perceptual (odour) class – namely, Aromatic, Roasted Coffee, Moth Ball, Fruity, Musk and Garlicky [54].



The mathematical language for understanding the physico-chemical space (or input) is Chemical Graph Theory, which treats the nuclei as nodes and the bonds as edges of *molecular graphs* (*explained in chapter 3*). Then, usual graph-theoretic matrices (e.g. adjacency),

suitably weighted by atomic properties (e.g. mass, electronegativity), can capture the properties of molecules [53].

In particular, it is known that the Laplacian matrix of a molecular graph, when weighted by the ratio of the mechanical stiffness of the bonds to the mass of the atoms, yields its Dynamical matrix, whose eigenvalues and eigenfunctions comprise the vibrational spectrum of the molecule. This implies that the vibrational spectrum of a molecule is a characteristic property of its structure and constituents. A realistic, calculated rendering thereof is attempted by the construction of a pseudospectrum called the EigenVAlue (EVA) molecular descriptor, which is built upon the thesis that “a significant amount of information pertaining to molecular properties, in particular, biological activity, might be contained within the molecular vibration wave-function, of which the vibrational spectrum is a fingerprint” [51]. It has become a standard technique for similarity searching in chemical structure databases, strengthening the link between molecular structure, vibration, and activity through its empirical success.

Firstly, calculate the vibrational modes of the odorants using QuantumATK atomistic simulation package [47]. QuantumATK has an extensive material database of crystals and molecules, and also has a provision to build or import molecules. After the molecule is built, its geometry will be optimized for minimum energy configuration using ATK-DFT: LCAO calculator under Local Density Approximation (LDA) (discussed in Chapter 3). After obtaining the optimized structure, Dynamical matrix of these molecules is calculated as discussed in the previous chapter. The eigenvalues and eigenvectors of the Dynamical matrix are the normal modes frequencies and coordinates of the molecule respectively. The theoretical spectra calculated is compared with the reported experimental data to make the calculations consistent and reliable for further usage.

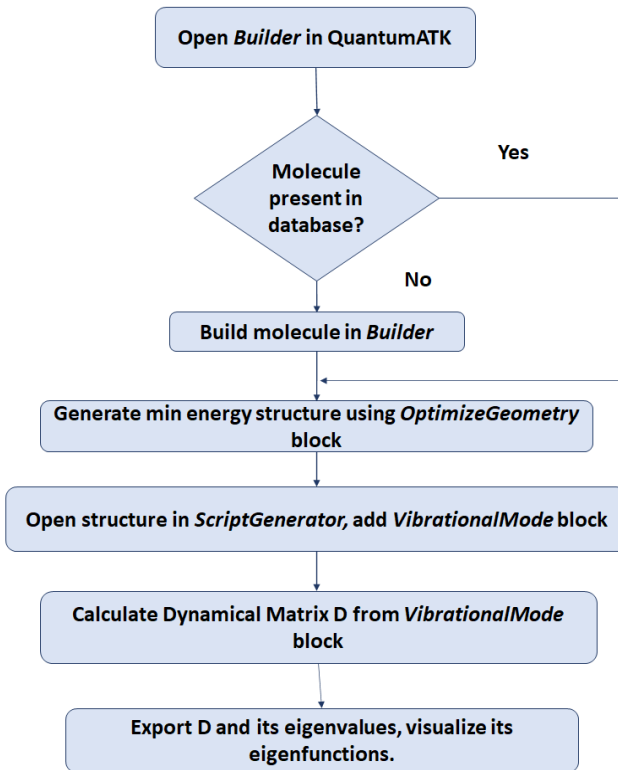


Figure 4.2: The flowchart for the calculation of the molecular vibrational spectra from the Dynamical Matrix in QuantumATK.

The eigenfrequencies have been compared for validation to available experimental data for two different molecules, as tabulated below.

Table 4.2: Vibrational Spectrum of Benzene

Calculated (in cm^{-1})	Experimental (in cm^{-1})[55]
399	405
399	405
591.86	607
592.45	671
628.79	671
703.53	703
804.5	849
805.06	849
919.92	970

920.36	970
942.89	993
977.01	999
999.33	1010
1023.17	1038
1026.32	1038
1105.81	1146
1125.04	1146
1136.64	1179
1292.19	1179
1379.44	1309
1455.01	1478
1459.95	1478
1617.44	1599
1621.02	1599
3122.8	3056
3129.92	3056
3136.45	3057
3143.7	3064
3144.47	3064
3154.7	3064

Table 4.3: Vibrational Spectrum of Allicin (data available for select modes only)

Mode	Calculated (in cm^{-1})	Experimental (in cm^{-1}) [56]
$\nu\text{S-S}$	449.39	474
γCH_2	911.62	927
γCH_2	963.49	989
$\nu\text{S=O}$	1076.67	1087
$\rho\text{ CH}_2$	1237.85	1229
$\rho\text{ C-H}$	1338.87	1319
$\delta\text{ CH}_2$	1374.84	1402
$\delta\text{ CH}_2$	1387.37	1423
$\nu\text{ C=C}$	1659.76	1635

v C-H	2989	2916
v CH ₂	2998	2978
v C-H	3061	3013
v CH ₂	3081	3083

4.2 Thermal broadening

Next, to mimic the thermal broadening of biological systems along these lines a gaussian smearing or blurring can be used. The standard deviation or the width of the gaussian is the measure of the deviation from the desired value. In understanding the link of vibrational spectra to the odor of the molecule, it is important to note that the structure of the molecule translates to vibrational modes which are then translated to some convolved spectra to get sensed by the biological system. Here the convoluted spectra originate from the gaussian convolution of the vibrational modes with some particular deviation. The spectra obtained is called EigenValue (EVA) descriptor [57]. It is a common descriptor used in Graph Theory. EVA descriptors are 3D-descriptors, independent of any molecular alignment, giving information about molecular size, shape and electronic properties. They are, moreover, only moderately dependent on conformation. They are mainly used as descriptors for QSAR and they have been shown to perform well with different data sets for prediction of biological responses [51].

The molecules with A number of atoms, the number of vibrational modes is $3A - 6$ or $3A - 5$. These frequencies are projected on a bounded frequency scale and represent them as points on the axis. A Gaussian function of some standard deviation σ is centered on each frequency which results in series of overlapping and identical Gaussians.

Then the value of EVA function at any point x on the axis is given by the contribution from each Gaussian [53],

$$EVA(x) = \sum_{i=1}^{3A-6} \frac{1}{\sigma \sqrt{2\pi}} e^{-\frac{(x-\lambda_i)^2}{2\sigma^2}}$$

Eq. 4.1

let λ_i be the i^{th} vibrational mode frequency, σ be the standard deviation.

The obtained spectra plot the multiplicity of the eigenvalues after superimposing gaussians on the frequencies projected on a bounded scale. The Gaussian function imposed is of some standard deviation σ is centered on each frequency which results in series of overlapping and identical Gaussians. The obtained plot looks like as shown in Figure 4.3.

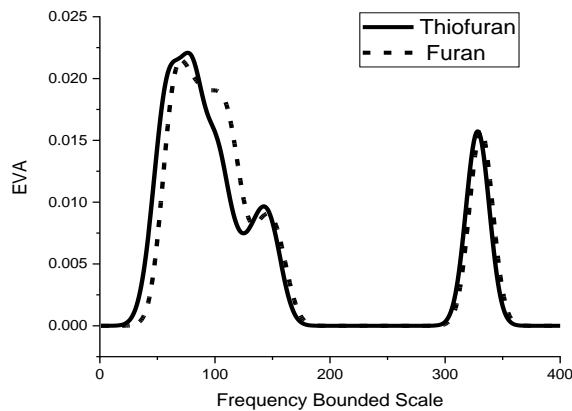


Figure 4.3: EVA plot obtained from convolution of Gaussian function.

The choice of σ defines the extent to which the fundamental vibrations overlap, these values determine the number and extent to which vibrations of a particular frequency in one structure can statistically be related to those in the other structures (inter-structural overlap); such values also govern the extent to which vibrations within the same structure may overlap at non-negligible values (intra-structural overlap). The value of standard deviation brings out the feature of the molecular graph, the smaller value of σ helps in comparing finer details whereas the bigger values bring out the global patterns of the structure more evidently [58].

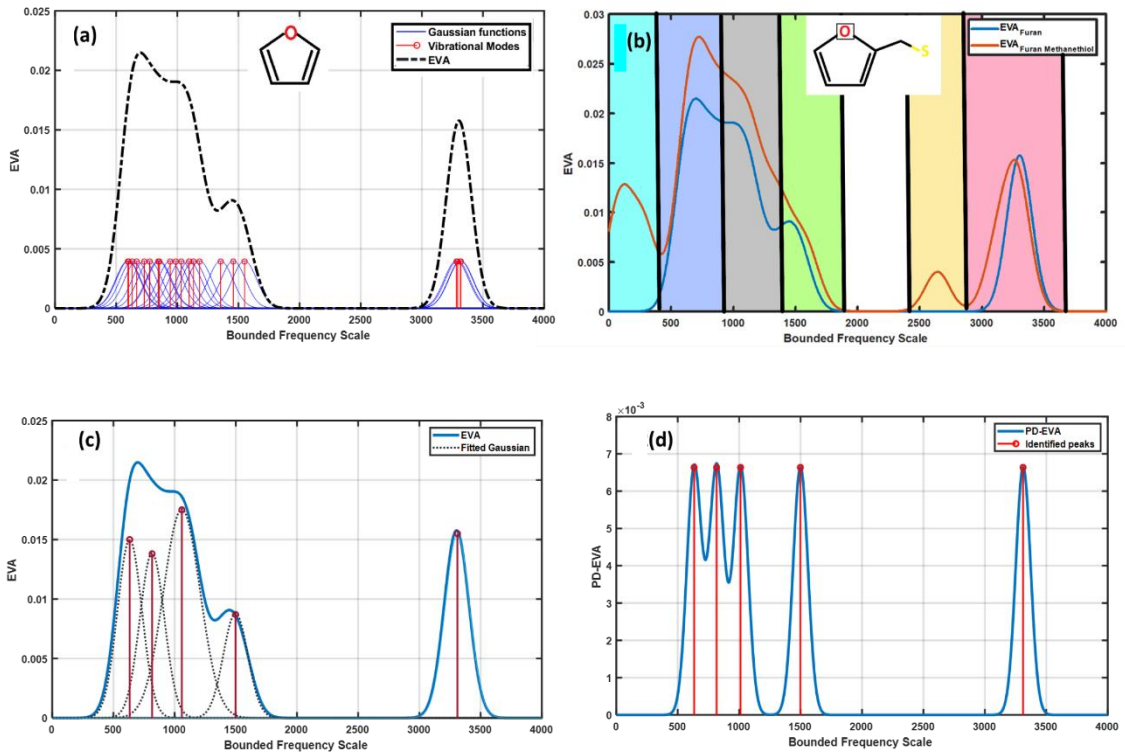


Figure 4.4 (a): The ‘EigenVAlue’ (EVA) pseudo-spectrum for the molecule Furan (shown in inset), constructed by broadening the calculated vibrational peaks (stems in red) with Gaussian functions (in blue) of suitable σ (here 100cm^{-1}) and summing up the contributions from all of them at each frequency point. (b): The EVA pseudospectrum, of Furan Methanethiol (inset) as an example, with the partitioning of the frequency scale by types of vibrational modes. From left to right: ■ Torsional modes, □ Ring Torsion and C-H rocking, ▨ Ring Deformation, C-H wagging, C-C stretch, ▢ C=C stretch, C=O stretch, ▤ S-H stretch, ▧ C-H stretch. Similar broad classification of modes can be done so the entire convolved EVA spectra can be deconvolved into broad peaks to identify the regions. This suggests the classification of odorant molecules by broad separation of the vibrational spectrum into these regions, accomplished through the ‘peak-decomposed EVA’. (c): Peak Decomposition of the EVA spectrum of Furan (shown in inset). (d): Construction of the Peak-Decomposed EVA (PD-EVA) spectrum by following the same procedure as for EVA (illustrated in Fig. 4.4(a)).

Thermal broadening presents a well-known identification problem in IETS based sensors [59] which have been sought to be alleviated by novel device designs [60]. Here the broadening is equivalent the room temperature, in fact, leads to proper odorant identification from their EVA pseudo-spectra. This suggests that: one, the “thermal broadening problem” in IETS-based sensors may not need a ‘hardware-level solution’, but can be addressed at the ‘software-level’; and two, the ‘software’ for odorant identification from vibrational peak analysis - to be presented hereafter - may, in fact, be aided by room temperature thermal broadening.

In order to develop some physical intuition, the vibrational mode types are identified, which in turn determine the frequency of the spectral peaks [61]. For example, torsional modes are typically the lowest energy ones, whereas C-H stretching modes are the highest energy. In 300K EVA pseudospectra, discrete peaks arising from the same mode type would tend to get merged together. A novel procedure to resolve the modes and generate a secondary EVA pseudospectrum carrying this information. First, the 300K EVA is decomposed by standard methods (using ‘Peak Deconvolution’ in the software Origin® [62]) into a few broad peaks - far fewer than the number of original discrete peaks started with. Dividing the frequency range into intervals, as shown in Fig. 4.4(b), then allows us to identify these broad peaks with specific mode types. Thereafter the EVA procedure is iterated as shown in Fig. 4.4(c) and 2(d), starting this time with discrete peaks (stems) positioned at the center of the above broad peaks, and using a smaller σ (60cm^{-1}) to enable finer resolution between them. This yields the secondary EVA, the Peak Deconvolved -EVA (PD-EVA) (shown for Furan in Fig. 4.4(c), for all the other molecules in Appendix)

4.3 Unsupervised Machine Learning: Odor Classification

Cluster Analysis is an unsupervised machine learning algorithm used to group and/or search for similar objects in large databases. Here, objects grouped within the same cluster should be more alike (per some well-defined measure) than those outside [63].

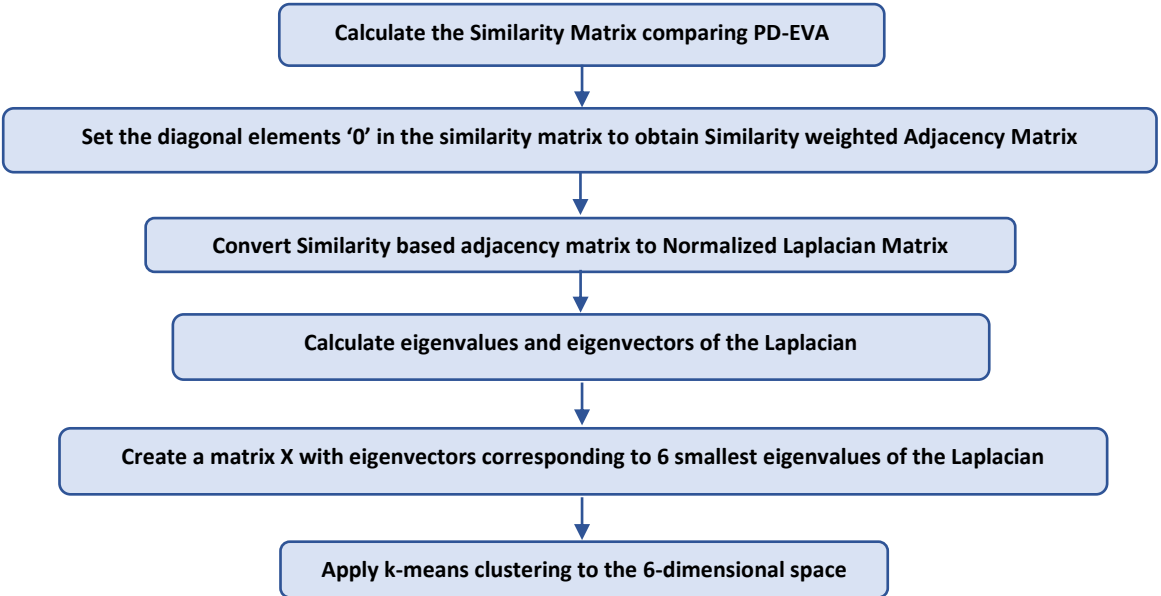


Figure 4.5: The flowchart explains the process of clustering used to classify the odorant molecules based on their PD-EVA pseudo-spectra.

In particular, a technique called Spectral Clustering is used, wherein a normalized Laplacian Matrix is calculated from an effective Adjacency Matrix - which is obtained from the Similarity Matrix by setting its diagonal elements to zero. The first ‘m’ eigenvalues and eigenvectors of this normalized Laplacian are then used to cluster the odorants into ‘m’ groups using the standard k-means algorithm.

Now, it is possible to perform a classification of odorants from their EVA pseudospectra that is based purely on data science methods, and not explicitly linked to underlying physics [64]. In order to develop a classification scheme that is informed by physical intuition, the vibrational mode types are identified, which in turn determine the frequency of the spectral peaks. After calculating PD-EVA, a measure is employed, common in QSAR techniques, to compare two EVA (or PD-EVA) spectra [53]. This measure, called the Similarity, is calculated as follows:

$$S = 2 * \frac{\sum_{i=1}^n EVA1(i) * EVA2(i)}{\sum_{i=1}^n EVA1(i)^2 + \sum_{i=1}^n EVA2(i)^2}$$

Eq. 4.2

The pairwise Similarity Indices so obtained are arranged in a nxn matrix, called the Similarity Matrix where the columns and rows correspond to the n odorant molecules under study [59]. This is then used for Cluster Analysis.

4.4 Results and Analysis

The spectral clustering provides the solution of clustering using standard linear algebra methods and mathematical concepts and so is a much more efficient algorithm. It uses the spectrum of the Similarity matrix to perform dimensionality reduction into fewer dimensions for clustering. As the eigenvalues and eigenvectors are used to perform dimensionality reduction the orthonormality of the newly created space is maintained. Initially the odor classification was performed for 17 molecules belonging to 5 odor classes shown below:

Table 4.4: Set of initial odorant molecules used in this study, showing their structure, and perceptual (odour) class – namely, Aromatic, Roasted Coffee, Moth Ball, Musk and Garlicky.

Class	Molecules
Roasted coffee	Furan, Furan Methanethiol
Moth ball	Naphthalene, Tetralin, Fluorene
Sulphurous or Garlic	Benzyl Mercaptan, Allyl Thiol, Diallyl Disulfide, Allicin, Dimethyl Sulfide
Aromatic (Benzene like)	Benzene, Thifuran, Anthracene
Musks	Civetone, Moxalone, Galaxolide, Helvetolide

Clustering on Gaussian profile with $\sigma = 10\text{cm}^{-1}$

The EVA was calculated for a standard deviation of 10 cm^{-1} and various EVA spectra were compared to obtain a Similarity index and Spectral clustering was performed to obtain six clusters:

- 1 Thiophene, Benzene
- 2 Furan, Furan methanethiol, **Allyl thiol, Benzyl Mercaptan**
- 3 Naph, Tetralin, Fluorene, **Anthracene**,
- 4 Allicin, Diallyl disulfide
- 5 Civetone, Moxalone, Galaxolide, Helvetolide

6 Dimethyl sulfide

The molecules in bold are wrongly estimated or are in wrong cluster. This clustering is inefficient and has some wrong estimation. The standard deviation of 10 cm^{-1} compares the finer details of the molecules by comparing individual peak to peak but is not physically feasible because it corresponds to very low temperature and is susceptible to conformational changes in the combined system.

Clustering on Gaussian profile with $\sigma = 100\text{ cm}^{-1}$

1. **Thiofuran**, Furan, Furan methanethiol
2. **Benzene**, Naphthalene, Tetralin, Fluorene, **Anthracene**
3. Benzyl Mercaptan, Allicin, Diallyl Disulfide
4. Allyl thiol, Dimethyl sulfide
5. Civetone, Moxalone, Galaxolide, Helvetolide

The clustering again has wrong estimations but is more physically important to explore and understand. If we observe the result, the algorithm is not able to differentiate between Thiofuran and Furan because of the slight shift in the spectrum (in appendix) and the similarity index tends to overlook this shift. Same is the case with benzene, naphthalene and anthracene, because of the similarity in local structure their EVA spectrum is very similar and algorithm is not able to differentiate that.

To overcome this or to make our algorithm susceptible to these shifts we perform the deconvolution of the EVA spectrum. The vibrational modes are the eigenvalues of the Dynamical matrix and are not just numbers but have some inherited properties of the molecular structure stored in them. The region of the spectrum in which the mode is present defines the type of vibration it indicates. The vibrational frequencies depend upon the stability, mass and structure of the bond present in a molecule. Higher stability of the bond higher is the frequency; evidently torsional modes are the lowest energy modes and C-H stretching modes are the highest energy modes. Similar broad classification of modes can be done so the whole convolved EVA spectra can be deconvolved into broad peaks to identify the regions. If a single molecule activates multiple receptors to create a whole spectrum to map that spectrum to smell in the brain, this deconvolution might give a very rough idea of the multiple activation.

This method is now applied to cluster the 20 odorant molecules into physical (vibrational) classes based on the Similarity in their PD-EVA spectra. The 20 odorant molecules we chose, belong to 6 different classes of smell from different walks of everyday life, namely roasted coffee, garlic, musk, fruity, aromatic and moth ball. The molecules included have different structures to make this study comprehensive. The optimal clustering leads to 8 physical classes, in contrast to the 6 perceptual ones (something similar was also observed earlier [60]. However, the molecules in each physical class do smell the same. It transpires that two of the six perceptual classes split into two in the process of physical (vibration-based) clustering. This will be elucidated in the following paragraph. Table 4.5 lists the molecules in bands indicating the physical classes, the perceptual class (i.e. smell) for each molecule, and its dominant vibrational modes obtained through peak decomposition of its EVA pseudospectrum.

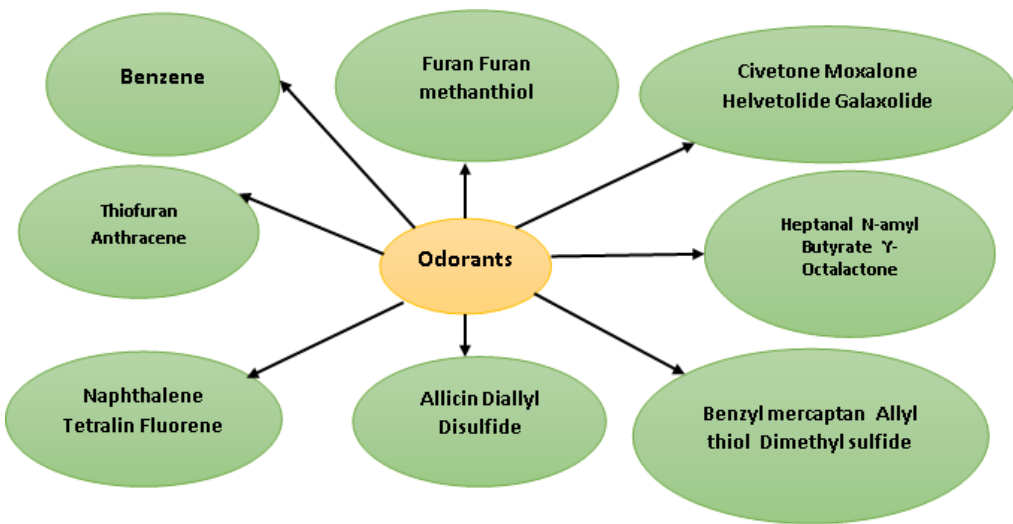


Figure 4.6: the clusters obtained in spectral clustering. The molecules in same cluster have similar smell.

In fact, these classes correspond to a natural subgrouping of the perceptual class, namely ‘weakly aromatic’ and ‘strongly aromatic’ [24]. The ‘garlicky’ perceptual class (last in Table 4.5) is also found to split into 2 physical classes; again, this is found to correspond to natural perceptual sub-classes. Allicin and diallyl disulfide occur naturally in garlic and are responsible for its odor, whereas benzyl mercaptan, dimethyl sulfide, and allyl thiol are synthetic molecules which are perceived as sulfurous-garlic [54]. It is intriguing that a purely mathematical clustering algorithm, using a descriptor originating from molecular vibrational

modes, is able to resolve the perceptual subclasses. This indicates that classification and identification of odorant molecules based on intricate information about their vibrational spectra, can effectively emulate biological olfaction and enable biomimetic olfactory sensors.

Table 4.5: Molecules with their Perceptual classes and the dominant vibrational modes (in cm^{-1}) identified by peak-decomposition of EVA pseudo-spectrum. A, B: Low-frequency torsional modes. C, D: Ring torsion and C-H rocking. E, F: Ring deformation, C-H wagging, and C-C stretch. G: C=C stretch. H: C=O stretch. I: S-H stretch. J: C-H stretch.

Molecule	Odor Perception	A	B	C	D	E	F	G	H	I	J
Benzene	Aromatic (Strong)			399	637		1084	1485			3189
Anthracene	Aromatic (Weak)				615	826	1147	1446			3206
Thiofuran	Aromatic (Weak)				538	758	1043	1424			3258
Furan	Roasted Coffee				633	816	1011	1498			3311
Furan methanethiol	Roasted Coffee	157			684		1025	1526		2650	3251
Naphthalene	Moth-ball	151		441		842	1150	1515			3213
Tetralin	Moth-ball	118		468		827	1147	1471			3080
Fluorene	Moth-ball	137		463		871	1126	1456			3193
Heptanal	Fruity	79				883	1287		1817		3046
N-amyl Butyrate	Fruity	118				846	1157	1386	1780		3066
γ -Octalactone	Fruity	112				820	1263		1816		3066
Civetone	Musk		240				1044	1377			3009
Moxalone	Musk		292				993	1370			3029
Galaxoltide	Musk		318				989	1373			3035
Helvelotide	Musk		280				999	1359			3029
Benzyl Mercaptan	Garlicky (artificial)		260			881	1091	1454		2585	3193
Allyl thiol	Garlicky (artificial)		272				927	1313	1696	2602	3086
Dimethyl sulfide	Garlicky (artificial)		226			885		1371			3051
Diallyl disulfide	Garlicky (natural)	110		439			922	1254	1724		3070
Allicin	Garlicky (natural)	120		382			958	1313	1692		3109

4.5 Conclusion

In conclusion, we have used Chemical Graph Theory to illuminate the link between molecular structure and vibrational spectra that is implicit in QSAR studies based on the EVA molecular descriptor. This is consistent with earlier work [48] suggesting that, of numerous physicochemical properties, the most crucial ones contributing to the complex perception of

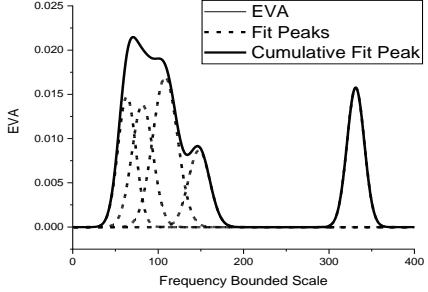
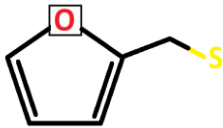
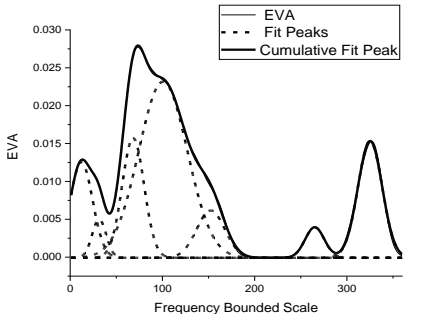
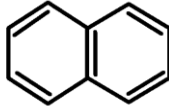
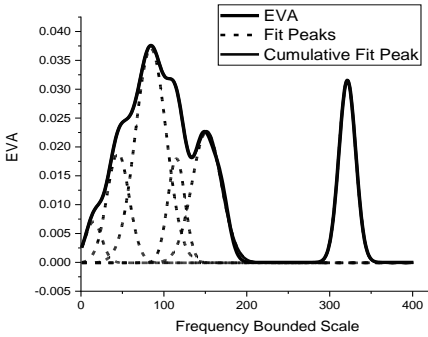
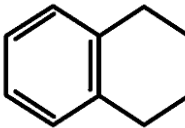
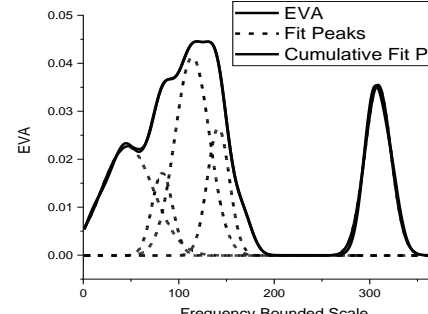
smell are molecular mass and its distribution – which naturally connect to its vibrational spectra in the framework of Chemical Graph Theory. A novel vibrational pseudo-spectrum called the PD-EVA was introduced, which incorporates physical insight about vibrational mode types. A small, proof-of-concept set of 20 odorant molecules, belonging to 6 perceptual classes are classified into physical (vibrational) by Spectral Clustering based on Similarity between their PD-EVA. It is found that the best clustering leads to 8 physical classes, corresponding to the perceptual ones, plus one subclass each that was inherent in 2 of the perceptual classes and revealed in the clustering process. With this mapping, PD-EVA places vibration-based odour classification on a firm physical foundation, which was missing in earlier EVA-based clustering [64]. Thereby it strengthens the thesis that Vibration plays a non-trivial role in Olfaction. It also suggests that the power of biological olfaction may be possible to emulate with vibration-based sensing and identification. This certainly bears verification with much larger odorant data sets, which must be the subject of future work. Nonetheless, we remind ourselves that biophysical models, even if simplistic or incomplete, have proven highly effective in guiding the development of useful bio-inspired technologies, e.g. learning using neural networks. This work could thus guide the development of a quantum biomimetic electronic nose, where the path to realizing a practical vibration/IETS based sensor system [16] seems clearer than it is for sensors based on many other physicochemical properties.

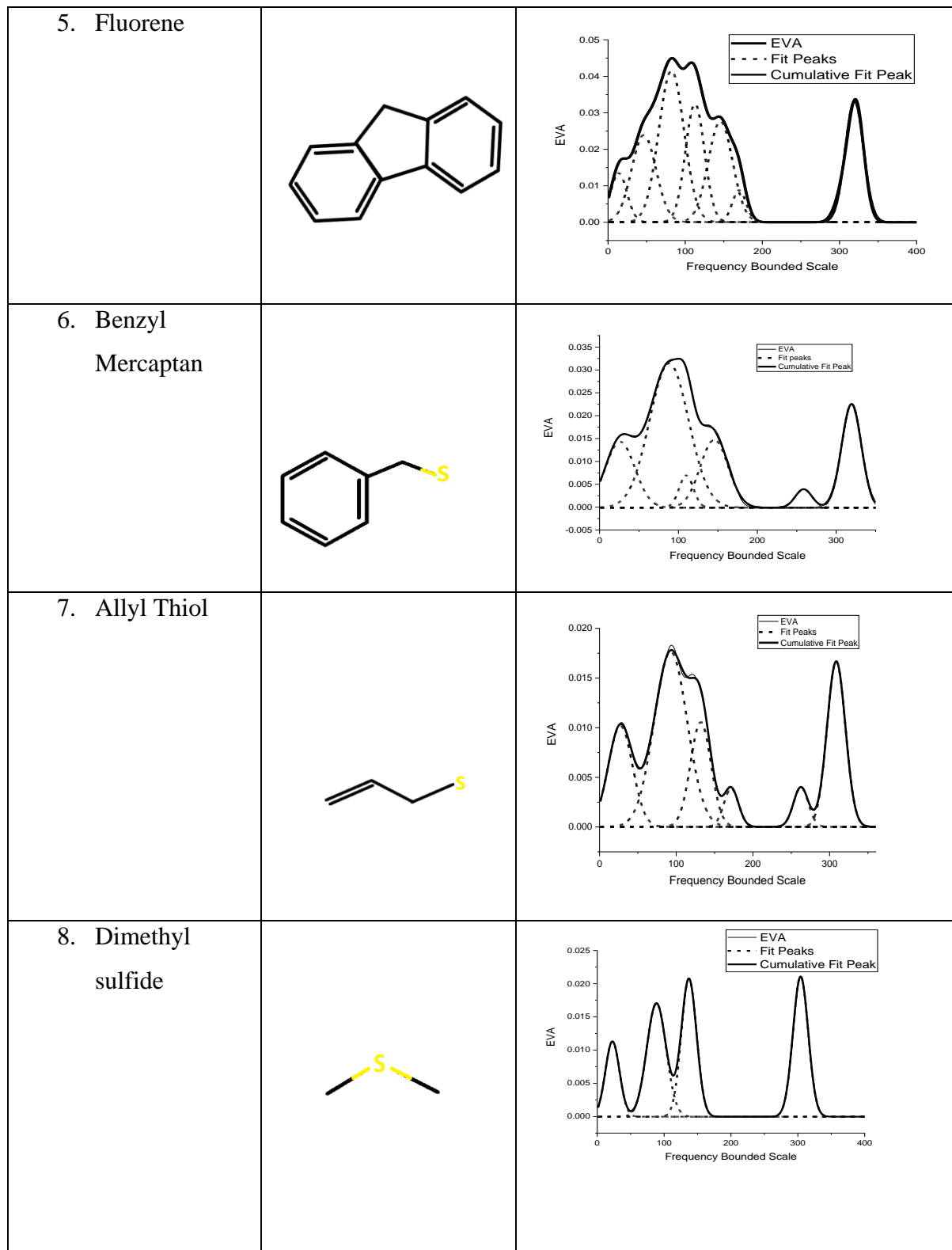
4.6 Appendix

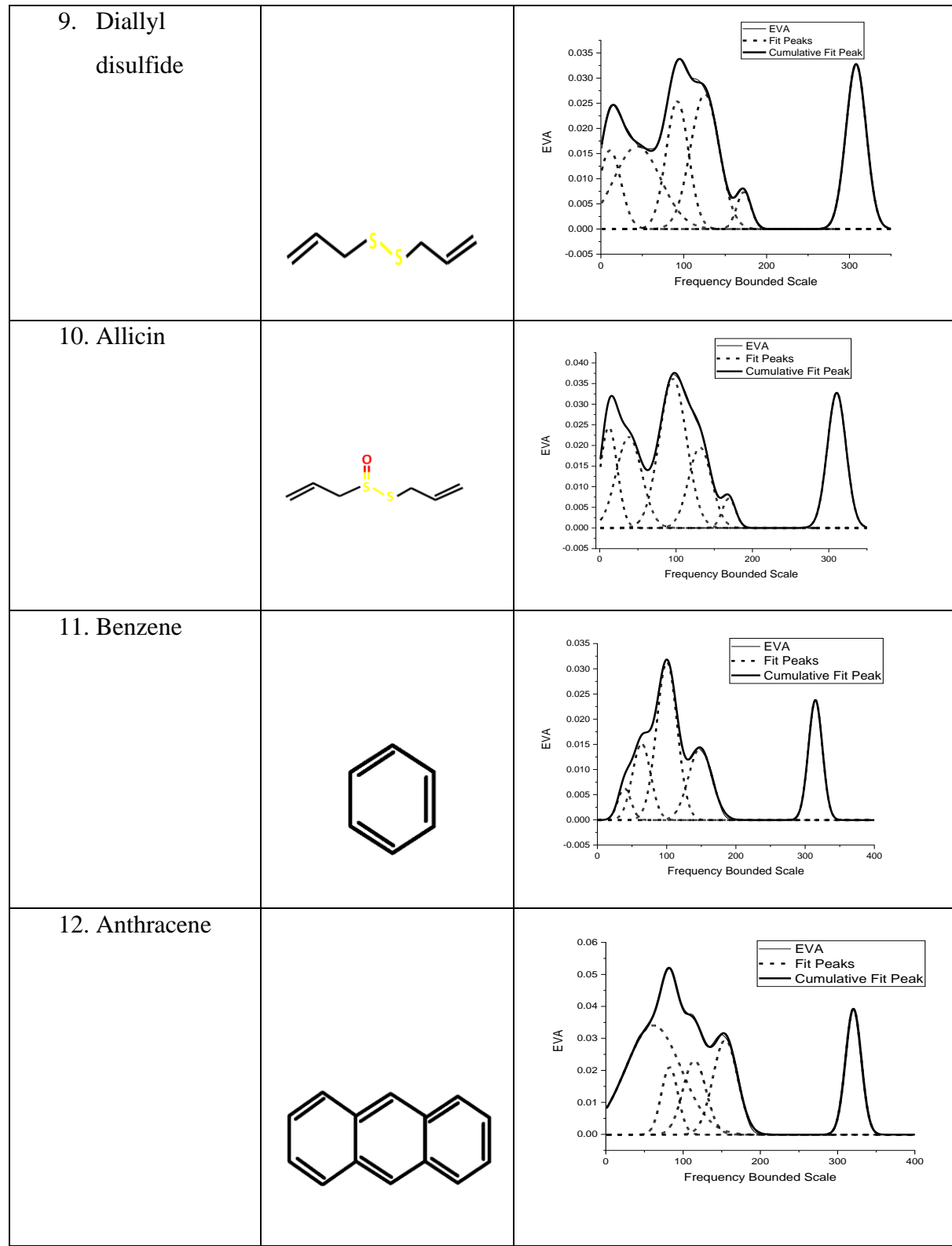
Molecular EVA and PD-EVA

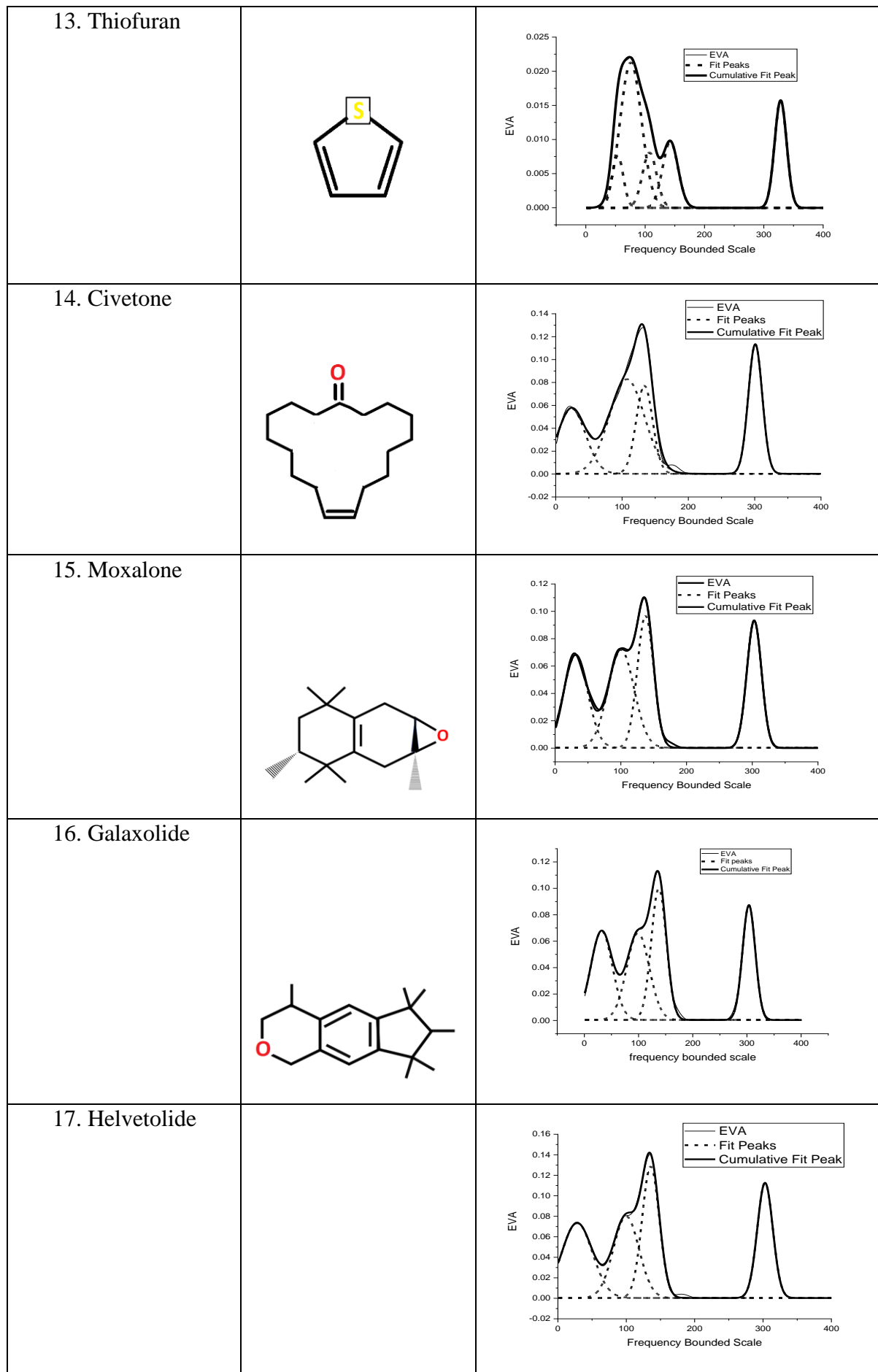
The structure of all 20 molecules studied here, along with their EVA and peak decomposition (for generating PD-EVA) is shown below.

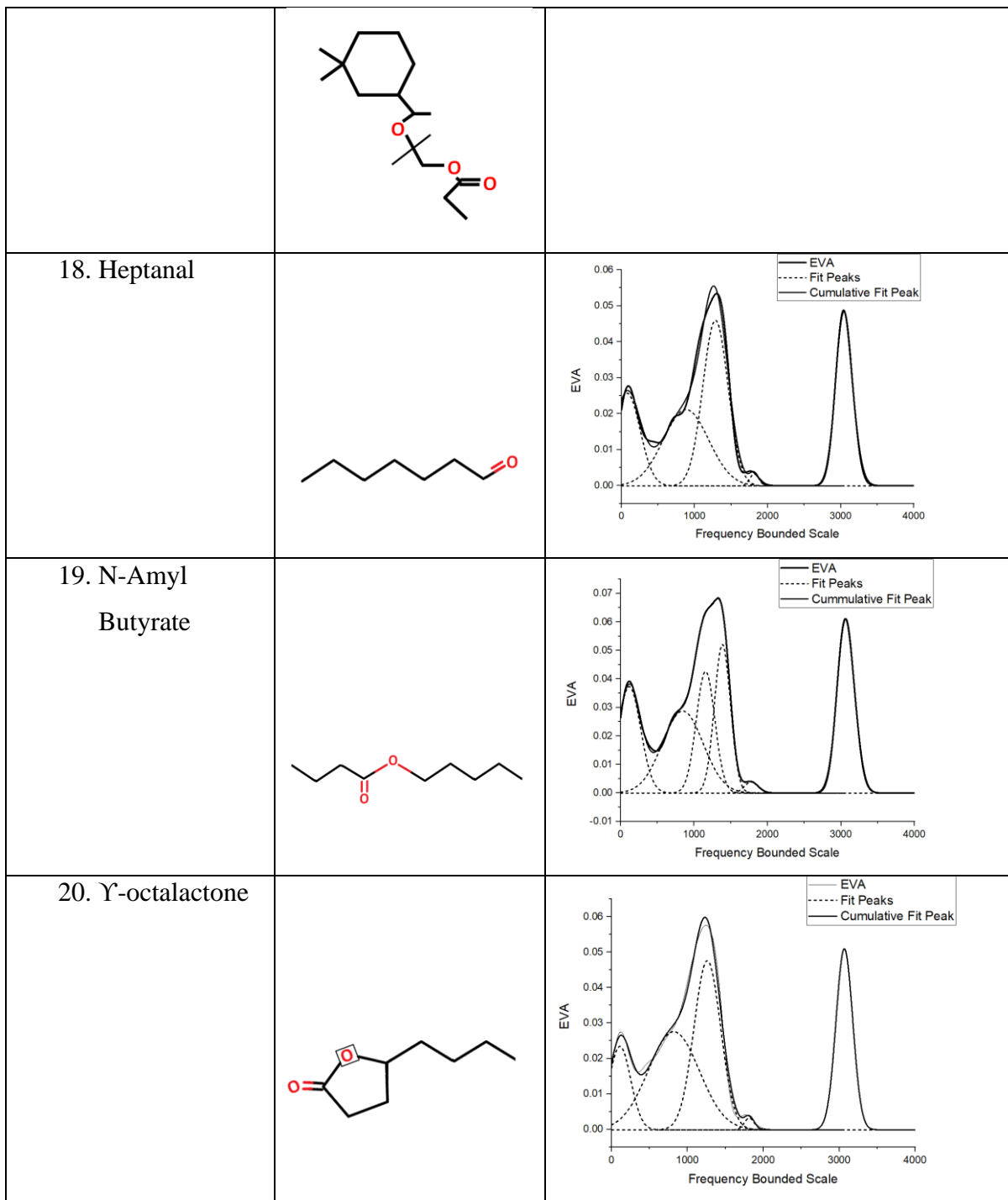
Table 4.6: Molecular structure of all 20 molecules with their EVA and peak decomposition (for generating PD-EVA)

Molecule	Structure	EVA, PD-EVA
1. Furan		
2. Furan Methanethiol		
3. Naphthalene		
4. Tertalin		









Chapter 5

5. Chirality Induced Spin Selectivity (CISS)

This chapter introduces Chirality and theory around enantio-selection in bio-recognition, Chirality Induced Spin Selectivity (CISS). It also explains Symmetry Adapted Perturbation theory (SAPT), which elucidated the path for including spin in charge polarization and making the process enantioselective. This chapter tries to look beyond the shortcomings of VTO.

5.1 Chiral molecules

In 19th century, it was found that some molecules had the property of rotating the plane of polarization of the beam of light incident on them. The direction in which the plane of polarisation has rotated after the light has gone through the substance allowed scientists to classify these molecules as optically active and determine whether they are dextrorotatory or levorotatory. Dextrorotatory substances rotate the plane of polarization clockwise to the observer in relation to the incoming light beam, whereas levorotatory substances rotate the plane of polarization anticlockwise [65]. It was later explained that the origin of this property lies in the geometrical construct of these molecules, called chirality. Chiral molecules are non-superimposable mirror image of each other, so chiral molecules have two distinct configurations corresponding to each image, called enantiomers. The left handed molecule will rotate the plane of polarization in clockwise direction while the right-handed molecule will rotate the polarization in the anti-clockwise direction. The chirality of a molecule is identified by its geometrical construct of left or right handedness as well as the rotation of the plane of polarization of the light beam [66].

The following describes the physical process that causes optical activity: a linearly polarised light beam moving in the z-direction has its polarisation vector in the x-y plane.. The state of the initial light is $|\theta\rangle$, θ indicates the angle between the polarization vector and x-axis. Now

$|\theta\rangle$ can be written as a superposition of right circularly polarized $|R\rangle$ and a left circularly polarized $|L\rangle$ light as follows,

$$|\theta\rangle = \frac{1}{\sqrt{2}}(e^{i\theta}|R\rangle + e^{-i\theta}|L\rangle)$$

Eq. 5.1

the speed of light is different for left and right components in an optically active medium. So after passing through the medium the outgoing beam will become,

$$|\theta'\rangle = \frac{1}{\sqrt{2}}(e^{i(\theta+\delta)}|R\rangle + e^{-i(\theta+\delta)}|L\rangle) = |\theta + \delta\rangle$$

Eq. 5.2

The polarization of the outgoing light beam is $\theta + \delta$. The light beam has electric and magnetic fields which interact with the electric and magnetic dipole moments of the molecule and produce a particular type of response.

5.1.1 Manifestation of chirality

Chiral molecules form the building block of life in the form of proteins, amino acids and DNA. Now, it is difficult to distinguish enantiomers artificially—chirality can only be discerned by a probe that is itself chiral. Nonetheless, nature seems to have ways to isolate them, and important biochemical processes are known to be enantioselective [67]. The response of human senses, except the ear, is influenced by the chirality of the molecule [68].

In the present context, chirality ('handedness') is a property of molecules that seems to be relevant in many chemical and biochemical (life) processes [69]. In the food flavoring industry, many essential oils or spices are derived from natural resources. It is a challenge to authenticate these natural extracts as they occur in nature as racemic mixtures, viz. a mixture of equal amounts of enantiomers [70]. Information about chirality is also important in

medicinal drug molecules since these too often occur as racemic mixtures, wherein one enantiomer can be active and the other can be inactive (or worse, could have side-effects, or even be toxic). Enantiomers, being chiral molecules that are non-superimposable mirror images of each other, are structurally identical up to a lateral inversion. Differing sensitivity of (bio)chemical processes to different chirality is termed ‘enantioselectivity’. How it arises, and the role it plays in biology constitute topics of contemporary research [71]. This is driven in significant part by interest in the design and synthesis of drug molecules for the reason mentioned above.

5.1.2 Chirality Induced Spin Selectivity (CISS)

While optical activity can be described as the filtering of photons by chiral molecules, CISS, on the other hand, describes the filtering of the spin of electrons by chiral molecules. The phenomenon of Chirality Induced Spin Selectivity (CISS) features spin polarization along with charge polarization induced by the handedness of molecules. An electron traverses more or less easily through a chiral molecule depending upon the spin of the electron and the chirality of the molecule. This spin selectivity arises from the coupling of spin with the linear momentum - called Spin-Orbit Coupling - which can be of either the Dresselhaus [72] or Rashba types [73], due to bulk and structure inversion asymmetry, respectively. As chiral molecules do not have structural symmetry, Rashba type SOC is the dominant contribution to the Hamiltonian. This effect favors one spin orientation over the other and gives rise to spin-dependent transmission.

Spin selectivity is an exciting prospect for technological applications and several recent developments, both experimental and theoretical, have shown that the CISS effect has a significant amount of spin-selectivity [74]. The first experiment is electron transmission measurements, a strong demonstration of CISS was made in a photoelectron transmission experiment using an Au(111) substrate and an adsorbed monolayer of thiolated double-stranded DNA (dsDNA) molecules. The outcomes show a spin polarisation of up to -60% in the normal direction [75]. Furthermore, the polarisation of the X-rays utilised to irradiate the sample had no effect on the spin-polarization of the electrons. Additionally, it was discovered that the length of the dsDNA molecules increased the spin polarisation.

The first observation of CISS in a conductance setup is described by Xie et al. [76]. Here, gold nanoparticles and ferromagnetic Ni surfaces are joined by dsDNA molecules, and the latter is attached to an AFM tip. Adsorbed onto the Ni surface and thiol-bonded to the Au nanoparticle are single-stranded DNA (ssDNA) molecules. A connection between the AFM tip and the surface is created when the ssDNA linked to the tip is brought close to a complementary strand on the surface. The next step was to make spin-dependent conductance measurements by adjusting the bias across the junction and the magnetization of the Ni substrate. The outcomes demonstrated that the two spin orientations have a significantly different conductance.

5.1.3 Rashba SOC

From special relativity it is known that, if we have an electrostatic field E in one reference frame, it will give rise to a magnetic field $B = \frac{1}{c^2} E \times v$ in a frame moving with velocity $v \ll c$ with respect to the lab frame [77]. In its rest frame, an electron experiencing an electric field experiences a magnetic field. The interaction between the electron's spin magnetic moment and this magnetic field is known as spin-orbit interaction. The Hamiltonian for the helical structure with Rashba type spin orbit coupling

$$H = \frac{p^2}{2m} + \frac{\alpha}{\hbar} (\sigma_y p_x - \sigma_x p_y)$$

Eq. 5.3

Convert this into helical coordinates [78]

$$x = a \cos \xi \Phi \quad y = a \sin \xi \Phi \quad z = b \Phi \quad 0 \leq \Phi \leq 2N\pi$$

where a is the radius, b is the pitch, N is the no of turns in helix and ξ is the handedness of the helix ($\xi = +1$ right handedness; -1 for left handedness)

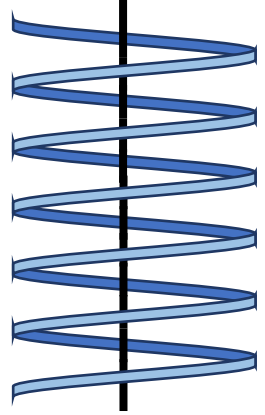
$$H = \frac{p_\Phi^2}{2m(a^2 + b^2)} - \frac{\alpha a}{\hbar(a^2 + b^2)} (\sigma_\rho p_\Phi) + \frac{i\alpha a}{2(a^2 + b^2)} \sigma_\Phi$$

Eq. 5.4

where σ_ρ and σ_Φ are the Pauli spin matrices in cylindrical coordinates

$$\text{Let } \omega_o = \frac{\hbar}{m(a^2+b^2)} \text{ and } \omega_{so} = \frac{2\alpha a}{\hbar(a^2+b^2)}$$

Converting Hamiltonian into quadratic form



$$H = \frac{\hbar\omega_o}{2} \left(i\partial_\Phi + \frac{\omega_{so}}{2\omega_o} \sigma_\rho \right)^2$$

Eq. 5.5

To solve this equation, consider

$$h = \left(i\partial_\Phi + \frac{\omega_{so}}{2\omega_o} \sigma_\rho \right)$$

Eq. 5.6

And the wavefunction in form spinors

$$\psi_{n,s}^{\lambda,\xi} = \exp(i\lambda \frac{n}{2N} \xi \Phi) \frac{A e^{-i\xi\Phi/2}}{B e^{i\xi\Phi/2}}$$

Eq. 5.7

Solving h,

$$\varepsilon = \frac{n}{2N} - \frac{s\lambda\xi}{2} \sqrt{1 + \left(\frac{\omega_{so}}{\omega_o}\right)^2}$$

Eq. 5.8

$$E_{n,s}^{\lambda,\xi} = \frac{\hbar\omega_o}{2} \left(\frac{n}{2N} - \frac{s\lambda\xi}{2} \sqrt{1 + \left(\frac{\omega_{so}}{\omega_o}\right)^2} \right)^2$$

Eq. 5.9

where $s(\pm 1)$ is spin, $\lambda (\pm 1)$ is the direction of propagation and $\xi (\pm 1)$ is the chirality index

If $\alpha=0$ no spin orbit coupling $E_{n,s}^{\lambda,\xi} = \frac{\hbar\omega_o}{2} \left(\frac{n}{2N} - \frac{s\lambda\xi}{2} \right)^2$

Time reversal symmetry, $E_{n,s}^{\lambda,\xi} = E_{n,-s}^{-\lambda,\xi} = \frac{\hbar\omega_o}{2} \left(\frac{n}{2N} - \frac{s\lambda\xi}{2} \right)^2$

if we fix the chirality $\xi=+1$,

$$E_{n,s}^{\lambda,+} = \frac{\hbar\omega_o}{2} \left(\frac{n}{2N} - \frac{s\lambda}{2} \right)^2$$

This energy is four-fold degenerate

1) For $\lambda=+1$ and $s=-1$ $E_{n,-}^{+,+} = \frac{\hbar\omega_o}{2} \left(\frac{n}{2N} + \frac{1}{2} \right)^2$

2) For $\lambda=-1$ and $s=+1$ $E_{n,+}^{-,+} = \frac{\hbar\omega_o}{2} \left(\frac{n}{2N} + \frac{1}{2} \right)^2$

3) For $\lambda=+1$ and $s=+1$ $E_{\frac{n}{2N}+1,+}^{+,+} = \frac{\hbar\omega_o}{2} \left(\frac{n}{2N} + \frac{1}{2} \right)^2$

$$4) \text{ For } \lambda=-1 \text{ and } s = -1 \quad E_{\frac{n}{2N}+1,-}^{-,+} = \frac{\hbar\omega_0}{2} \left(\frac{n}{2N} + \frac{1}{2} \right)^2$$

If $\alpha \neq 0$, the degeneracy is lifted and the energy level splits into a low energy configuration and high energy configuration. For $\xi=+1$, if we choose a particular direction of propagation $\lambda=+1$, then for spin down $s=-1$

$$E_> = \frac{\hbar\omega_0}{2} \left(\frac{n}{2N} + \frac{1}{2} \sqrt{1 + \left(\frac{\omega_{so}}{\omega_0} \right)^2} \right)^2$$

Eq. 5.10

spin up $s=+1$

$$E_< = \frac{\hbar\omega_0}{2} \left(\frac{n}{2N} + 1 - \frac{1}{2} \sqrt{1 + \left(\frac{\omega_{so}}{\omega_0} \right)^2} \right)^2$$

Eq. 5.11

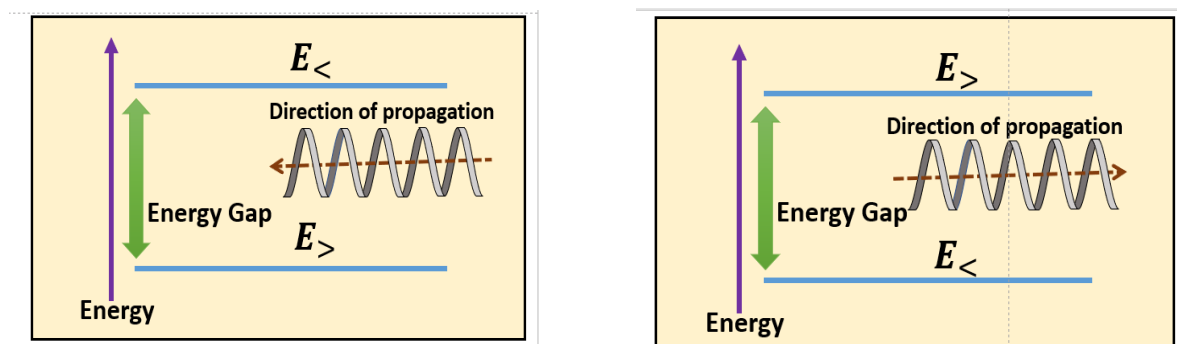


Figure 5.1: The splitting of energy of up-spin and down spin electrons due to chirality of the channel and choosing the direction of propagation.

5.1.4 SOI as a phase

The Hamiltonian contains the spin-orbit coupling due to structure inversion asymmetry. To look at this Hamiltonian in a new perspective, operators are introduced,

$$\hat{H} = -\frac{\hbar^2 \nabla^2}{2m} + V + V_{SOC}(r)$$

Eq. 5.12

$$V_{SOC}(r) = -\frac{\alpha}{\hbar} \boldsymbol{\sigma} \cdot (\mathbf{E} \times \hat{\mathbf{p}})$$

Eq. 5.13

$$\hat{\mathbf{A}} \equiv \frac{\hbar}{2mc^2} (\boldsymbol{\sigma} \times \mathbf{E})$$

Eq. 5.14

under the unitary transformation, $U = e^{i\Omega}$ where, $\nabla\Omega = \frac{qA}{2\hbar}$

The Hamiltonian becomes

$$\hat{H}' = -\frac{\hbar^2 \nabla^2}{2m} + V - \frac{A^2}{8m}$$

Eq. 5.15

Since \hat{H}' is diagonal in spin space, it follows that in a purely electrostatic field, the Hamiltonian can be transformed to a form where the effects of spin-orbit interaction are entirely incorporated into the unitary operator \hat{U} . The unitary operator has a phase which a

particle acquires a geometric phase in the presence of a magnetic vector potential moving along a path. [79]

For a simple 2-D channel, Figure 5.2, it can be shown that Spin-orbit coupling adds an imaginary term in the Hamiltonian. The resulting Hamiltonian is Hermitian but is not symmetric which opens up spin polarization depending upon the direction of the transport (or in this case depending upon the chirality of the system).

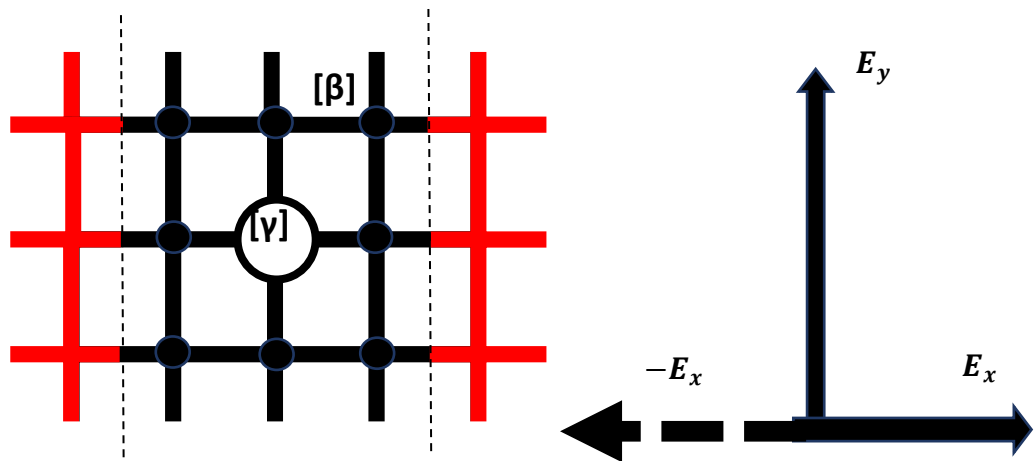


Figure 5.2: (a) shows the 2d channel with γ as onsite energy, (b) field used to probe the chirality of the channel

The polarization is given by

$$P_z = \frac{TMd - TMu}{TMd + TMu}$$

Eq. 5.16

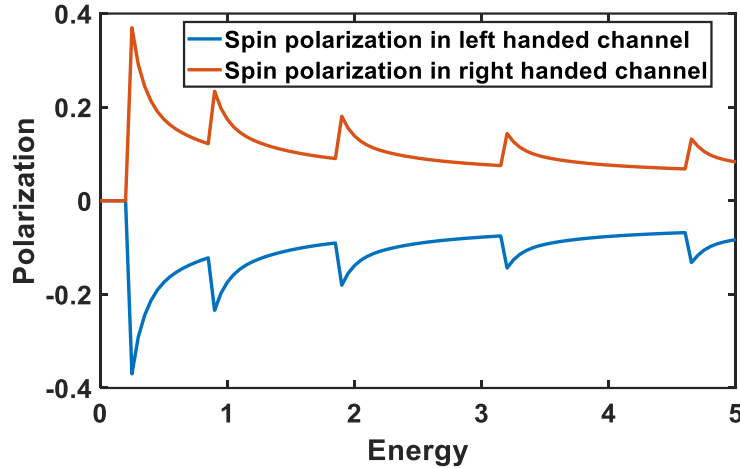


Figure 5.3: Spin Polarization in chiral channel (spin polarity gets reversed on reversing the chirality of channel)

5.2 Intermolecular Forces

Currently the most widely accepted version is that the smell depends on both shape/size and vibrational energies of the odorant molecule. According to shape/docking theory, the intermolecular interaction (electrostatic and van der Waals) energies between odorant and reception molecules is responsible for the odor. In this chapter, SAPT approach to calculate intermolecular interaction energies between molecules has been studied extensively.

5.2.1 Types of Intermolecular Energies

On a fundamental level, intermolecular interaction energies can be classified as follows [80]:

- Electrostatics: The Coulomb interaction between isolated molecules' charge strengths (monomers). Each charge density consists of a continuous electron density and discrete nuclear charges. Electrostatics causes interactions between the monomers' permanent multipole moments (a charge, dipole, quadrupole, etc.) at large distances between them; at small distances this also includes the charge penetration effects brought on by the overlap of electron densities.
- Induction: The energetic result of the two molecules' mutual polarisation. The isolated molecule A's electric field polarises molecule B, and vice versa, producing

the leading order induction term. When two molecules are far apart, induction mostly consists of interactions between the induced multipole moments on one of the molecules and the permanent multipole moments on the other, with the latter depending on static and hyperpolarizabilities.

- Dispersion: Typically, correlated electron density fluctuations on both molecules are used to describe how intermonomer electron correlation affects both molecules. Even nonpolar molecules and uncommon gas atoms can form a weak bond with any two systems because to the alluring effect of dispersion. The dynamic polarizabilities of the two molecules' assessed imaginary frequencies are related to dispersion energy at long range.
- Exchange: A result of the Pauli exclusion principle that has a short-range repelling power. Exchange is the main cause of short-range repulsion between molecules and vanishes exponentially with distance, precisely like the overlap of two electron concentrations. The effects of induction and dispersion are also short-range quenched by exchange.

5.2.2 Rayleigh Schrodinger Perturbation Theory

The intermolecular energy operator V in the standard Rayleigh Schrödinger perturbation expansion is given as:

$$V = \sum_{\alpha \in A, \beta \in B} \frac{Z_\alpha Z_\beta}{R_{\alpha\beta}} + \sum_{i \in A, \beta \in B} \frac{Z_\beta}{R_{i\beta}} + \sum_{\alpha \in A, j \in B} \frac{Z_\alpha}{R_{\alpha i}} + \sum_{i \in A, j \in B} \frac{1}{R_{ij}}$$

Eq. 5.17

Notation: In the above expression, the indices i and j represent the electrons whereas the indices A and B represent the nuclei of the monomers. Z_X is the atomic number of nucleus X and R_{XY} is the distance between particles X and Y .

The Schrödinger equations for the unperturbed monomers A and B can be solved precisely in this method. Thus, the interaction energy between two monomers defined by their full-configuration interaction (FCI) wavefunctions is determined using Symmetry Adapted Perturbation Theory (SAPT).

In SAPT (FCI) approach, the zeroth-order (unperturbed) Hamiltonian is the sum of Hamiltonians of individual monomers A and B, i.e. $H_0 = H_A + H_B$. If Ψ_A and Ψ_B are the FCI wavefunctions of monomers A and B respectively, then we get the following relations:

$$H_A \Psi_A^{(0)} = E_A^{(0)} \Psi_A^{(0)}$$

Eq. 5.18(a)

$$H_B \Psi_B^{(0)} = E_B^{(0)} \Psi_B^{(0)}$$

Eq. 5.18(b)

$$\Psi^{(0)} = \Psi_A^{(0)} \Psi_B^{(0)}$$

Eq. 5.18(c)

$$E^{(0)} = E_A^{(0)} + E_B^{(0)}$$

Eq. 5.18(d)

If N_A and N_B are number of electrons in isolated molecules A and B, then zeroth order wavefunction of system $\Psi^{(0)}$ is given by the expression below:

$$\Psi^{(0)}(1, \dots, N_A + N_B) = \Psi_A^{(0)}(1, \dots, N_A) \Psi_B^{(0)}(N_A + 1, \dots, N_A + N_B)$$

Eq. 5.19

The resultant wavefunction is antisymmetric with respect to electron exchanges within each monomer but not between the monomers. Therefore, the Pauli's exclusion principle is not being enforced here. So, to recover the exchange component of the intermolecular interaction energy, a suitable symmetry adaptation needs to be performed on the wavefunction $\Psi^{(0)}$.

The calculation of intermolecular interaction energy without any permutational symmetry adaptation is the standard Rayleigh Schrödinger perturbation expansion so known as the polarization approximation. The first-order and second-order energy corrections in the polarization approximation is given by the following standard RS perturbation theory formulas:

$$E_{RS}^{(1)} = \langle \Psi_A^{(0)} \Psi_B^{(0)} | V | \Psi_A^{(0)} \Psi_B^{(0)} \rangle$$

Eq. 5.20

$$\begin{aligned} E_{RS}^{(2)} = & \sum_{i \neq 0} \frac{\langle \Psi_A^{(0)} \Psi_B^{(0)} | V | \Psi_A^{(i)} \Psi_B^{(0)} \rangle}{E_A^{(0)} - E_A^{(i)}} + \sum_{j \neq 0} \frac{\langle \Psi_A^{(0)} \Psi_B^{(0)} | V | \Psi_A^{(0)} \Psi_B^{(j)} \rangle}{E_B^{(0)} - E_B^{(j)}} \\ & + \sum_{i,j \neq 0} \frac{\langle \Psi_A^{(0)} \Psi_B^{(0)} | V | \Psi_A^{(i)} \Psi_B^{(j)} \rangle}{E_A^{(0)} - E_A^{(i)} + E_B^{(0)} - E_B^{(j)}} \end{aligned}$$

Eq. 5.21

Notation: In the expression of the second-order energy correction $E_{RS}^{(1)}, \{E_A^{(i)}, \Psi_A^{(i)}\}$ and $\{\Psi_B^{(j)}, E_B^{(j)}\}, i, j = 1, 2, \dots$ are the excited eigenfunctions and eigenvalues of the Hamiltonians H_A and H_B respectively.

The charge-density due the nuclei (positive) and electrons (negative) of the monomer A (ρ_A) is expressed as:

$$\rho_A^{(0)} = \sum_{\alpha \in A} Z_\alpha \delta(r_1 - R_\alpha) - N_A \sum_{\sigma_1} \langle \Psi_A^{(0)} | \Psi_A^{(0)} \rangle$$

Eq. 5.22

Similarly, we have an analogous expression for the charge density of monomer B

$$\rho_B^{(0)} = \sum_{\beta \in B} Z_\beta \delta(r_2 - R_\beta) - N_B \sum_{\sigma_2} \langle \Psi_B^{(0)} | \Psi_B^{(0)} \rangle$$

Eq. 5.23

Therefore, from the multipole expansions of non-overlapping charge densities ρ_A and ρ_B , the electrostatic interaction energy (E_{elst}) can be expressed as the sum of the individual interactions between the permanent multiple moments of monomers A and B.

$$E_{RS}^{(1)} \equiv E_{elst}^{(1)} = \iint \rho_A^{(0)}(r_1) \frac{1}{|r_1 - r_2|} \rho_B^{(0)}(r_2) dr_1 dr_2$$

Eq. 5.24

The second-order perturbation formula $E_{RS}^{(2)}$ contains the summation over all the excited states of the unperturbed system, $\Psi_A^{(i)}, \Psi_B^{(j)}$, with indices i and j not equal to zero simultaneously. This second-order energy correction can be divided into three physically meaningful components, i.e. $E_{ind,B \rightarrow A}^{(2)}$, $E_{ind,A \rightarrow B}^{(2)}$ and $E_{disp}^{(2)}$.

$E_{ind,B \rightarrow A}^{(2)}$ is the part of induction energy due to the polarization of charge density of monomer A under the influence of electric field of monomer B. Likewise, $E_{ind,A \rightarrow B}^{(2)}$ is the part of induction energy due to polarization of monomer B under the influence of electric field of monomer A.

$$E_{ind,B \rightarrow A}^{(2)} = \sum_{i \neq 0} \frac{\langle \Psi_A^{(0)} \Psi_B^{(0)} | V | \Psi_A^{(i)} \Psi_B^{(0)} \rangle}{E_A^{(0)} - E_A^{(i)}}$$

Eq. 5.25

$$E_{ind,A \rightarrow B}^{(2)} = \sum_{j \neq 0} \frac{\langle \Psi_A^{(0)} \Psi_B^{(0)} | V | \Psi_A^{(0)} \Psi_B^{(j)} \rangle}{E_B^{(0)} - E_B^{(j)}}$$

Eq. 5.26

The second-order dispersion energy ($E_{disp}^{(2)}$) term is result of mutual polarization of monomers A and B due to their coupled instantaneous electric fields.

$$E_{disp}^{(2)} = \sum_{i,j \neq 0} \frac{\langle \Psi_A^{(0)} \Psi_B^{(0)} | V | \Psi_A^{(i)} \Psi_B^{(j)} \rangle}{E_A^{(0)} - E_A^{(i)} + E_B^{(0)} - E_B^{(j)}}$$

Eq. 5.27

Therefore, the overall expression of second-order energy correction $E_{RS}^{(2)}$

$$E_{RS}^{(2)} = E_{ind,B \rightarrow A}^{(2)} + E_{ind,A \rightarrow B}^{(2)} + E_{disp}^{(2)}$$

Eq. 5.28

5.2.3 Symmetrized RS Approach

As stated in the previous section, the resultant zeroth-order wavefunction from RS perturbation approach was not antisymmetric with respect to electron exchanges between the monomers and thus, violates the Pauli's exclusion principle. Therefore, so as to obtain the exchange corrections to the interaction energies, we need to enforce the permutational symmetry by using a $N_A + N_B$ electron anti-symmetrizer operator A in the energy expressions. There exists different ways of symmetry adaptation such as weak enforcement (where only energy expressions are anti-symmetrized) and strong enforcement (where even the anti-symmetrized operator A is used in expressions of wavefunctions).

In this approach, we use the weak enforcement of anti-symmetry. The expressions for the first-order and the second-order complete energy contributions from this approach (ESRS) is given by:

$$E_{SRS}^{(1)} = \frac{\langle \Psi_A^{(0)} \Psi_B^{(0)} | V A | \Psi_A^{(0)} \Psi_B^{(0)} \rangle}{\langle \Psi_A^{(0)} \Psi_B^{(0)} | A | \Psi_A^{(0)} \Psi_B^{(0)} \rangle}$$

Eq. 5.29

$$E_{SRS}^{(2)} = \frac{\langle \Psi_A^{(0)} \Psi_B^{(0)} | (V - E_{SRS}^{(1)}) | A \Psi_{RS}^{(1)} \rangle}{\langle \Psi_A^{(0)} \Psi_B^{(0)} | A | \Psi_A^{(0)} \Psi_B^{(0)} \rangle}$$

Eq. 5.30

The first-order SRS energy correction, $E_{SRS}^{(1)}$ is the sum of $E_{RS}^{(1)}$ and the first-order exchange energy $E_{exch}^{(1)}$. $E_{exch}^{(1)}$ is positive (repulsive) for all interactions between two closed-shell systems. In general, the exchange energy. $E_{exch}^{(n)}$ is calculated as the difference of $E_{SRS}^{(n)}$ and $E_{RS}^{(n)}$ for all orders n.

$$E_{exch}^{(1)} = E_{SRS}^{(1)} - E_{RS}^{(1)}$$

Eq. 5.31

$$E_{exch}^{(2)} = E_{SRS}^{(2)} - E_{RS}^{(2)}$$

Eq. 5.32

The second-order exchange energy $E_{exch}^{(2)}$ can be split up in an analogous fashion to $E_{RS}^{(2)}$ as follows:

$$E_{exch}^{(2)} = E_{exch-ind,B \rightarrow A}^{(2)} + E_{exch-ind,A \rightarrow B}^{(2)} + E_{exch-disp}^{(2)}$$

Eq. 5.33

All the three terms, i.e. $E_{exch-ind,B \rightarrow A}^{(2)}, E_{exch-ind,A \rightarrow B}^{(2)}, E_{exch-disp}^{(2)}$ are repulsive in nature and provide appropriate quenching of induction and dispersion energies(attractive in nature) in accordance with the Pauli's exclusion principle.

5.2.4 Levels of SAPT

The SAPT theory as explained in the earlier sections of this chapter is not a practically plausible approach as it requires the solutions of wavefunctions described by their full configuration interactions. Therefore, in a real system, we need to take into account only partial amount (or none) of intermolecular electron correlation effects. If F_A and F_B be the Fock matrices and W_A and W_B be the Møller-Plesset (MP) fluctuation potentials of monomers A and B respectively, then the generalized Hamiltonian H for all levels of SAPT is given by:

$$H = F_A + F_B + \xi(W_A + W_B) + \lambda V$$

Eq. 5.34

$$W_A = H_A - F_A$$

Eq. 5.35(a)

$$W_B = H_B - F_B$$

Eq. 5.35(b)

Notation: Here ξ and λ are the parameters of the perturbation expansion. The resultant terms $E_{SAPT}^{(mn)}$ has two indices m and n. The index $m = 1, 2, \dots$ denotes the order in V and the index $n = 1, 2, \dots$ denotes the order in W.

5.2.5 SAPT0

The simplest of the SAPT levels, which provides us with a reasonable approximation to intermolecular interaction energies is the SAPT0 method. In this case, the intramolecular electron correlation (viz. correlation between the fluctuations in electron-density of two interacting molecules) is completely neglected, i.e. ($n=0$).

$$E_{int}^{SAPT0} = E_{elst}^{(10)} + E_{exch}^{(10)} + E_{ind,resp}^{(20)} + E_{exch-ind,resp}^{(20)} + E_{disp}^{(20)} + E_{exch-disp}^{(20)} + \delta E_{HF}^{(2)}$$

Eq. 5.36

The first two terms of the above equation is the electrostatic interaction energy and its exchange counterpart. The next two parts of the equation is induction energy and its exchange counterpart. The subscript “resp” indicates the response of the Hartree-Fock orbitals of a monomer in the electrostatic potential of the other monomer. The calculation

of this response requires solving a set of coupled perturbed Hartree Fock (CPHF) equations.

The fifth and sixth terms of this equation are the only terms which signifies the true electronic correlation effects. The fifth term is the dispersion energy which provides us a good approximation to the van der Waals dispersion energies. The sixth term is the exchange counterpart of the dispersion energy. This term has two components, namely OS (opposite spin) and SS (same spin). These components are heavily dependent on the amount of spin-polarization occurring upon interaction of two molecules. The final term nearly accounts for the third and higher-order induction energy corrections. The term can be obtained for Hartree-Fock (HF) energy via supermolecular approach as:

$$\delta E_{HF}^{(2)} = E_{int}^{HF} - E_{elst}^{(10)} - E_{exch}^{(10)} - E_{ind,resp}^{(20)} - E_{exch-ind,resp}^{(20)}$$

Eq. 5.37

Thus, upon combining the above two equations, we get the following expression:

$$E_{int}^{SAPT0} = E_{int}^{HF} + E_{disp}^{(20)} + E_{exch-disp}^{(20)}$$

Eq. 5.38

5.2.6 Other SAPT Levels

To improve the accuracy of energy components over SAPT0 results, we need to take into account both higher order terms in V as well as in the fluctuation potential W. However, on proceeding towards the higher SAPT levels, the improvement of accuracy is also accompanied by computationally expensive calculations, making them require higher CPU time/resources compared to SAPT0. The thorough examination of the energy terms appearing in higher-level SAPT expressions is beyond the scope of this thesis.

Chapter 6

6. Non-Equilibrium Green's function and Inelastic Electron Tunneling Spectroscopy

With the rise in nano-technology it becomes evident that a complete quantum mechanical description of transport is important. A typical system that is important is a two-probe device with a central nano-scale object and two charged reservoirs.

6.1 Non-Equilibrium Green's function (NEGF)

This device as shown in Figure 6.1 can be seen from different perspectives, from a thermodynamical viewpoint this device has two bulk leads and one central region. The central region, called extended molecule, includes the actual device and part of the leads. The two leads are kept at two different chemical potentials and can exchange the electrons from the extended molecule. When the chemical potentials of the leads are equal, the leads are in equilibrium with each other and no current flows. When the chemical potentials are different after applying the bias, the current flows. The bias applied keeps the chemical potential of the leads different and to counter this effect the charge flows from one reservoir to other.

The approach of Non-Equilibrium Green's function [81] starts from the time-independent Schrodinger equation $[H]\{\Psi\} = E\{\Psi\}$, where H is the Hamiltonian and E is the energy eigen-value, and adding 2 terms that represent inflow and outflow [82].

$$[H]\{\Psi\} + [\Sigma]\{\Psi\} + \{s\} = E\{\Psi\}$$

Eq. 6.1

The second term on LHS represents outflow and third term represents inflow. These two terms arise after imposing open boundary conditions on the Schrodinger equation with an incident wave from the contacts. Using this equation, the wave function can be written as

$$\{\Psi\} = [EI - H - \Sigma]^{-1} \{s\}$$

Eq. 6.2

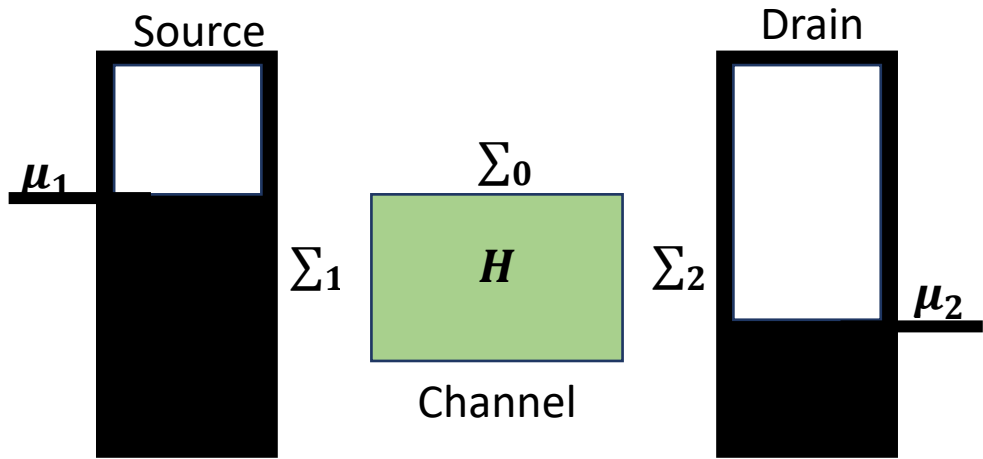


Figure 6.1: In the NEGF-based quantum transport model, Hamiltonian matrix $[H]$ describes the channel, the self-energy matrices $[\Sigma]$ and the connection between the channel and contacts, and $[\Sigma_0]$ describes interactions inside the channel.

It is convenient to work with quantities like

$$[G^n] \sim \{\Psi\}\{\Psi\}^\dagger$$

Eq.6.3(a)

$$[\Sigma^{in}] \sim \{s\}\{s\}^\dagger$$

Eq. 6.3(b)

By defining

$$[G^R] = [EI - H - \Sigma]^{-1}$$

Eq. 6.4

$$[G^A] = [G^R]^\dagger$$

$$G^n = G^R \Sigma^{in} G^A$$

Eq. 6.5

The standard notation for G^n and Σ^{in} is

$$G^n \rightarrow -iG^< \text{ and } \Sigma^{in} \rightarrow -i\Sigma^<$$

Working with this formalism has two important aspects:

(a) equations 6.4 and 6.5

(b) finding Σ (self-energy) and Σ^{in} (in-scattering)

The two equations define retarded Green's function and the matrix version of electron density respectively and essentially have the essence of NEGF formalism but it is the evaluation of self-energy and in-scattering that evolves with the problem being looked at. The NEGF method provides a rigorous way to include all types of interaction in the channel, both elastic and inelastic.

The matrix version of density of states, called spectral function, is defined by

$$A = i[G^R - G^A]$$

Eq. 6.6

The anti-Hermitian part of self-energy is called the broadening matrix and describes the ease of electrons in the channel communicating with the contacts.

$$\Gamma = i[\Sigma - \Sigma^\dagger]$$

Eq. 6.7

The current at any contact can be written as

$$I_i = \frac{q}{h} \text{Trace} [\sum_i^{in} A - \Gamma_i G^n]$$

Eq. 6.8

where I_i is the current operator and gives the current depending upon the problem in hand.

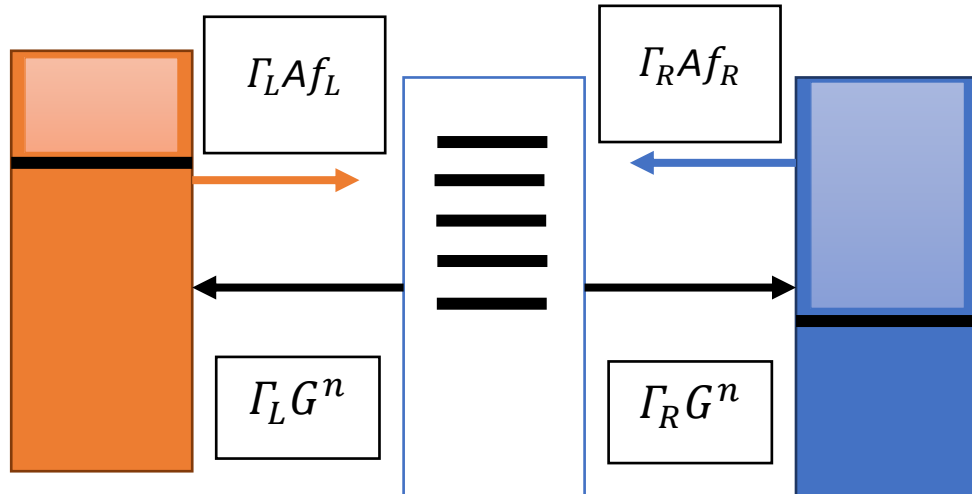


Figure 6.2: Quantum treatment of filling and emptying a channel in a device with a channel and two reservoirs.

6.1.1 Coherent and Incoherent Transport

The coherent transport

$$\tilde{I}(E) = \frac{q}{h} \text{Trace}[\Gamma_L G^r \Gamma_R G^a] (f_L(E) - f_R(E))$$

Eq.6.9

The quantum expression for the conductance $G(E)$ for the coherent transport is

$$G(E) = \frac{q^2}{h} \text{Trace}[\Gamma_L G^r \Gamma_R G^a]$$

Eq.6.10

In the NEGF formalism the elastic and inelastic effects can be included into the self-energy

$$G^{r,a} = \frac{1}{E - H - \Sigma^{r,a}}$$

Eq. 6.11(a)

$$\Sigma = \Sigma_L + \Sigma_R + \Sigma_{int}$$

Eq. 6.11(b)

6.2 Inelastic Electron Tunnelling Spectroscopy

The inelastic electron tunnelling spectroscopy is used to measure the vibrational frequencies of molecules. The system consists of two metal electrodes connected by a molecule, a metal-insulator-metal junction, shown in Figure 6.3. When a voltage V is applied across this junction, the electron tunnels from the left to the right electrode elastically and to a first approximation the current-voltage relationship is linear. At a particular voltage V_0 , an inelastic channel opens up and the conductance increases. At this voltage $eV_0 = \hbar\omega_0$, the electron excites a vibrational mode of the molecule. This increase in conductance appears as a kink in the I-V characteristics, a step in the first derivative plot, and a peak in the second derivative plot sha shown in Figure 6.4.

The inelastic tunnelling takes place when the electron couples with the phonon or vibrational mode and excites the local vibrational mode [26]. The tunneling rate is given by:

$$W_{L \rightarrow R} = \frac{2\pi}{\hbar} |M_{LR}|^2 \delta(E_L - E_R - \hbar\omega_0)$$

Eq. 6.12

M_{LR} is the tunneling matrix element, this tunneling rate gives the transition rate from the left to the right electrode when the difference between the electron energy in the left and right electrodes is equal to the energy of the localized vibrational mode (vibron) of the molecule.

When this inelastic transition occurs due to the vibron a peak occurs at that voltage in the $\frac{d^2I}{dV^2}$ vs V plot. The frequencies of the molecule at which these transitions occur can act as their chemical signatures. The IET spectroscopy is useful in experimental nano-scale physics, also used to explain the signal transduction in the context of vibrational theory of olfaction. To understand the theory of IETS from NEGF formalism is important for making VTO based artificial nose nano-sensors.

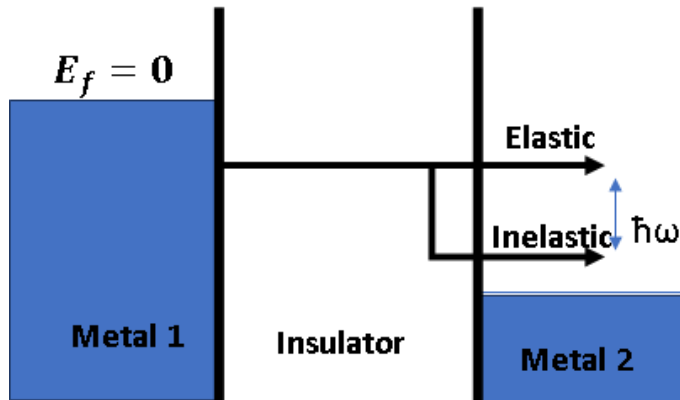


Figure 6.3: Schematic illustration of phonon-assisted tunneling in the two-probe molecular junction system. An electron incoming from the left lead emits a phonon (quantized molecular vibrational mode) in the molecular junction and propagates to the right lead with lower energy.

6.2.1 Electron-Phonon coupling

Hamiltonian of an electron-ion system,

$$H = \sum_K \frac{p_K^2}{2M_K} + \sum_{K,L} V_{ion-ion}(R_K, R_L) + H_{el} + H_{el-ion}$$

Eq. 6.13

Here the first two terms correspond to the ionic degrees of freedom (the first term is kinetic energy) the third and fourth terms are the electronic Hamiltonian and electronic-ion interaction term. The total energy of the system for a given ionic configuration may be expressed as:

$$E_{total}[\{R_K\}, \psi_e] = \langle \psi_e | H_{el} + H_{el-ion} + V_{ion-ion}(\{R_K\}) | \psi_e \rangle$$

Eq. 6.14

The solution to the Schrödinger Equation with the first two terms may be obtained through the Kohn-Sham equation in Density Functional Theory.

$$H_e = H_{el} + H_{el-ion}$$

Eq. 6.15

Now, at each point on the energy surface for an ionic configuration, the ions have a potential energy E_{total} , which is a function of ionic positions.

For the vibrational degrees-of-freedom, the Hamiltonian can therefore be written as:

$$H_{ph} = \sum_K \frac{p_K^2}{2M_K} + E_{total}[\{R_K\}]$$

Eq. 6.16

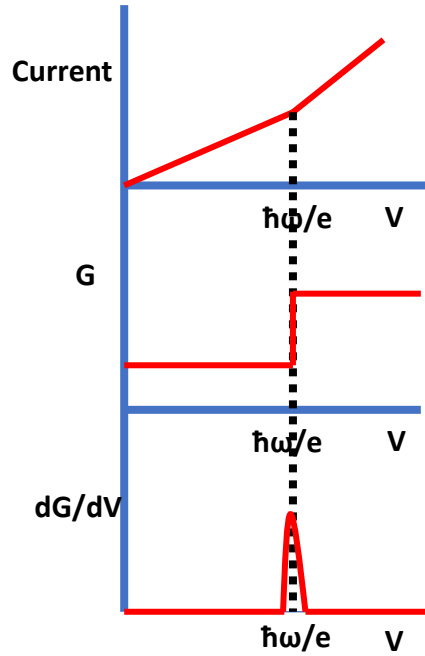


Figure 6.4: Schematic I-V, G-V, and IETS-V curves are shown with the existence of electron-phonon coupling. A delta-function peak in the dG/dV curve results from the conductance suddenly increasing as the phonon-assisted transport process becomes viable (the step-function increase only occurs at zero-temperature conditions and will be smoothed out at finite temperature).

Here the first terms on the right-hand side corresponds to the ionic kinetic energy as a quadratic function of their momenta, and the second to the potential energy as a function of their positions. Expanding the second term in a Taylor series around the equilibrium position:

$$\begin{aligned}
H_{ph} = & \sum_K \frac{p_K^2}{2M_K} + E_{total}[\{R_{K0}\}] + \sum_K \frac{\partial E_{total}}{\partial R_K} |_{\{R_{K0}\}} (R_K - R_{K0}) \\
& + \sum_{K,L} \frac{\partial^2 E_{total}}{\partial R_K \partial R_L} |_{\{R_{K0}\} \{R_{L0}\}} (R_K - R_{K0})(R_L - R_{L0})
\end{aligned}$$

Eq. 6.17

The first derivative of the energy will be zero in the equilibrium state. Recognizing that the second derivative is nothing but the spring constant, the Dynamical Matrix can be written as:

$$D_{KL} = \frac{1}{\sqrt{M_K M_L}} \frac{\partial^2 E_{total}}{\partial R_K \partial R_L}$$

Eq. 6.18

Following second quantization procedure, the transformation is as

$$\sqrt{M_K} \delta R_{K\alpha} \rightarrow \sum_\nu \sqrt{\frac{\hbar}{2\omega_\nu}} e_{K\alpha}^\nu (b_\nu^\dagger + b_\nu)$$

Eq. 6.19(a)

$$\frac{\hat{p}_{K\alpha}}{\sqrt{M_K}} \rightarrow i \sum_\nu \sqrt{\frac{\hbar\omega_\nu}{2}} e_{K\alpha}^\nu (b_\nu^\dagger - b_\nu)$$

Eq. 6.19(b)

Equation 6.17 becomes

$$H_{ph} = \sum_\nu \hbar\omega_\nu (b_\nu^\dagger b_\nu + \frac{1}{2})$$

Eq. 6.20

The electron-phonon coupling term can be obtained by expanding electronic Hamiltonian

$$\hat{H}_e[\{R_K\}] = \hat{H}_e[\{R_K^0\}] + \sum_K \frac{\partial \hat{H}_e}{\partial R_K} (R_K - R_K^0) + O(\delta R^2)$$

Eq. 6.21

$$\hat{H}_e[\{R_K\}] = \hat{H}_e[\{R_K^0\}] + \sum_{K\alpha,\nu} \sqrt{\frac{\hbar}{2M_K\omega_\nu}} \frac{\partial \hat{H}_e}{\partial R_{K\alpha}} e_{K\alpha}^\nu (b_\nu^\dagger + b_\nu)$$

$$\hat{H}_e[\{R_K\}] = \hat{H}_e[\{R_K^0\}] + \sum_\nu \hat{g}_\nu (b_\nu^\dagger + b_\nu)$$

Eq. 6.22

The electron-phonon coupling factor

$$\hat{g}_\nu = \sum_{K\alpha} \sqrt{\frac{\hbar}{2M_K\omega_\nu}} \frac{\partial \hat{H}_e}{\partial R_{K\alpha}} e_{K\alpha}^\nu$$

Eq. 6.23

The electron-phonon coupling introduces complexities to the NEGF formalism, discussed in the previous section. The effect of phonon to electrons can be understood in terms of self-energies. To solve these complexities introduced in the equations, some simplifications are needed. First, the phonons are assumed to be at zero-temperature equilibrium. The electronic device is coupled to a bath of phonons which is at zero temperature. Any phonon excited by an electron immediately gets absorbed in the bath and so there is no accumulation of phonons in the device.

Second, the lowest order contribution is considered due to electron-phonon coupling in the self-energy. In including only the lowest order term, the self-energy is calculated from non-

perturbative electron Green's function and the full Green's function is obtained from Dyson equation,

$$G = G_0 + G_0 \Sigma G$$

Eq. 6.24

Beyond the first order Born Approximation is the self-consistent Born approximation (SCBA), in which the self-consistent full Green's function is used in the calculation of self-energy [83].

The bare phonon's Green function can be

$$D_\nu^r(\Omega) = \frac{1}{\Omega - \hbar\omega_\nu + i\epsilon} - \frac{1}{\Omega + \hbar\omega_\nu + i\epsilon}$$

Eq. 6.25

$$D_\nu^a(\Omega) = \frac{1}{\Omega - \hbar\omega_\nu - i\epsilon} - \frac{1}{\Omega + \hbar\omega_\nu - i\epsilon}$$

Eq. 6.26

$$D_\nu^<(\Omega) = -2\pi i[n_\nu \delta(\Omega - \hbar\omega_\nu) + (n_\nu + 1)\delta(\Omega + \hbar\omega_\nu)]$$

Eq. 6.27

$$D_\nu^>(\Omega) = -2\pi i[(n_\nu + 1)\delta(\Omega - \hbar\omega_\nu) + n_\nu\delta(\Omega + \hbar\omega_\nu)]$$

Eq. 6.28

$$\text{where } n_\nu = \frac{1}{e^{\frac{\hbar\omega_\nu}{kT}} - 1}$$

Eq. 6.29

is the Bose-Einstein distribution function. The phonons are at equilibrium and so they do not affect the electron density. The electron self-energy due to phonon will be

$$\Sigma_{e-ph}(E) = i \sum_\nu \int \frac{d\Omega}{2\pi} g^\nu G(E - \Omega) g^{\nu\dagger} D(\Omega)$$

Eq. 6.30

The lesser, greater, retarded, advanced self-energies will be

$$\Sigma_{e-ph}^<(E) = \sum_\nu n_\nu g^\nu G^<(E - \hbar\omega_\nu) g^{\nu\dagger} + (n_\nu + 1) g^\nu G^<(E + \hbar\omega_\nu) g^{\nu\dagger}$$

Eq. 6.31

$$\Sigma_{e-ph}^>(E) = \sum_\nu (n_\nu + 1) g^\nu G^>(E - \hbar\omega_\nu) g^{\nu\dagger} + n_\nu g^\nu G^>(E + \hbar\omega_\nu) g^{\nu\dagger}$$

Eq. 6.32

$$\begin{aligned} \Sigma_{e-ph}^r(E) &= \sum_\nu (n_\nu + 1) g^\nu G^r(E - \hbar\omega_\nu) g^{\nu\dagger} + n_\nu g^\nu G^r(E + \hbar\omega_\nu) g^{\nu\dagger} \\ &\quad + i \sum_\nu \int \frac{d\Omega}{2\pi} g^\nu G^<(E - \Omega) g^{\nu\dagger} \left[\frac{1}{\Omega - \hbar\omega_\nu + i\epsilon} - \frac{1}{\Omega + \hbar\omega_\nu + i\epsilon} \right] \end{aligned}$$

Eq. 6.33

$$\begin{aligned}\Sigma_{e-ph}^a(E) = & \sum_\nu (n_\nu + 1) g^\nu G^a(E - \hbar\omega_\nu) g^{\nu\dagger} + n_\nu g^\nu G^a(E + \hbar\omega_\nu) g^{\nu\dagger} \\ & - i \sum_\nu \int \frac{d\Omega}{2\pi} g^\nu G^<(E - \Omega) g^{\nu\dagger} \left[\frac{1}{\Omega - \hbar\omega_\nu - i\epsilon} - \frac{1}{\Omega + \hbar\omega_\nu - i\epsilon} \right]\end{aligned}$$

Eq. 6.34

6.2.2 Transmission with phonon under SCBA

In the two-probe, non-equilibrium system, the total self-energies include those from the leads as well as from the electron-phonon coupling [83]

$$\Sigma^\gamma = \Sigma_L^\gamma + \Sigma_R^\gamma + \Sigma_{e-ph}^\gamma$$

Eq. 6.35

where $\gamma = r, a, <, >$

$$G^{r,a} = \frac{1}{E - H - \Sigma^{r,a}}$$

Eq. 6.36(a)

$$G^{>,<} = G^r (\Sigma_L^{>,<} + \Sigma_R^{>,<} + \Sigma_{e-ph}^{>,<}) G^a$$

Eq. 6.36(b)

where the self-energies due to phonons are functionals of the full electron Green's functions.

In the self-consistent Born approximation, as shown in Figure 6.5, the self-energy due to electron-phonon coupling and the full electron Green's function are calculated self-consistently. Within each self-consistent cycle between electron density ρ and the Hamiltonian H , another self-consistent cycle between the Green's function and the phonon

self-energy is inserted. The Green's function calculated after one ρ -H-G cycle is used for calculating the electron self-energy due to the phonons for the next cycle. Once the self-consistency is reached, the two sets of self-consistent equations are automatically satisfied [83].

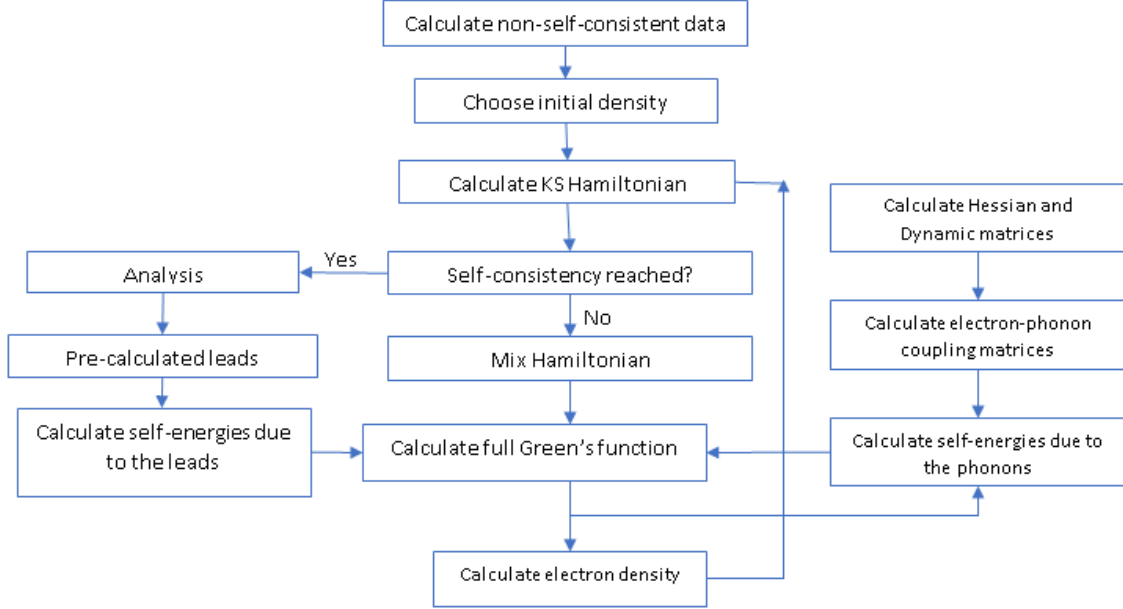


Figure 6.5: Flow chart for DFT-NEGF-SCBA self-consistent cycle. Electron self-energies due to the phonons are calculated from the electron Green's functions from the previous self-consistent cycle.

The current expression is given by:

$$I_L = \frac{2e}{h} \int dE \operatorname{Tr}(\sum_L^< G^> - \sum_L^> G^<)$$

Eq. 6.37(a)

$$I_R = \frac{2e}{h} \int dE \operatorname{Tr}(\sum_R^< G^> - \sum_R^> G^<)$$

Eq. 6.37(b)

where the lesser or greater Green's function is given by

$$G^{>,<} = G^r (\Sigma_L^{>,<} + \Sigma_R^{>,<} + \Sigma_{e-ph}^{>,<}) G^a$$

in the presence of electron-phonon coupling. The self-energy due to the electrodes under fluctuation-dissipation theorem,

$$\Sigma_{L,R}^> = i f_{L,R}(E) \Gamma_{L,R}(E)$$

Eq. 6.38(a)

$$\Sigma_{L,R}^< = i(f_{L,R}(E)-1) \Gamma_{L,R}(E)$$

Eq. 6.38(b)

and self-energy due to phonon is

$$\Sigma_{e-ph}^{>,<}(E) = \sum_{\nu} g^{\nu} G^{<,>}(E \pm \hbar\omega_{\nu}) g^{\nu\dagger}$$

Eq. 6.39

$$I_L = \frac{2e}{h} \int dE \text{Tr} [\Sigma_L^< G^r (\Sigma_L^> + \Sigma_R^> + \Sigma_{e-ph}^>) G^a - \Sigma_L^> G^r (\Sigma_L^< + \Sigma_R^< + \Sigma_{e-ph}^<) G^a]$$

Eq. 6.40

The elastic and inelastic part of the transmission is:

$$I_L^{el} = \frac{2e}{h} \int dE (f_L(E) - f_R(E)) \text{Tr} (\Gamma_L(E) G^r \Gamma_R(E) G^a)$$

Eq. 6.41(a)

$$I_L^{inel} = \frac{2e}{h} \int dE \operatorname{Tr} [\Sigma_L^< G^r \Sigma_{e-ph}^> G^a - \Sigma_L^> G^r \Sigma_{e-ph}^< G^a]$$

Eq. 6.41(b)

The sum of the elastic and inelastic current will give the total current whether calculated from left to right or from right to left [83].

In this work the electron-phonon coupling is not the coupling between electron and the bulk phonon mode present in the device but, here this coupling is between the electron in the channel and the localized vibrational mode, called vibron [60]. IETS is used to detect vibrational modes of organic molecules by the electrons present in the channel interacting with the before mentioned vibrational modes. These vibrational modes are localized because of local presence of organic molecule in the channel. This interaction too opens up an inelastic channel which can manifest itself as a distinct peak in the double derivative of the current with respect to voltage.

Chapter 7

7. Enantioselective Olfaction within the Vibration

Theory

The nascent field of Quantum Biology explores non-trivial quantum mechanical effects in biological systems. Besides the scientific appeal, it presents a technological opportunity to explore quantum biomimetic devices inspired by these systems. The olfactory system is a prototypical quantum biological system, based on the theory that odorants are sensed by their vibrational energies through a quantum mechanical mechanism, viz. inelastic electron tunneling (IET) [4].

As discussed in detail in chapter 2, the orthodox understanding of Olfaction is based on a Docking (Lock and Key) mechanism where the odorant molecule (key) binds to one or more olfactory receptors (lock). This is thought to lead to a conformational change that results in a signal to the brain, which translates into the perception of odor. Thus, in this picture, the structure of an odorant molecule decides its smell. An heterodox thesis is the Vibration Theory of Olfaction (VTO), which claims that the olfactory receptors act as chemical spectrometers, to identify odorant molecules through their vibrational modes. While this basic idea has been around for a long time [2], it gained a fresh lease of life when an existing analytical technique called IET Spectroscopy (IETS) [17] was propounded as the mechanism for this vibration sensing [4]. The idea is that IET through a receptor would bear a signature of the vibrational mode/s introduced by an adsorbed odorant molecule, to which the tunneling electrons can lose energy. VTO seems to be well-suited to address some questions that the

Lock and Key picture cannot readily answer, such as the experimentally observed difference in smell between some identically shaped molecules, and the similarity in smell between some differently shaped molecules with similar vibrational energies.

However, VTO is not without gaps of its own. In fact, we tried to elucidate the connection between the structure and vibrational modes of odorant molecules, in the previous section [84], and suggest that these two pictures are related - while neither might be complete in itself. An essential gap in VTO is its inability to explain the difference in smell between enantiomers (left-handed vs. right-handed versions of the same molecule) [85], which have identical vibrational spectra.

Now, chirality in molecules has traditionally been probed using circularly polarized light because of its obvious enantioselectivity [86]. As discussed in Chapter 6, it has been recognized that charge polarization in chiral molecules would be accompanied by spin polarization because of spin-orbit coupling. This phenomenon has been termed Chirality Induced Spin Selectivity (CISS), and it has opened up spin-polarized electrons as another tool to probe chiral molecules [87]. Can we combine CISS together with IETS to investigate the possible enantioselectivity of olfaction within VTO?

7.1 Molecular Interaction and Spin Polarization

The symmetry constraint imposed by the spin polarization affects the electron cloud overlap, the electron exchange and correlation significantly contribute to the intermolecular forces at short range. The exchange interaction resulting from the quantum nature of the electron can stabilize the energy of the electrons that are confined in a region of space if they have opposite spins. Electrostatics and quantum mechanics mainly differ on the inclusion of electron spin, the inclusion of spin in charge polarization for the interaction between chiral molecules can describe the difference in the strength of the interaction between chiral molecules [87].

Interactions between two molecules or between non-bonded atoms can be attractive or repulsive, and it exists from protein folding, drug designing to nanotechnology. They do not form bonds and so it is called non-covalent interactions. The interaction can be electrostatic,

induced, dispersion or exchange discussed in depth in chapter 5). At long distances, these interactions are predominantly attractive, but at short ranges, they can be more complicated due to wavefunction overlap. The amount of repulsion depends upon the spin of the overlapping electrons. The same spin interaction forms an asymmetric wavefunction and destabilizes the interaction and repulsion increases whereas opposite spins form symmetric wavefunction stabilizing the interaction by reducing the repulsion.

Non-covalent interaction in molecular systems is calculated using force fields that are generated using a combination of quantum chemistry and model-fitting. Spin effects are not included in these effects. The interaction of molecules is accompanied by the polarization of charge which should be accompanied by some amount of spin polarization, via the CISS effect. If this affects the intermolecular interaction between the molecular systems this can lead to enantioselectivity intrinsic to the molecular system (due to the chirality of the system). It has been established through various studies that when two molecules of same-handedness interact the charge polarization is accompanied by spin polarization analogous to the singlet state whereas when the molecules of different chirality interact, the spin polarization created is analogous to the triplet state, illustrated in Figure 7.1. The interaction between molecules becomes enantiospecific due to the inclusion of spin in the interaction [87].

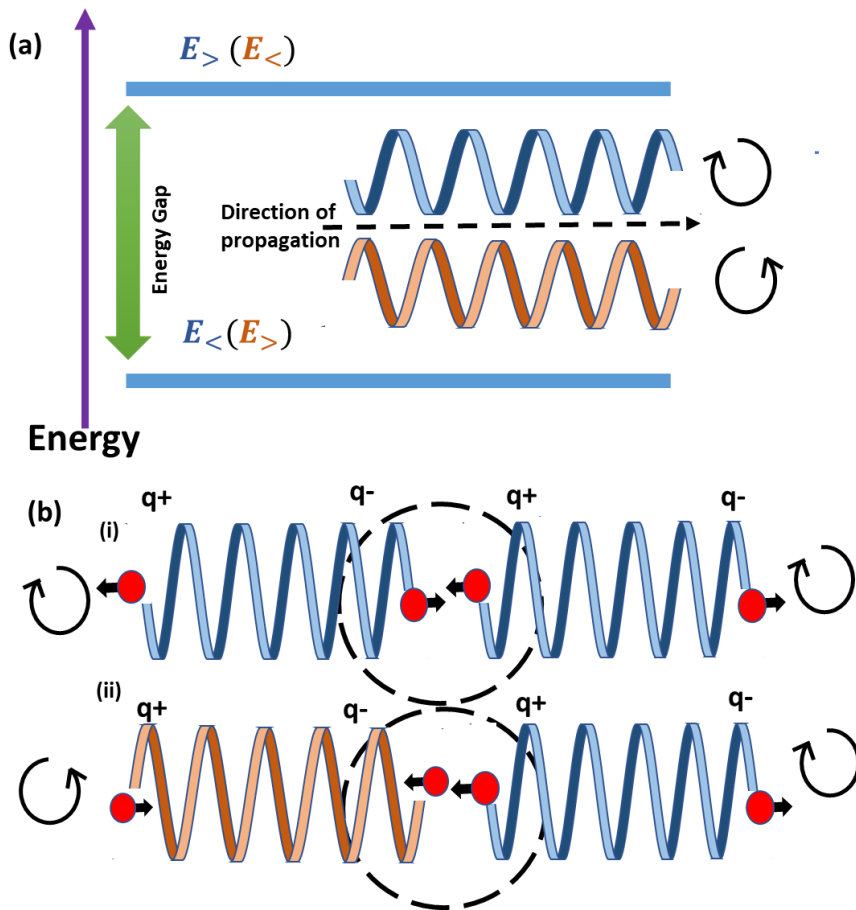


Figure 7.1: (a) The splitting of energy of up-spin and down spin electrons due to chirality of the channel vis a vis the direction of propagation. (b) (i) The illustration shows how two molecules with the same handedness interact via generated dipoles. The same spin is polarised in both molecules as charge q moves from one side to the other of the molecule, as shown by the red ball and black arrow. Due to the opposite spin polarization of the electron density that was left behind, the interaction between the molecules is therefore defined by two opposite spins, as seen by the singlet region in the dotted circle. (ii) When two molecules are interacting and have opposing chiralities, their interaction is characterized by two spins that are parallel to one another (in the dotted circle triplet region) [87].

To demonstrate this, the interaction energy of the two enantiomeric pairs was calculated where charge polarization is accompanied by spin polarization. For chiral molecules, these calculations were done using Symmetric Adapted Perturbation Theory, using the package Psi4 (see end of chapter for detail) [89]. Plot for interaction energies was obtained justifying the change between symmetric and anti-symmetric wavefunctions [83].

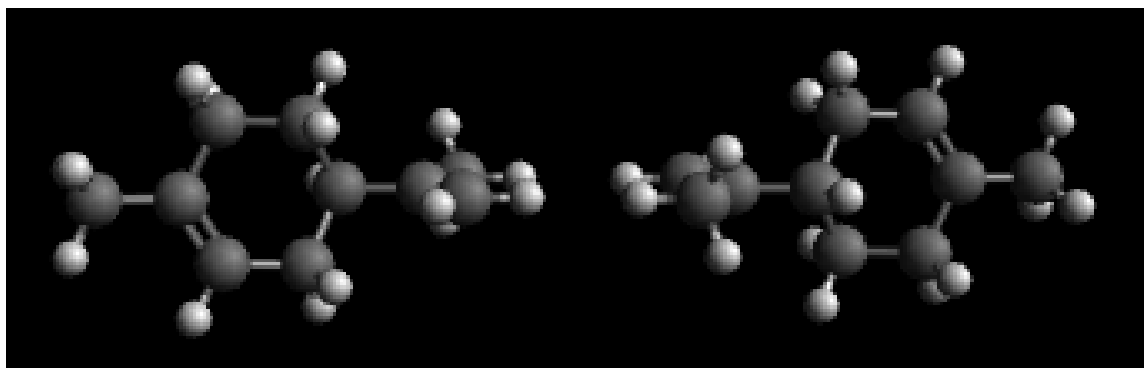


Figure 7.2: The two enantiomers of Limonene molecule are R-(+)-Limonene and (S)-(-)-Limonene. R-(+)-Limonene: This is found naturally in rind of oranges and has a pleasant, orange-like odor. S-(-)-Limonene: This is found in lemon peels and has a harsh turpentine-like odor with lemon note. [89]

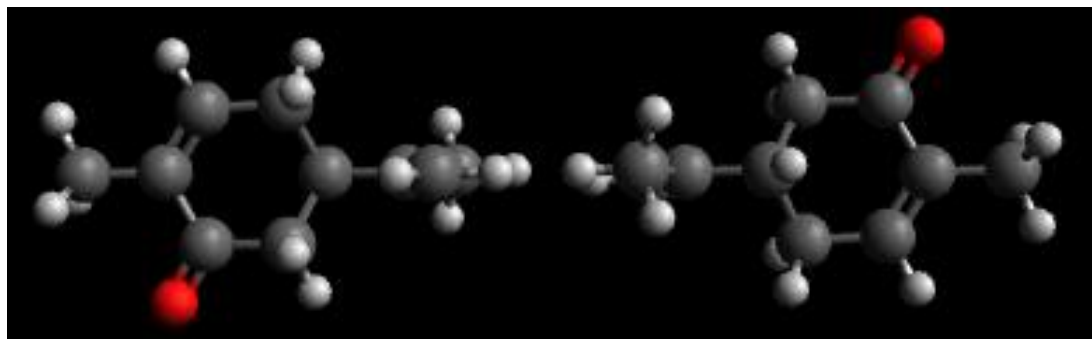


Figure 7.3: Carvone: The two enantiomers of Carvone molecule are (R)-(-)-Carvone and (S)-(+)-Carvone. (R)-(-)-Carvone: It is extracted from spearmint leaves and smells like spearmint. (S)-(+)-Carvone: It is extracted from caraway seeds and smells like caraway. [90]

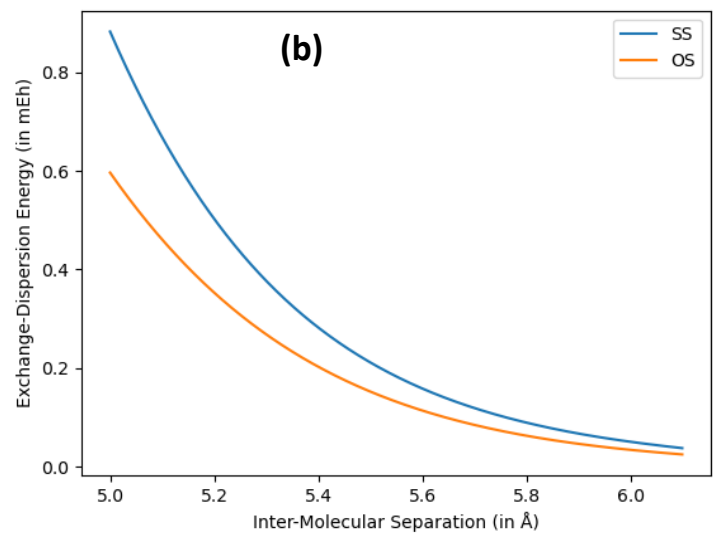
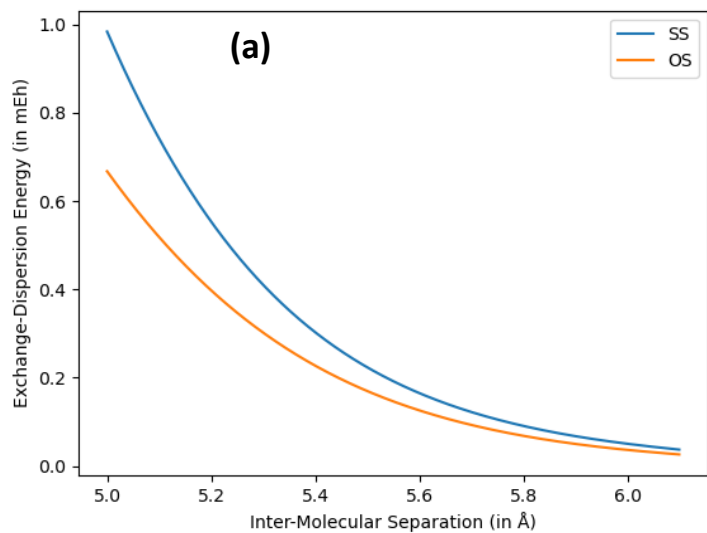


Figure 7.4: The plots of the values of exchange-dispersion energy for (a) limonene (obtained from SAPT0 simulation) and (b) carvone, as the function of intermolecular distance. The blue curve in these plots show similar spin interaction (SS component of exchange-dispersion energy), which is equivalent to the interaction between enantiomers of opposite handedness. Meanwhile, the orange curve indicates the opposite spin interaction (OS component of exchange-dispersion energy), which is equivalent to the interaction between enantiomers of same handedness.

The study of interactions between pairs of enantiomers having different odor was conducted to analyze the enantioselective nature of interactions between them. The two sets of enantiomers were chosen and aligned carefully. After that, SAPT0 simulations were performed upon them to get the individual components of their interaction energy. The two sets of enantiomers are Limonene (R,S) and Carvone (R,S) as shown in Figure 7.1 and 7.2.

The plots of exchange-dispersion energies of the interaction between the enantiomer pairs (Figure 7.3) has two curves, namely blue and orange curves. The blue curve in these plots show similar spin interaction (SS component of exchange-dispersion energy), which is equivalent to the interaction between enantiomers of opposite handedness. Meanwhile, the orange curve indicates the opposite spin interaction (OS component of exchange-dispersion energy), which is equivalent to the interaction between enantiomers of same handedness. As observed from the plots, the interaction energy for the case in which the two molecules have opposite handedness (RS), is more repulsive than when the two molecules have same handedness (SS). This is similar to results reported in the literature. [87]

7.2 Combining Spin selectivity and IETS

Theoretically it can be shown that, with the inclusion of CISS for a chiral olfactory receptor, the IETS signal emanating from it could indeed be enantioselective. In other words, the IET spectra (and ergo, the sensed smell) could differ for the left-handed versus the right-handed versions of an adsorbed odorant molecule, depending on the chirality of the receptor. Thus, we show that it is possible to have enantioselective olfaction within the Vibration Theory. As

it is to imagine IETS-based electronic nose sensors (i.e. artificial olfactory receptors) that are also enantioselective.

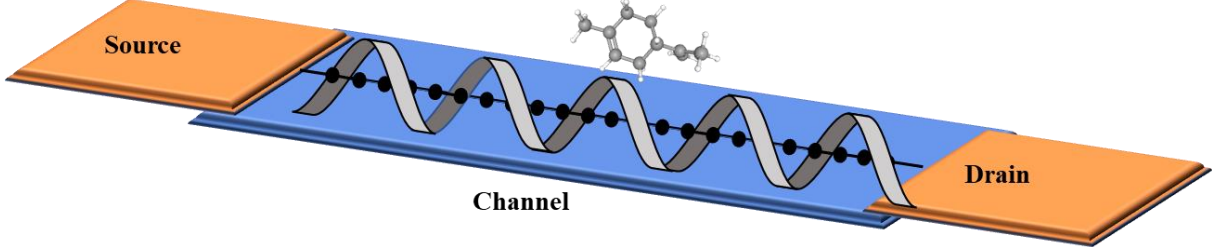


Figure 7.5: Simulation set-up with source, drain and channel. The channel is chiral and the odorant molecule is also chiral.

The simulation setup, Figure 7.5, consists of a source, drain and a channel. The channel is chiral and so will support one type of spin (either up or down). If a chiral molecule will come and interact with the receptor (channel) and opens up an inelastic channel as in IETS. As discussed above, the Vibration Theory of Olfaction (VTO) in its modern form is based on Inelastic Electron Tunneling Spectroscopy (IETS). As discussed in detail in Chapter 5, in IETS an extra inelastic channel opens up when electron interacts with the vibron. In an IETS based sensor, the vibrational mode of a foreign molecule opens up an inelastic channel for quantum mechanical tunneling, in addition to the usual elastic channel.

7.2.1 Result and Analysis

Spin selectivity is an exciting prospect for technological applications and several recent developments, both experimental and theoretical, have shown that the CISS effect has a significant amount of spin-selectivity. [87]

Although the impact of CISS on chiral systems is well understood, there is currently no experimental evidence to support this in the biorecognition processes. The chirality of molecules can be probed only in a chiral environment, the optically polarized light distinguishes between enantiomers. In this model, we assume that the channel is chiral because the protein that makes receptors are chiral in nature. In the vibration theory of olfaction, the phenomenon for signal transduction is assumed to be inelastic electron

tunneling. The electron-phonon coupling is the most important parameter that measures the change in force provided by the phonon mode for electrons to move from one site to another. It is usually calculated from expanding the Hamiltonian around equilibrium molecular configuration. The electronic Hamiltonian is modified here by including the short-range repulsions due to the exchange and overlap of electrons.

The electron-phonon coupling constant is,

$$\hat{g}_v = \sum_{K\alpha} \sqrt{\frac{\hbar}{2M_K \omega_v}} \frac{\partial \hat{H}_e}{\partial R_{K\alpha}} e_{K\alpha}^v$$

Eq. 7.1

where M_K is the nuclear mass, v is the index on vibron modes, ω_v is the frequency of the vibron modes, α is the index on the direction (cartesian coordinate direction), and $e_{K\alpha}^v$ is the transformation-vector. The detailed of the derivation are shown in the previous chapter.

The electron-phonon coupling depends upon the derivative of the electron Hamiltonian which with inclusion of spin will also depend upon electron-electron interaction, it will consist of 3 parts, the electron kinetic energy, the electron-ion interaction, and an electron-electron interaction due to wavefunction overlap (spin-dependent interaction) respectively.

$$\frac{\partial H_e}{\partial R_K} = \frac{\partial H_{el}}{\partial R_K} + \frac{\partial H_{el-ion}}{\partial R_K} + \frac{\partial H_{el-el}}{\partial R_K}$$

Eq.7.2

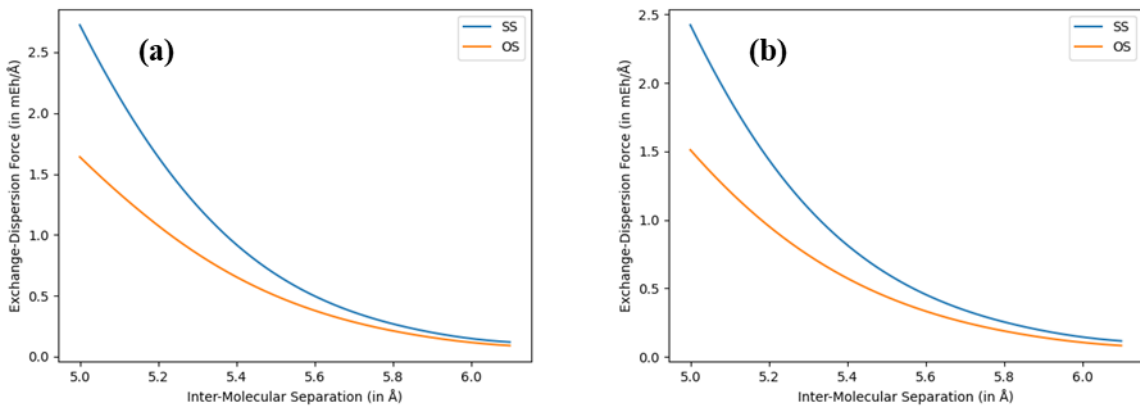


Figure 7.6: The plots of the values of derivative of exchange-dispersion energy with coordinate for (a) limonene (obtained from SAPT0 simulation) and (b) carvone as the function of intermolecular distance (absolute value). The blue curve in these plots show similar spin interaction (SS component of exchange-dispersion energy), which is equivalent to the interaction between enantiomers of opposite handedness. Meanwhile, the orange curve indicates the opposite spin interaction (OS component of exchange-dispersion energy), which is equivalent to the interaction between enantiomers of same handedness.

The electron-electron interaction shown in Figure 7.4, the derivative of this plot with respect to the coordinates, as shown in Figure 7.5, will give the change in force required and modify the electron-phonon coupling. It will form the third term of equation 7.2. The modified electron-phonon coupling is more for an opposite spin than for same spin making same handed interaction more feasible in Inelastic Electron Tunneling spectroscopy. For opposite handed interaction the derivative is more negative than for same handedness. That makes electron-phonon coupling for a system of same handedness system more than the system having opposite handedness.

The phenomenon of CISS enforces the assumption that the spins are polarized anti-parallel for the same handedness, whereas they are polarized parallel for the opposite handed case. the interaction enantioselective and so is olfaction. The inclusion of CISS in the framework of IETS can generate a signal that is enantioselective. The chirality can only be probed in a chiral environment, so the receptor in the sensor is assumed to be chiral too. The current in inelastic electron tunneling consists of two components, one elastic and the other originating from the opening of the inelastic channel. In this case, the inelastic interaction arises due to

the vibrational mode introduced by the odorant (foreign) molecule. The strength of inelastic interaction depends upon the electron-phonon coupling between the receptor and the foreign molecule. The inclusion of the spin-dependent exchange dispersion energy makes the interaction enantio-selective.

The simulation is done using NEGF formalism, explained in chapter 6 and see Supriyo Datta Chap 11 [91], to solve for the current in the simulation setup used.

The plot in Figure 7.6 is the plot of current v/s voltage for the simple single molecular chain with no foreign molecule to interact, as the simulation set-up. The introduction of an odorant molecule to interact with the molecular chain open up an inelastic channel, the strength of the interaction depends upon the magnitude of the electron-phonon coupling. The electron-phonon coupling is the parameter that measures the change of force when the electron interacts with the particular vibron-mode introduced by the odorant molecule. The inclusion of spin in the interaction creates a selective signal.

The receptor assumed in the simulation setup is very simple and basic, but IETS measurements with complex receptor structures can give useful insights into the type of interaction between odorant and receptor. In this setup, the two interacting molecules are in direct contact to make the short-range interaction become significant. This is necessary because the correlation energy of the electrons is only relevant when the electronic wavefunctions significantly overlap. The efficient enantio-recognition found in biological systems as opposed to the less effective process found in solutions or separating columns may be explained by this phenomenon. The process of including spin to make an enantioselective sensor in the framework of the vibrational theory of olfaction (VTO), so to calculate the double derivative of the current is an important step in sensing the vibrational modes.

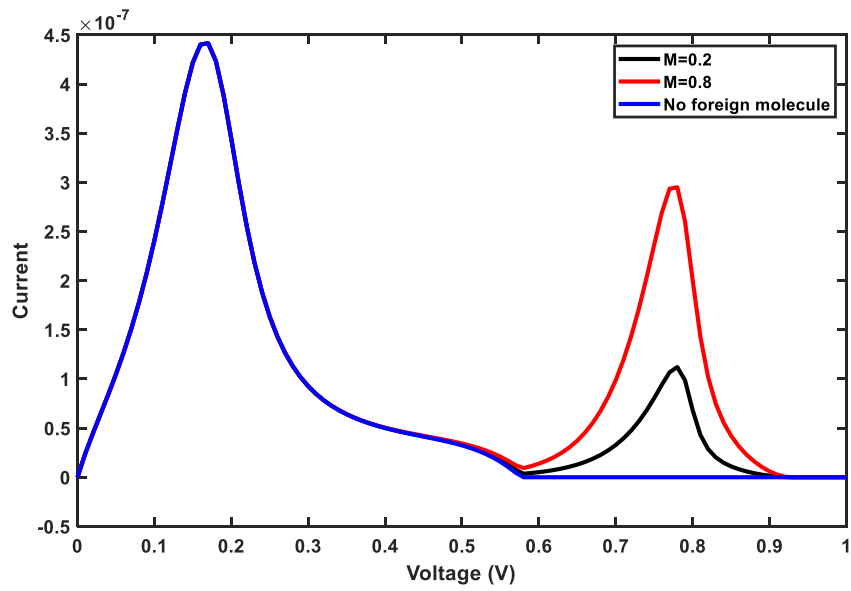


Figure 7.7: The Current vs Voltage plot showing the current through the sensor when no foreign molecule (odorant) is there, when a foreign molecule of different handedness interacts (black curve) and when a foreign molecule of same handedness interacts (red curve).

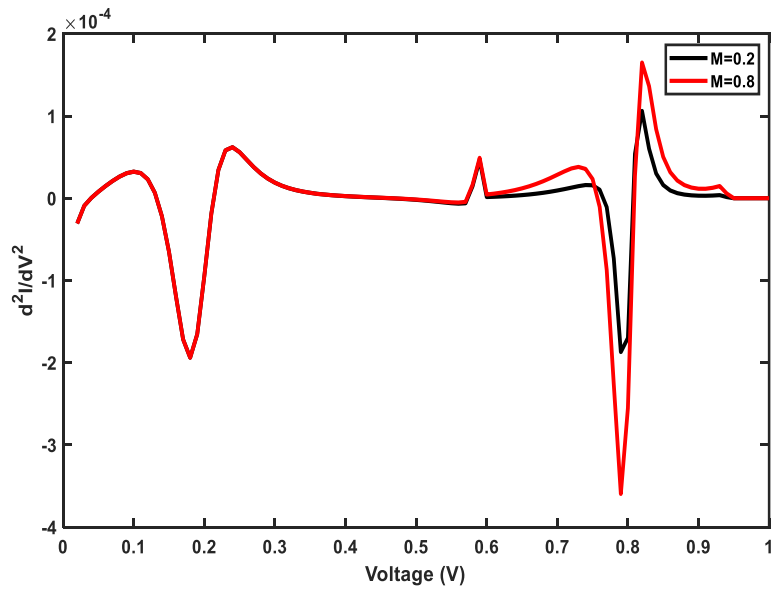


Figure 7.8: The double derivative of Current vs Voltage plot showing the current through the sensor when a foreign molecule of different handedness interacts (black curve) and when a foreign molecule of same handedness interacts (red curve).

To measure the enantioselectivity of the sensor (receptor in this case), enantioselectivity index is defined as

$$\text{Enantioselectivity Index} = \frac{IETS(\text{same - spin}) - IETS(\text{opp - spin})}{IETS(\text{same - spin}) + IETS(\text{opp - spin})}$$

Eq. 7.3

where IETS is the intensity of the peak corresponding to the vibrational mode in the plot of the double derivative of current.

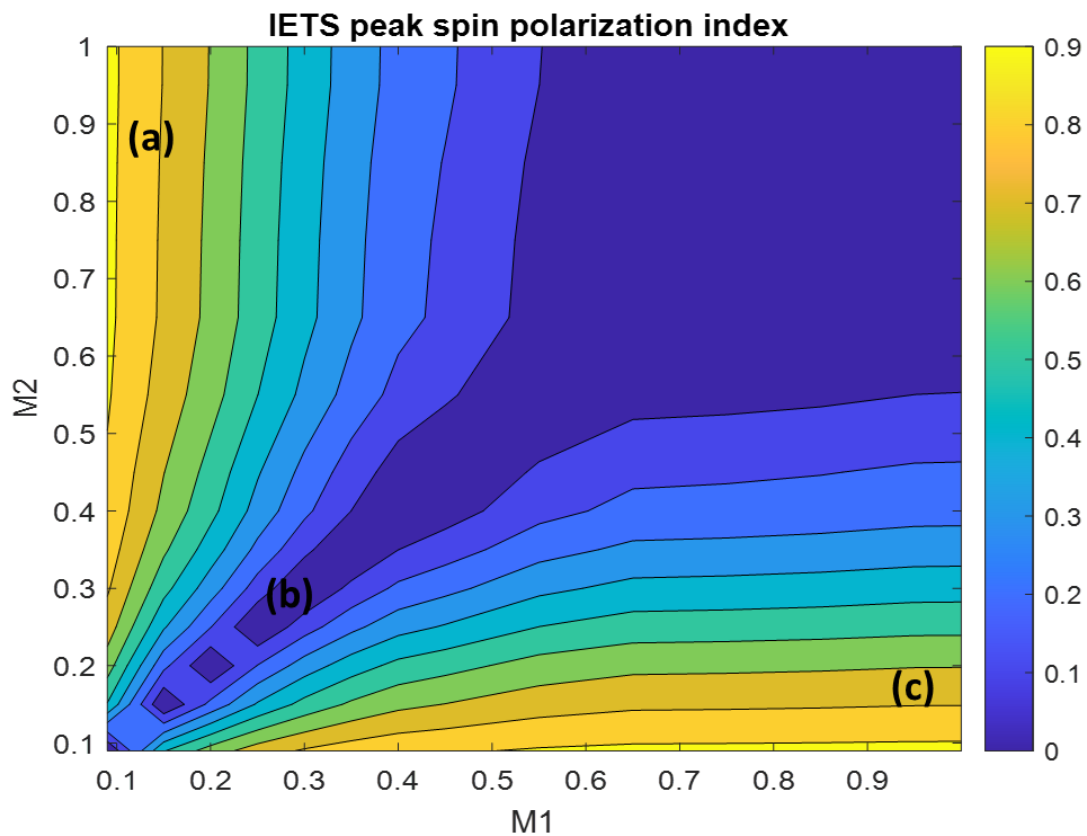


Figure 7.9: The contour plot shows the IETS peak spin polarization index as function of electron-phonon coupling for similar handed molecules vs opposite handed molecules (a) The point on contour plot shows maximum enantioselectivity. Receptor is L and odorant is L. (b) This point shows minimum enantioselectivity. Receptor is L and odorant is R or Receptor is R and odorant is L. (c) The point on contour plot shows maximum enantioselectivity. Receptor is R and odorant is R.

The similarity between the IETS peaks can measure the enantioselectivity of the system. The index defined is based on the assumption that the more difference there is to the intensity of IETS peaks more will be the enantioselectivity. The electron-phonon coupling is varied to a range of 0.0 to 1.0 as the value commonly used in simulation setup [88]. The contour plot of the enantioselectivity index shows 3 points: point (a) and (c) shows maximum enantioselectivity implying that receptor and odorant should be of similar handedness. The line on the contour plot along point (b) are points with the same electron-phonon coupling which show minimum enantio-selectivity.

7.3 Conclusion

The investigation of a chiral receptor as the potential candidate for an enantioselective electronic nose sensor within the framework of Inelastic electron tunneling and vibrational theory of olfaction. It has been shown theoretically that the inclusion of spin polarization along with charge polarization due to chirality-induced spin selectivity (CISS) effect in the receptor can form the basis of enantioselectivity in electronic nose sensors. The vibrational theory of Olfaction answers some questions about the conventional shape theory of olfaction but differentiating enantiomers is one of its limitations. In this study, an attempt has been made to combine the effect of CISS with IETS. It was observed that the spin polarization caused by CISS in the receptor generates a different inelastic current in the IETS simulation setup. The magnitude of this inelastic current depends upon the handedness (enantioselectivity) of the odorant molecule which is interacting with the receptor. This enantioselectivity gets manifested in the system through electron-phonon coupling. The enantioselectivity index is used to quantify and present the enantioselectivity of the sensor.

7.4 Appendix

7.4.1 Psi4

Psi4 is a free and open-source ab initio electronic structure application which provides the efficient implementations of most quantum chemistry calculations such as Hartree–Fock, density functional theory, many-body perturbation theory, configuration interaction, density cumulant theory, symmetry-adapted perturbation theory, and coupled-cluster theory [89]. It

requires an input file containing the coordinates of all the atoms, values of parameters such as convergence limits, memory limit, type of algorithm to be used and the computations to be performed. The output file containing the results is returned after a certain amount of time.

7.4.2 Avogadro

Avogadro is an open-source, cross-platform, three-dimensional molecular builder and visualizer [92], which is used to optimize the geometries of the molecules as well as to generate the input files for SAPT simulations to be run in PSI4 software. This software has tools to visualize and orient the molecules according to user's preferences. It also allows the user to choose the type of optimization algorithm, convergence limits and force fields to accurately optimize the geometries of molecules.

7.4.3 Artificial Chiral Receptor

Besides the computation of interaction energies between the enantiomeric pairs, a helical chiral receptor (motivated by the working of human olfactory receptor) was constructed to investigate the enantioselective nature of its interaction with a pair of odorant enantiomers. The receptor used in this work is an oligopeptide, L-poly-(7)-alanine, Figure 7.10. It consists of a polymeric chain of seven alanine molecules (a common amino-acid) having a secondary structure known as alpha helix. This receptor used here serves as a proxy for human olfactory receptor (G-protein coupled receptor GPCR). The dihedral angles for this receptor are $\Phi = -60^\circ$ and $\Psi = -40^\circ$. The N-terminus and C-terminus of this peptide are both electrically neutral (have -NH₂ and -COOH at its two ends) [93]

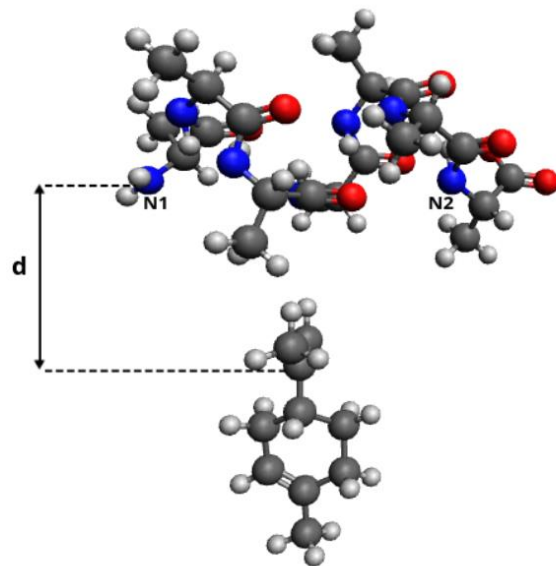


Figure 7.10: Alignment of the Receptor (peptide) and R-(+)-Limonene3.3.2

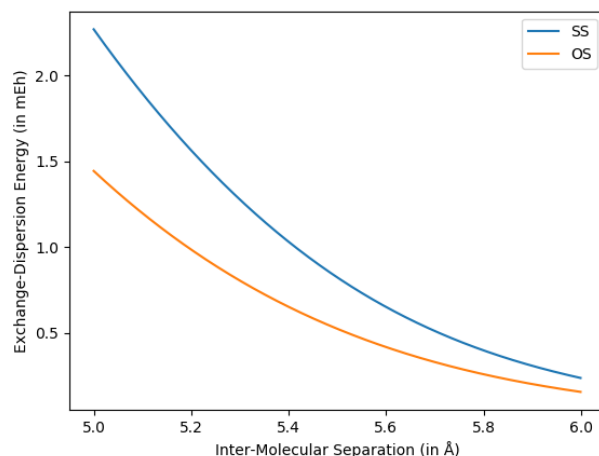


Figure 7.11: Exchange-dispersion Energy Plot for Receptor-Odorant Interaction

Chapter 8

8. Towards Application: Identification of Volatile Organic Compounds for quantifying the freshness of Mangoes

A simple EN sensor maps some physicochemical properties of the odorant molecule to its perception. The perception is, however, subjective to the person perceiving it. The machine cannot be subjective and can increase its efficiency by clearly identifying the molecules. In earlier sections, we tried to figure out how the inputs and outputs of vibration-based sensors fit together. Since vibration sensors based on IETS are still in their early stages [16, 56], it is worth looking into sensors that can use the sensitivity and specificity of real olfactory receptors (ORs). This study moves ahead of mapping vibrational mode to the perception of the volatile organic compounds (VOCs) to mapping the VOCs to a particular OR-based sensor. ORs are GPCRs and are known to be responsive to different VOCs. In this study, an attempt has been made to map the VOCs to particular ORs to make ORs-based sensors for detecting the freshness of fruits.

8.1 Motivation

Mangifera Indica (MI), also known as mango is a fruit of high commercial value with great nutritional content. The importance of mango increases many folds because of its connection to human experience and emotions. The quality control and monitoring of the health of mango is also attached to a bigger purpose of waste reduction and food quality insurance.

Smart packaging systems that exist in market focus primarily on quality assessment of meat products and beverages. Fruits are also prone to spoilage, and have been the source of disease outbreaks [94]; at the same time, they constitute one of the most nutritious food sources known to us. Therefore, it is imperative to develop tools for freshness monitoring.

There are many physical parameters of MI that can be used in the quality assessment depending upon the technology to be harnessed. Visual properties like the color and blackspots of the skin, shape of the mango can be used in computer vision technology-based freshness sensors. In some cases, it has been found that visual properties might not be the best marker for quantifying the quality and freshness.

To find better markers, Volatile Organic Compound (VOC) profile of Mangifera indica can be utilised for the same purpose [95]. VOCs are organic compounds characterized by low molecular weight, high vapor pressure, low boiling point, and low solubility in water. The high vapor pressure and low molecular weight facilitate the easy diffusion of VOCs in the air. Almost all fruits and vegetables produce volatile organic compounds at different stages of their life cycle, making them ideal biomarkers to assess the quality of these products (schematic shown in Figure 8.1).

The VOCs produced in the process of growth and then deterioration usually follow a fixed pattern depending upon the conditions they have been subjected to. The emission of volatiles also depends upon the biosynthetic pathway involved in the metabolism of the plant and can be emitted as primary or secondary products of the metabolism [96]. These volatiles produced by the fruit, distributed over time, contribute to its **VOC profile**.

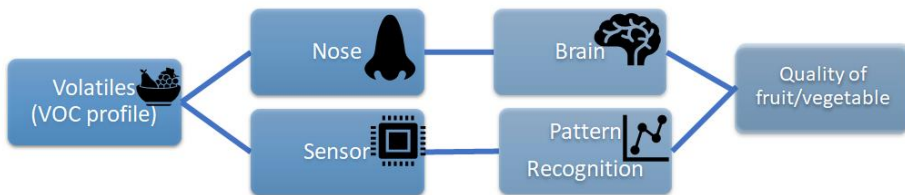


Figure 8.1: Identification of VOCs for measuring the quality of fruits or vegetables.

8.2 VOC Profiling and -Bio-active components of *Mangifera Indica*- Literature Review

The development of fruits can be divided into 3 stages: Maturation, Ripening and Senescence. The maturation of fruits refers to its biological growth, ripening refers to change in color, aroma and texture to reach desirable stage of consumption. Senescence is defined as the stage when fruits exceed their peak maturity and lead towards deterioration.

Mangifera Indica is a climacteric fruit, i.e., it ripens even after it has been harvested. During this process they emit ethylene along with increased rate of respiration. So, its freshness usually depends upon emission of ethylene and other VOCs [96]. Ethylene is a plant hormone responsible for the maturation and development of climacteric fruits. There have been chemoresistive, electrochemical sensors reported in literature responsible for detecting ethylene. But these sensors are sensitive to other compounds also which limit their selectivity. Along with Ethylene other secondary volatile organic compounds are emitted which can be used for freshness (ripeness) detection.

The total bioactive components found in *Mangifera Indica* includes carotenoids, ascorbic acid, polyphenols etc. Carotenoids are molecules found in abundance in all fruits. Beta-cartene is the carotenoid found in MI which is responsible for its color and ripening. The volatile organic compounds emitted by mangoes, shown in Table in 8.1, have compounds ranging from terpenes, aldehydes to alcohols [97]. In mangoes **terpenes** are most important volatile substances as shown in Figure 8.2. **Terpenes** are a class of natural products of compounds

with the formula $(C_5H_8)_n$ which comprises more than 30,000 compounds, predominantly produced by plants

Table 8.1: VOC profile of MI

3-carene
α -copaene
α -humulene
α -pinene
α -terpinolene
β -caryophyllene
β -pinene
Cedrol
decanal
ethanol
γ -terpinene
limonene
Methyl Decanoate
myrcene
octanal
toluene

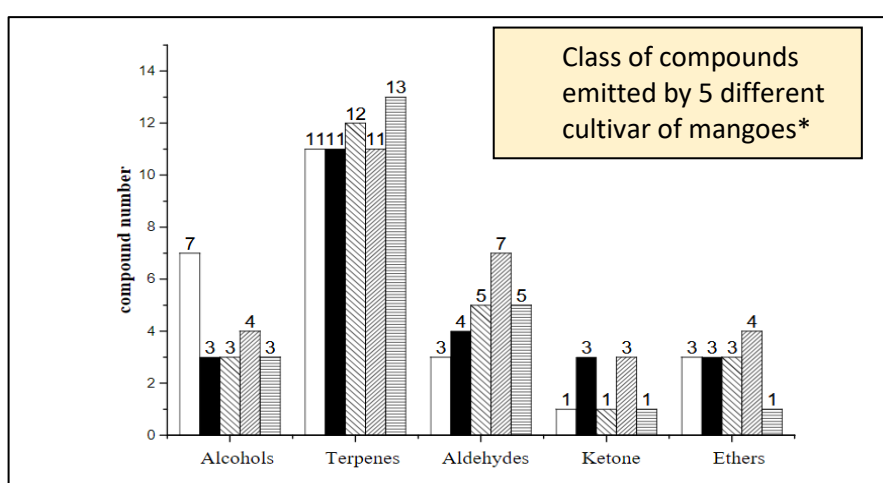


Figure 8.2: Class of compounds emitted by different cultivars of *Mangifera Indica* [96]

8.3 Biorecognition Element and Bio-reception

Biosensors require a biological and an artificial component, the bioreceptor and transducer respectively, in order to output a readable signal. This common scheme is illustrated in Figure 8.3. The analyte in question here is a specific fruit VOC that is to be sensed. Research in the field of Olfactory Receptor (OR) -based bioelectronic sensors is indeed recently emerging as a simpler strategy to detect **environmentally significant VOCs**. It has been suggested that given their high specificity and sensitivity, Olfactory Receptors (ORs) are the ideal candidates for the receptors in a biosensor [98]. Now, ORs can be expressed and purified easily and are stable to perturbations in temperature, pH and proteases. They have been used to engineer systems that can detect floral odorants, alcohols and explosives.

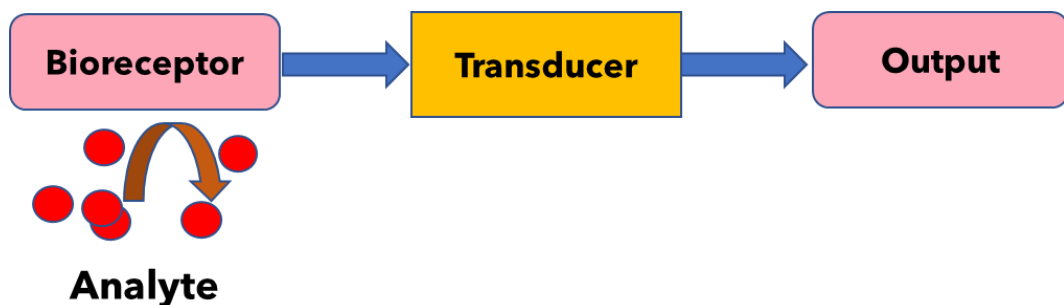


Figure 8.3: Schematic of a biosensor

To emulate the power of biological olfaction by using ORs in the biosensor. Developing a rigorous way to identify the biomaterial (OR) that can best sense a specific VOC of interest. The study focusses on the functionalization of available transducers with OR proteins.

Olfaction is a primary sense in insects which enables them to find mating partners, locating oviposition habitats, foraging, and avoiding predators. *Drosophila Melanogaster* (fruit fly) has a characteristic to linger around overripe or rotting fruit, Figure 8.4. The olfactory system of *Drosophila* has a repertoire of **approximately 60 odorant receptors** [99]. Molecules bind to odorant receptors with different affinities and activate them with different efficacies, thus providing a combinatorial code that identifies odorants. The ORs of *Drosophila*, **Or19a and Or98a**, have been found to be receptive to the molecules present in VOC profile of *Mangifera Indica*.

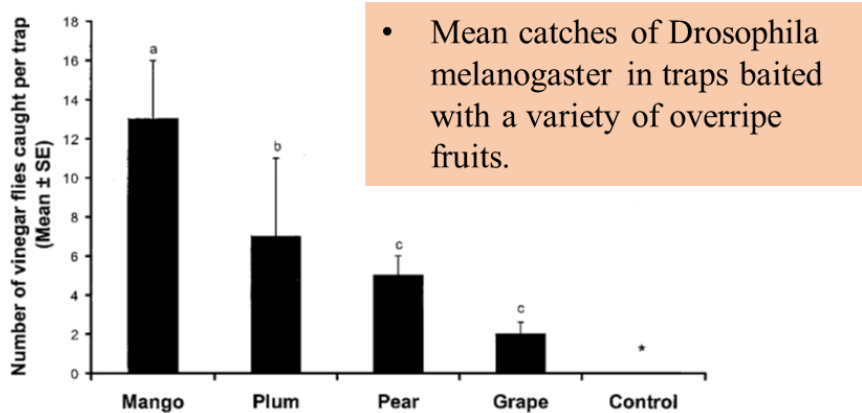


Figure 8.4: Response of Drosophila to 5 different fruits [94]

Olfactory Receptors belong to Class A G-protein Coupled Receptors (GPCRs). GPCRs consist of seven transmembrane helices (TM1–7) connected by three extracellular loops (ECLs) and three intracellular loops and an intracellular C-terminal helix 8, as explained in detail in Chapter 2. The orthosteric agonist binding sites of class A GPCRs are located in an extracellularly accessible binding pocket formed by the TM region, N terminus, and extracellular loops [100].

The research in the field of Olfactory Receptors based electronic nose sensors is evolving as many scientific prototypes exist. The main challenge is to develop a product that can be used at a consumer level. In moving from a single molecule to device in the context of sensors, it is very important to have clear an idea about signal transduction. Signal transduction in biological olfactory systems is not clear and still a topic of active research.

There are many standard transducers available that can be explored for their compatibility with olfactory receptors.

Table 8.2: Protein-peptide based biosensors for VOC detection [101]

Receptor/ Peptide	VOC	Surface	Transducer
mOR174-9	Acetophenone	CNT	CNT based FET
pOBP (odorant binding protein)	Methanol, ethanol	Si	Si-substrate with interdigitated electrodes (EIS)
RVNEWVIC (hORp193) humanOR1E	Acetic acid	Gold	Piezoelectric multiarray analyser/QCM/conductance
TKCVSLMAGTVNKKGEFFFF (LUSH OBP)	3-methyl-1-butanol	CNT	Field-effect transistor
AYSSGAPPMPFF (A3)	Acetonitrile; di-chloromethane; methyl salicylate	Gold nanoparticle	Inductor-capacitor-resistor resonators
HSSYWYAFNNKTGGGGWFVI(P1-ASP1C peptide) (honey bee antenna OBP)	Trinitrotoluene (TNT)	SWCNT	Field-effect transistor

8.3.1 Homology Modeling

The research around olfactory receptors based artificial nose is limited due to the limited information available about the 3-dimensional structure of proteins. Modeling techniques like Homology modeling and machine learning based methods have been used for prediction of 3-D structure of protein. In homology modeling, a library of experimental protein structures is searched to identify suitable templates for a given target protein (see Figure 8.5). Many known structures of class A GPCRs have been used as templates for homology modelling of Olfactory Receptors. Homology model can be generated for different receptors.

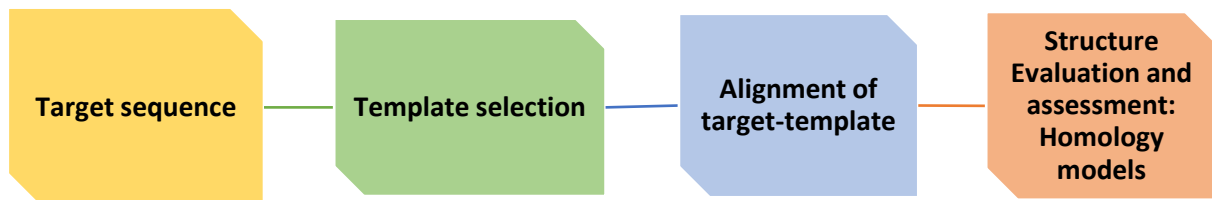


Figure 8.5: Schematic of flow of steps in Homology Modeling

AlphaFold is an AI system developed by **DeepMind** that predicts a protein's 3D structure from its amino acid sequence. Its accuracy is comparable with experiment. The 3-D structure

of proteins used in this work, Figure 8.6, has been obtained from the AlphaFold database [102].

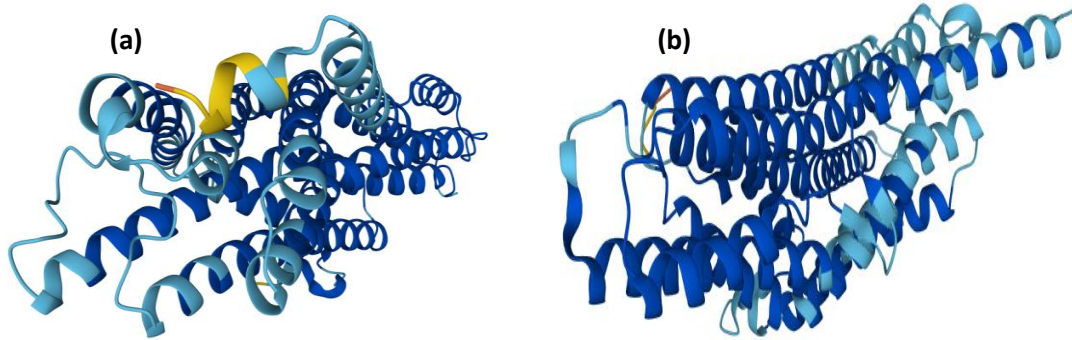


Figure 8.6: Predicted 3-D structures of (a) Or98a and (b) Or19a from Alphafold database

8.3.2 Binding Energy and Prediction of Docking Site

In the process of signal transduction from a molecule (VOC) to its perception in brain, the first step is the interaction between ligand (VOC) and receptor. Docking is a molecular modelling technique that is used to predict how a protein (receptor) interacts with small molecules (ligands). **AutoDock VINA** [103] is an open-source docking engine which predicts docking site and conformation of the ligand-protein system. To understand the interaction of ligand (VOCs) with receptor, the binding energy of ligand-receptor complex is to be calculated. The binding energy is given by:

$$\Delta G = -RT \ln(k_b)$$

Eq. 8.1

The lower the binding energy of interaction is the more stable the system is. AutoDock calculates the binding energy of the ligand bound receptor using the formula:

$$\Delta G = V_{bound}^{L-L} - V_{unbound}^{L-L} + V_{bound}^{P-P} - V_{unbound}^{P-P} + V_{bound}^{P-L} - V_{unbound}^{P-L} + \Delta S$$

Eq. 8.2

where L refers to the “ligand” and P refers to the “protein” in a ligand-protein docking calculation.

Binding event between ligand and receptor is coupled with a negative Gibbs' binding free energy, which is the sum of an enthalpic, and an entropic term:

$$\Delta G = \Delta H - T\Delta S$$

Eq. 8.3

where G is Gibbs free energy, ΔH is enthalpy, ΔS entropy, and T is the temperature. The enthalpic contribution include ionic, halogen, and hydrogen bonds, electrostatic (Coulomb) and van der Waals interactions and entropic contribution measures the dynamics of the overall system. To understand the type of interaction taking place between the protein and ligand the modeling technique of Interaction Fingerprinting [104] is used. The interaction fingerprint (IFP) concept consists of converting a 3D protein–ligand complex into a 1D bit string registering intermolecular interactions (hydrophobic, hydrogen bonds, ionic interactions) between a ligand and a fixed set of active site residues. IFP assigns precalculated interaction energy weights to ligand atoms in direct contact with the target. A python-based open-source package PyPLIF [105], compatible with AutoDock VINA is used to obtain IFP bit string.

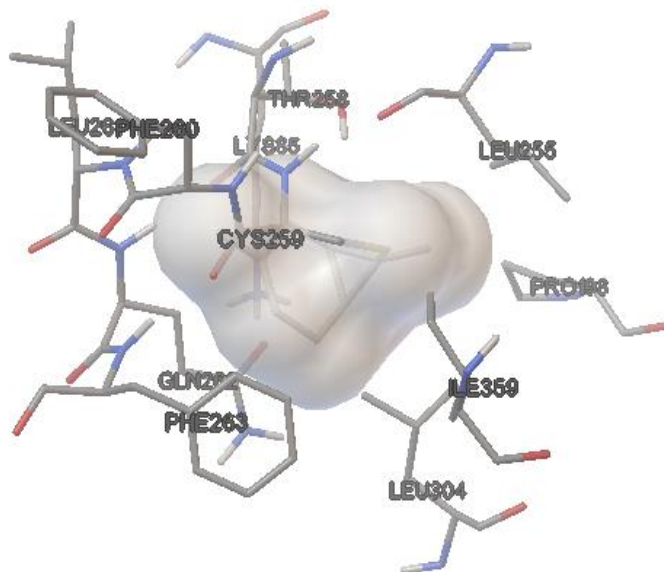


Figure 8.7: The binding site as identified by AutoDock

8.3.3 Results and Analysis

To create a combinatorial code for sensing the VOC profile of *Mangifera Indica*, 25 olfactory receptors were docked with 16 VOCs from its VOC profile. The docking scores were generated in AutoDock VINA using blind docking. Blind docking refers to docking a ligand

to the whole surface of a protein without any prior knowledge of the target pocket. Blind docking involves several trials/runs and several energy calculations before a favourable protein-ligand complex pose is found, example Figure 8.7.

Table 8.3: The Binding Map obtained in AutoDock VINA, each OR of drosophila was docked with all the 16 molecules from VOC profile of MI

	β -carenene	α -copaene	α -humulene	α -pinene	α -terpinolene	β -caryophyllene	β -pinene	cedrol	decanal	ethanol	γ -terpinene	limonen	methyl decanoate	myrcene	octanal	γ -toluene
	1	2	3	4	5	6	7	8	9	10	11	12	13	14	15	16
Or2a	-7.38	-8.331	-7.346	-6.906	-6.205	-7.435	-6.889	-7.98	-5.34	-2.552	-6.815	-6.529	-4.779	-5.869	-4.68	-5.987
Or7a	-6.25	-7.031	-6.861	-5.669	-5.944	-6.815	-5.483	-6.73	-4.961	-2.577	-6.018	-5.942	-4.734	-5.434	-4.202	-5.068
Or9a	-5.888	-6.329	-6.597	-6.786	-5.922	-8.24	-6.616	-6.234	-4.179	-2.449	-6.745	-6.978	-6.02	-5.658	-4.01	-5.616
Or10a	-5.923	-6.713	-6.389	-5.671	-5.781	-6.943	-6.435	-6.499	-5.023	-2.44	-5.428	-6.46	-3.971	-4.52	-4.845	-5.504
Or19a	-6.003	-7.119	-7.538	-6.339	-5.338	-7.5	-6.277	-7.688	-5.7	-2.525	-5.71	-5.76	-4.6	-5.2	-4.33	-4.8
Or22a	-5.7	-7.185	-6.28	-5.698	-6.828	-7.114	-5.488	-6.647	-4.163	-2.79	-6.766	-6.427	-4.256	-4.988	-4.018	-6.052
Or22b	-5.752	-7.154	-7.311	-5.882	-5.909	-7.446	-6.408	-7.694	-4.395	-2.691	-5.601	-5.75	-4.176	-4.821	-4.228	-5.338
Or23a	-6.643	-8.8266	-7.11	-6.343	-6.428	-7.023	-6.442	-6.6	-4.795	-2.66	-6.443	-6.528	-4.538	-5.534	-4.417	-5.848
Or35a	-5.593	-6.483	-6.511	-5.187	-5.506	-6.975	-5.029	-6.219	-4.417	-2.647	-5.61	-5.518	-4.136	-4.984	-4.08	-4.57
Or42a	-5.968	-6.405	-6.357	-5.345	-5.962	-6.35	-5.249	-6.102	-3.962	-2.704	-5.241	-5.466	-4.261	-4.608	-4.674	-4.174
Or43a	-7.001	-8.627	-8.368	-6.528	-6.956	-6.212	-6.541	-6.441	-4.365	-2.441	-6.543	-6.55	-4.26	-6.386	-4.726	-5.431
Or46a	-6.163	-7.486	-6.126	-5.47	-6.228	-6.609	-5.617	-6.501	-4.763	-2.524	-6.078	-6.217	-4.337	-5.165	-3.701	-4.628
Or47a	-6.79	-6.367	-6.25	-6.36	-5.76	-6.669	-6.098	-6.434	-5.327	-2.627	-7.171	-6.971	-3.997	-4.387	-5	-5.649
Or56a	-5.727	-7.514	-6.296	-6.257	-6.198	-7.036	-6.202	-6.609	-4.545	-2.798	-5.887	-5.919	-4.671	-4.678	-4.243	-4.713

Or59a	-5.834	-7.039	-7.154	-6.233	-5.668	-7.258	-6.033	-7.129	-4.222	-3.053	-5.655	-5.595	-4.31	-4.861	-3.923	-4.949
Or59b	-5.491	-6.982	-6.479	-5.252	-6.674	-6.492	-5.648	-6.75	-4.308	-2.74	-5.558	-5.573	-4.217	-4.6	-3.845	-4.447
Or63a	-5.488	-6.664	-6.279	-5.516	-5.179	-6.166	-5.468	-5.817	-4.028	-2.56	-5.447	-5.463	-3.949	-4.771	-3.772	-4.512
Or65a	-8.893	-7.767	-8.03	-6.521	-7.619	-7.841	-6.956	-6.525	-4.64	-2.7	-7.787	-7.685	-4.291	-5.506	-3.995	-6.328
Or67a	-6.047	-6.73	-6.666	-5.665	-5.719	-6.538	-5.573	-6.332	-4.298	-2.541	-6.091	-7.515	-6.386	-4.54	-5.548	-6.25
Or67d	-6.121	-6.388	-5.966	-5.866	-6.181	-6.244	-5.923	-6.396	-3.916	-2.811	-6.035	-5.666	-3.918	-4.331	-4.48	-5.315
Or82a	-5.975	-6.653	-6.803	-5.964	-5.473	-7.289	-5.156	-6.872	-4.056	-2.524	-5.29	-5.375	-4.377	-4.715	-3.863	-4.632
Or83a	-7.182	-6.166	-6.151	-6.353	-6.694	-6.369	-6.662	-6.258	-3.607	-2.732	-6.454	-5.23	-4.3	-4.282	-3.911	-5.347
Or85a	-6.119	-6.829	-6.49	-5.594	-6.482	-6.5	-6.273	-6.44	-5.364	-2.535	-6.932	-6.947	-4.488	-5.39	-4.53	-5.686
Or88a	-5.423	-7.071	-6.359	-5.449	-6.33	-6.78	-6.72	-6.652	-4.48	-2.803	-5.95	-5.95	-4.631	-5.066	-4.233	-5.548
Or98a	-6.282	-7.022	-6.556	-6.159	-7.066	-6.554	-6.145	-7.14	-5.096	-2.736	-6.593	-6.538	-3.99	-4.992	-3.909	-5.57

Principal Component Analysis

Principal Component Analysis (PCA) can be used to optimize the number of receptors. Principal Components (PC) obtained from applying PCA on 16x25 matrix show that PC1 accounts for 87% variance in the data. The loadings of PCs indicate whether a variable has a strong or weak effect on the loadings. The criterion to decide the weightage of loadings is derived from the reciprocal of square root of number of columns.

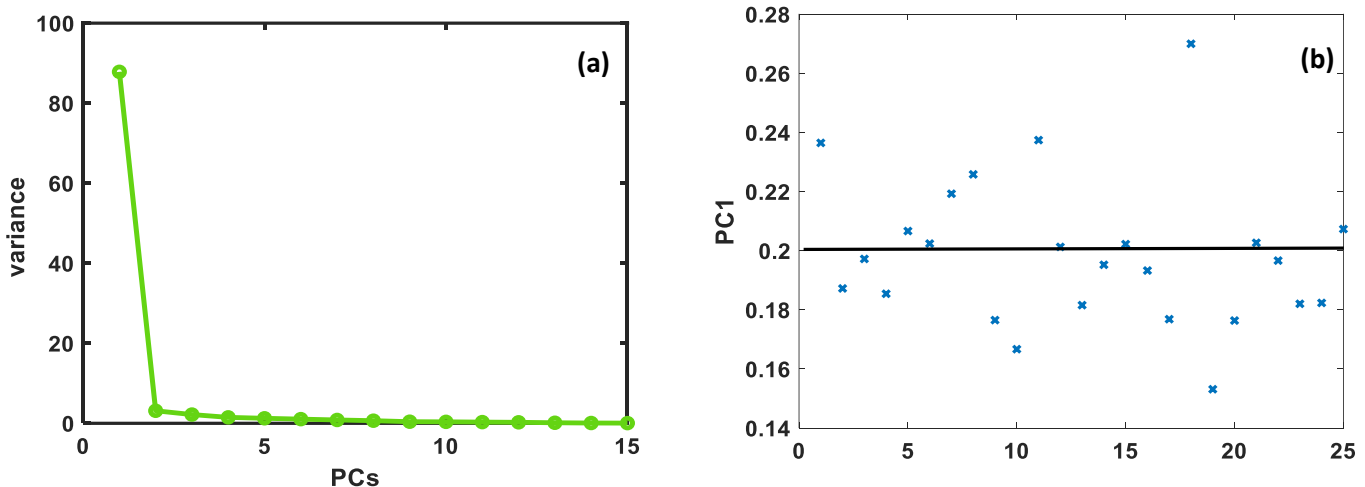


Figure 8.8: (a) Plot of Variance Vs principle components. PC1 comprises of almost 87% variance in the data. (b) Loadings of PC1, the cut-off for the 16 x 25 matrix comes out to be 0.2. All the points above 0.2 dominate the response of this matrix.

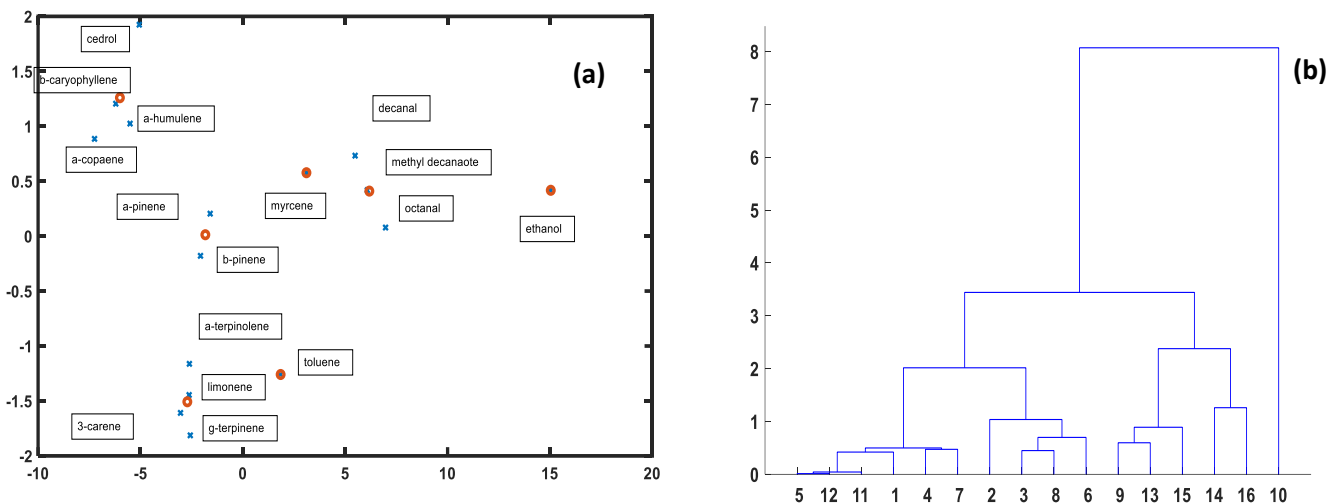


Figure 8.9: (a) 16 molecules visualized in the 2-D space of PC1 vs PC2 . (b)The hierarchical clustering of molecules with respect to PC1.

Plotting the VOCs in the 2-dimensional space of PC1 vs PC2, Figure 8.9(a), groups similar type of molecules in one cluster. The cluster containing 6 terpene molecules was chosen as the class of significant similar response. Now the matrix got reduced to 6×11 , applying PCA further on this optimizes the no of receptor to 5. After final optimization 5 receptors can give the complete response of these 6 VOCs. The five receptors are **Or2a**, **Or19a**, **Or22a**, **Or46a**, **Or65a**.

8.3.4 Interaction Fingerprinting

To understand the interaction of ligands with the protein it is important to analyze the type of interactions taking place between molecule and the protein in the binding site. The interactions can be hydrophobic, electrostatic, hydrogen bond, etc. Electrostatic interactions take place between oppositely charged atoms. Attractive Van der Waals interactions is due to 2 induced dipoles arising from fluctuations in charge densities between adjacent uncharged atoms whereas repulsive Van der Waals interactions occur when distance between two atoms is very small such that their electron clouds start to overlap. Hydrogen bonds are non-covalent, attractive interactions between a hydrogen covalently bonded to some electronegative group (“donor”), and another electropositive atom(“acceptor”). Interactions between aromatic rings is pi–pi interactions and contributes to protein and DNA stability. The

pi-pi interaction is dominated by dispersion and electro-static (quadrupole-quadrupole) forces.

Table 8.4 Types of Interaction in AutoDock VINA

Types of interaction in AutoDock

1	hydrophobic
2	aromatic face to face
3	aromatic edge to face
4	h-bond (protein is donor)
5	h-bond (protein is acceptor)
6	electrostatic force (protein +)
7	electrostatic force (protein -)
8	hydrophobic + aromatic face to face
9	hydrophobic + aromatic edge to face
10	hydrophobic + aromatic edge to face+ aromatic face to face

The interaction fingerprint between the receptor and protein is a bitstring indicating the type of interaction. Table 8.4 shows the type of interaction in AutoDock VINA and Table 8.5 shows the IFP of Or2a with the 16 molecules of VOC profile of MI

Table 8.5 Interaction Fingerprint of Or2a receptor with 16 odorant molecules, the rows are the molecules of VOC profile of MI and columns represent the binding pocket of OR2a

residues	B.E.	PHE290	PHE309	SER305	PHE390	ILE306	ALA287	VAL286	THR386	TYR387	MET383
molecule 1	-7.38	9	9	1	10	1	1	1	0	0	0
molecule 2	-8.331	1	9	0	9	1	0	0	0	0	0
molecule 3	-7.346	9	9	0	9	1	1	0	0	0	0
molecule 4	-6.906	9	9	0	9	1	1	1	0	0	0
molecule 5	-6.205	1	9	0	9	1	0	0	0	1	0
molecule 6	-7.435	9	9	0	9	1	1	1	0	0	0
molecule 7	-6.889	9	9	0	9	1	1	1	0	0	0
molecule 8	-7.98	9	9	1	8	1	1	1	0	0	0
molecule 9	-5.34	1	1	0	1	1	1	1	0	1	0
molecule 10	-2.552	0	0	0	0	0	0	0	0	0	0
molecule 11	-6.815	1	8	1	9	1	1	1	0	0	0
molecule 12	-6.529	1	9	1	9	1	1	1	0	0	0
molecule 13	-4.779	1	1	0	1	1	1	1	0	1	1
molecule 14	-5.869	1	1	0	1	1	0	1	0	1	1
molecule 15	-4.68	1	1	1	1	1	1	1	0	0	0
molecule 16	-5.987	9	8	0	9	1	1	1	0	0	0

8.4 Relation of physicochemical properties of molecules with their binding score

A functional relationship might exist between molecular volume and the response of the receptor. There might be some way to estimate the *molecular receptive range* or *tuning function* of ORs. There can be some relation between the structural properties of the molecules and receptor-response. The structure properties of 16 VOCs were obtained using a open-source package called VEGA-ZZ [6].

The plot between binding score and lipophilicity and molecular volume shows a significant correlation between these properties and the binding score. A relationship that could be explored as these properties could act as representations of the properties that can be sensed or measured to create sensors for sensing small Volatile organic molecules.

Table 8.6 Molecular weight, Volume and hydrophobicity of molecules in VOC profile of MI

	Molecular weight	Volume	logP (broto)
3-carene	136.23	151.2	2.52
a-copaene	204.3	224.5	3.66
a-humulene	204.3	233.5	3.76
a-pinene	136.23	154.2	2.52
a-terpinolene	136.23	156.2	1.52
b-caryophyllene	204.35	232	4.009
b-pinene	136.23	149.4	2.96
Cedrol	222.36	236.6	3.96
decanal	156.2	183.6	3.7
ethanol	46.09	53.9	0.09
g-terpinene	136.2	156.7	1.8108
limonene	136.23	158.0	2.25
Methyl decanoate	186.28	206.9	4.06
myrcene	136.23	165.3	2.62
octanal	128.1	148.3	2.88
toluene	92.1	97.3	2.26

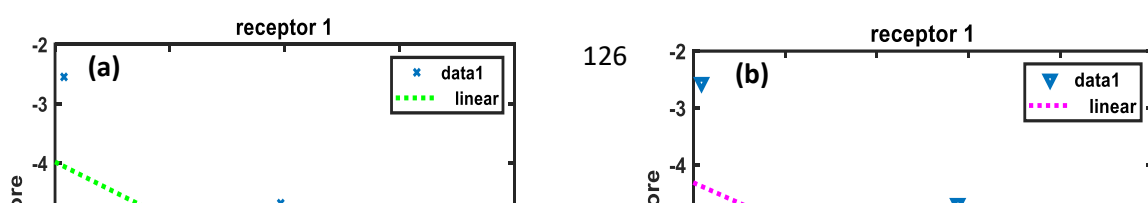


Figure 8.10: (a) Correlation of the binding score of ligand and Or2a with molecular volume and (b) lipophilicity of ligands.

Table 8.7: Correlation values of the binding score of ligand and ORs with molecular volume (right) and lipophilicity of ligands (left). The values in red show low correlation.

Receptor	Correlation between volume and binding score	Correlation between logP and binding score
Or2a	-0.67296	-0.53589
Or7a	-0.76883	-0.57208
Or9a	-0.61001	-0.47969
Or10a	-0.61777	-0.52467
Or19a	-0.82412	-0.69768
Or22a	-0.5303	-0.29604
Or22b	-0.71458	-0.55166
Or23a	-0.61545	-0.44336
Or35a	-0.76655	-0.54634
Or42a	-0.71739	-0.48368

Or43a	-0.57071	-0.35751
Or46a	-0.68321	-0.44798
Or47a	-0.45683	-0.32808
Or56a	-0.70369	-0.50283
Or59a	-0.70775	-0.51359
Or59b	-0.70637	-0.44227
Or63a	-0.68491	-0.48723
Or65a	-0.42165	-0.2158
Or67a	-0.59385	-0.5301
Or67d	-0.49692	-0.30809
Or82a	-0.75929	-0.56744
Or83a	-0.39214	-0.22022
Or85a	-0.57039	-0.39123
Or88a	-0.63626	-0.47464
Or98a	-0.54782	-0.32084

8.5 Sensor Design

8.5.1 Device Design

To make working prototypes of olfactory receptors-based sensors for freshness detection of the fruits and vegetables, it is important to understand the device design. Silicon nanowire-based biosensors are very popular. Silicon industry is well-developed, mature industry with set methods for device fabrication. Such a mature industry also enables the fabrication of Silicon nanowires (SiNWs) with different shapes, dopants, sizes, etc. SiNWs performance also shows a high reproducibility of the devices. In biological research, SiNW-FETs are used for different types of detection including DNA sequences, small molecules, viruses, cancer biomarkers. SiNW-FET sensor has been developed for COVID-19 detection [106].

To simulate the device in Quantum ATK [47] a silicon nanowire was created. The SiNW-FET was created using the graphical user interface of Virtual Nano Lab (VNL). The simulation and modeling of the Si NW-FET without a gate dielectric was generated. Figure 8.11 illustrates the sensor configuration consisting of three regions, the source, drain, and channel. The silicon nanowire edges were saturated with hydrogen. The silicon nanowire was oriented in

the (100) direction, and the two ends were doped to get an n-type doping concentration of $4 \times 10^{19} \text{ cm}^{-3}$ to create the source and drain regions.

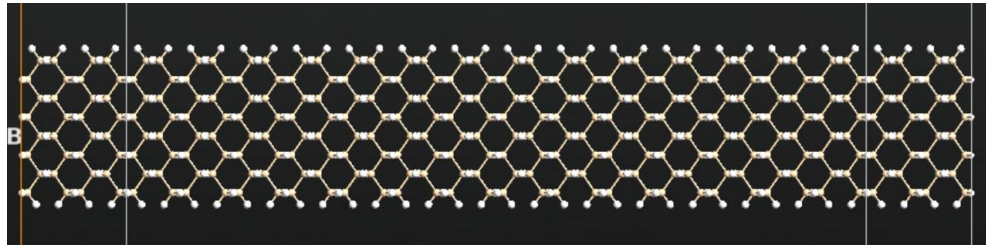


Figure 8.11: ATK-VNL view of SiNW-FET composed of source, drain, and channel. The source and drain are doped with n-type dopants. Silicon—yellow; hydrogen—white.

The SiNW-FET channel had an approximate width of 2 nm and length of 7.6 nm. These dimensions were appropriate to accommodate the number of atoms and the size of the peptide. A pair of 11 Å electrodes was connected at the edges of the channel. It is also important to note that QuantumATK offered computational information for nanoscale sensors, which could be utilised as a proof of concept to back up the experiment based on larger size sensors. All lattice constants and atomic positions were geometrically optimized to reach minimum energy configuration. To increase the stability and longevity of the material, the reactive dangling bonds on silicon atoms were passivated with hydrogen. The bandgap energy of the substance can be altered by these dangling bonds, which changes its semiconductor properties.

8.5.2 Peptide as Sensing material

The sensing material used is the peptide obtained from Or2a olfactory receptor of *Drosophila Melanogaster*. The procedure to choose the amino acid sequence for the peptide starts from identifying the binding pocket using AutoDock VINA, as explained in previous section. The binding pocket is the actual spatial region a ligand acquires in between the transmembrane helices of the receptor protein. The program identifies the amino acids in the primary sequence of the receptor. The binding pocket for Or2a as identified by AutoDock VINA is, **PHE290 PHE309 SER305 PHE390 ILE306 ALA287 VAL286 THR386 TYR387 MET383.**

To make the peptide the amino acid sequence was chosen from 302 – 312. This method of designing peptide is a known method reported in literature [107]. The peptide was constructed in alpha-helix form using UCSF Chimera Tool [108], as shown in Figure 8.12. UCSF Chimera is a program for analysis of molecular structures, its related data including density maps, trajectories, and sequence alignments. It is a platform for interactive visualization and can be used to build peptide. It is available free of charge for non-commercial use.

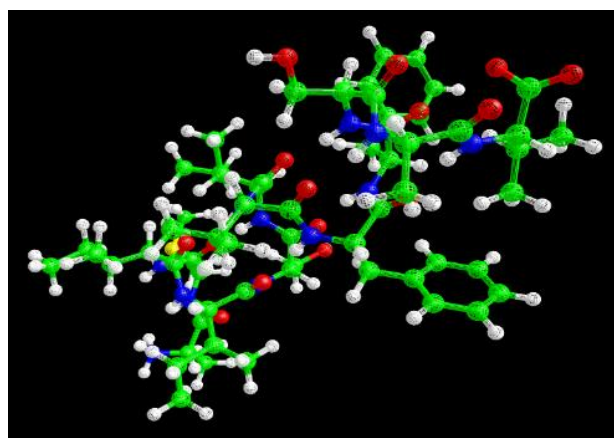


Figure 8.12: Peptide obtained from Or2a receptor around the binding pocket. Peptide is build in the builder of UCSF Chimera.

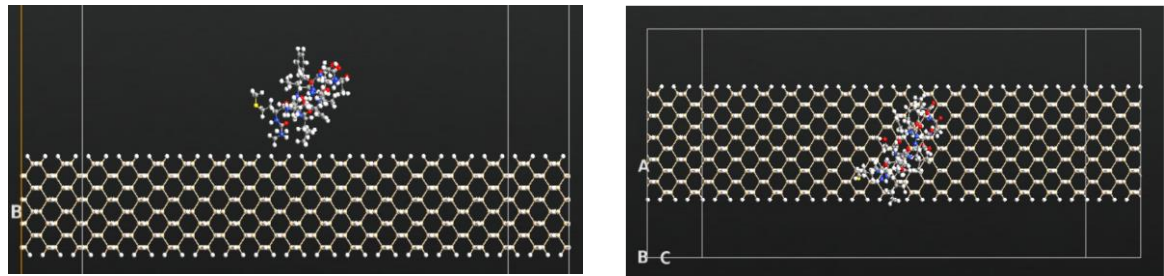


Figure 8.13 shows the SiNW-FET with the peptide and a top view of the channel to study the variation on the electronic transport properties.

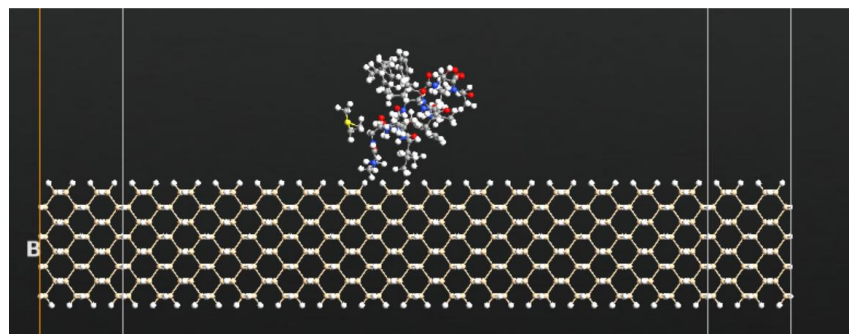


Figure 8.14: ATK-VNL view of ligand bound peptide placed on top of the SiNW-FET channel. The SiNW-FET coated with VOC 3-carene (found in VOC profile of mango) bound to the peptide. The binding configuration was obtained from AutoDock VINA.

The generated peptide is then docked with VOC (3-carene) in AutoDock VINA. The peptide was placed on the silicon and geometry optimization was performed before generating the electronic transport properties for the developed sensor

8.5.3 Computational Methodology

ATK-VNL has various built-in calculators to be used for semi-empirical modelling. NEGF+SC-EH simulations were performed via the ATK-SE semiempirical model to generate the electronic properties of the biosensors. The semi-empirical modelling was used to utilise the experimentally calibrated parameters in the calculations. The sensor performance was analyzed using the nonequilibrium Green's function (Chapter 5) combined with the self-consistent extended Hückel (NEGF+SC-EH) method.[43] Several electronic properties can be studied like conductance, transmission spectrum, electrostatic potential etc. before and after placing peptide on the surface.

The device structure is first created using the ATK builder tool in the ATK-VNL procedure. Next, the script generator produced the designed structure as a Python script. The script generator made it possible to include a built-in calculator with the necessary inputs for the analysis of the nanodevice. The resulting scripts were written in Python and were editable to carry out the necessary simulations. After getting the self-consistent nonequilibrium density matrix, the different electronic transport properties of the sensor can be produced.

8.5.4 Electrostatic Potential

Hartree potential is the potential due to the electron charge density in the system

$$\nabla^2 V_H[n](r) = -4\pi n(r)$$

Eq. 8.4

In a similar fashion, the Hartree difference potential is calculated from the electron difference density as

$$\nabla^2 \delta V_H[\delta n](r) = -\frac{e^2}{4\pi\epsilon_0} \delta n(r)$$

Eq. 8.5

with the electron difference density $\delta n(r)$ being defined through the relation

$$n(r) = \delta n(r) + \sum_I^{N_{atoms}} n_I(r)$$

Eq. 8.6

where $n_I(r)$ is the compensation charge of atom I and N_{atoms} is the number of atoms in the system.

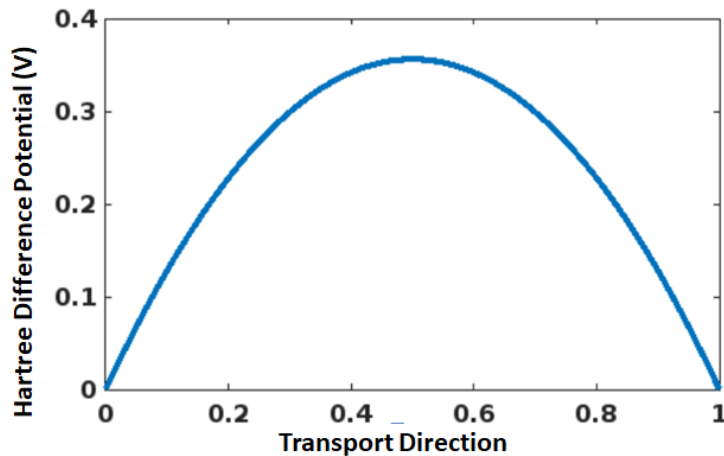


Figure 8.15: Electrostatic Potential difference from left electrode to the right electrode (z-direction) for pristine SiNW.

The electrostatic potential difference gives the change in electron density in the system. the plot shown in Figure 8.15 has zero potential at both the electrodes, which is correct as both the electrodes act as source and sink of the electron so no charge can accumulate at these points. The potential profile is because of the n-i-n structure of the device. Figure 8.16 shows the electrostatic potential difference of the channel when a peptide is added on its top. There is a change in the potential plot of the channel depicting the change in distribution of charge density in the channel due to the presence of peptide.

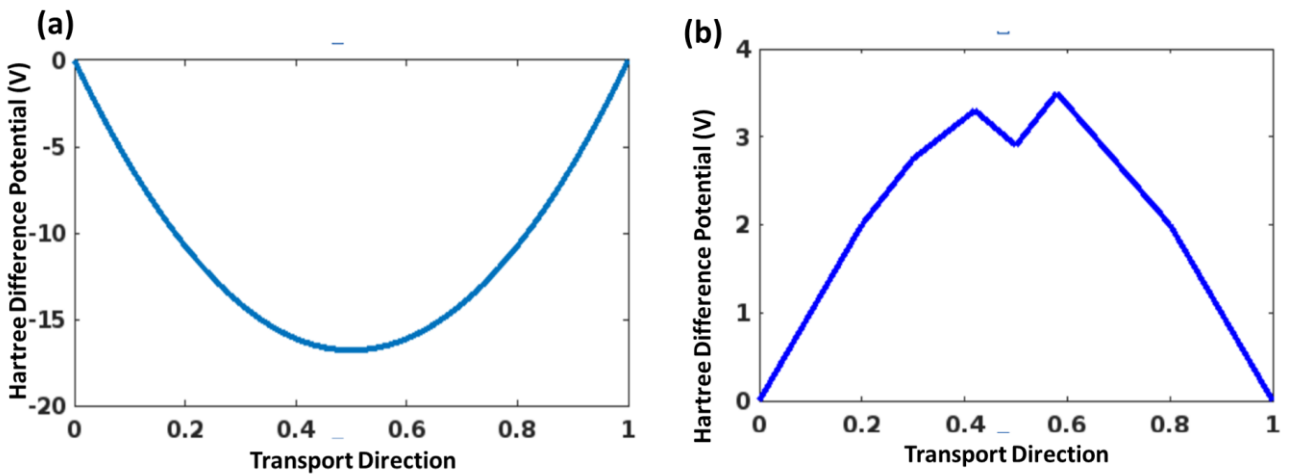


Figure 8.16: (a) Electrostatic Potential difference from left electrode to the right electrode (z-direction) for peptide on top of SiNW. (b) Electrostatic Potential difference from left electrode to the right electrode (z-direction) for docked peptide on top of SiNW.

When peptide is docked with the ligand (VOC), the composition of the molecules, present on the surface of the channel changes and hence change the charge density of the channel. The plot in the Figure 8.16(a) is the plot of the electrostatic difference potential for peptide and 8.16(b) is the electrostatic difference potential plot for ligand bound peptide.

These results are a proof of concept that peptide causes change in the potential profile of the channel.

8.5.4 Transport Calculations

In this sensor design we assume that detection of biomolecules on Si-NW channel between electrodes functionalized with specific receptors that can bind with the target VOC. It has been shown that the response to biomolecules is caused by the coulomb interaction between the biomolecule and the NW that results in change of conductivity of the NW. The sensor design presented deals with a semi-empirical approach of the atomistic view of the Si-NW and the biomolecules. The fluid surrounding the biomolecule (usually water) can significantly affect the electrostatics of the interaction due to its high dielectric constant [109]. The induced charge in the NW is dictated by the net charge profile of the biomolecule and hence of the dielectric properties of the surrounding media. The interaction of charges in dielectric media

is screened by the dielectric constant of the medium. The dielectric properties of the polar liquids depend upon two types of susceptibilities, one local (solvation) and other long-range (dielectric screening) [110]. Here for simplicity only long-range screening is considered, where the interaction energy is made dielectric constant times (ϵ) smaller [110].

The transport calculations were performed using a 1D NEGF simulator in MATLAB. The electrostatic potential profile calculated using QuantumATK was given to the simulator as an input voltage profile. The current and conductance was calculated using self-consistent NEGF formalism for a ballistic device. The potential in the channel has two contributions one interior due to the doping of the contacts as shown in Figure 8.15, second exterior due to the biomolecule (peptide or docked peptide). The contribution due to the doping of contacts is constant but the contribution due to biomolecules changes with docking. The potential change induced due to the olfactory receptor peptide and VOC docked peptide was calculated after subtracting the potential due to contacts from the potential calculated by QuantumATK for peptide (or docked peptide), Figure 8.16 (a) and (b). The resultant potential was scaled down by the factor of 78.5, which is the dielectric constant of the water. The scaling was done to include the screening effect of the fluidic environment surrounding the NW sensor. The scaled potential was then added back to the interior potential to obtain the total potential change induced by the peptide or docked peptide.

The SiNW-FET biosensor demonstrates its ability to detect the presence of the target VOC through alterations in conductivity and current. The plot shown in the Figure 8.17 is the logarithm base 10 of the current calculated from the NEGF simulator for three cases with pristine SiNW, peptide on SiNW and then VOC-docked peptide on the NW. The charge transport properties were computed by the model based on 1-D NEGF current calculation [91] to acquire valid results. This model has the advantage of a low computational cost and low computational time. The two main quantities that illustrate the electron transport efficiency are conductance and current, which are proportional to the transmission probability between the source and the drain based on the Landauer formula explained in Equation 6.9. To quantify the change in current, the current generated by the sensor upon introducing the target molecule can be subtracted from the current of the unmodified sensor. The change in the SiNW-FET sensor's drain current after introducing the peptide occurred as a result of the charges on the peptide, which leads to a negative electrostatic difference potential. The change in the potential induced, Figure 8.16(a), is large because the charges on peptide are not screened by the fluidic environment in QuantumATK. So, when the current is calculated this

potential is scaled by the dielectric constant to include this screening. The current can be seen to change by the order of 3 at 200 mV going from only peptide to VOC docked peptide on the silicon nanowire.

The change in current shows sensing action by the SiNW nano-transistor functionalized with the peptide designed for a particular VOC. The adsorbed peptide interacts with the SiNW-FET channel and modifies its conductivity by modifying the potential of the channel and hence the carrier concentration.

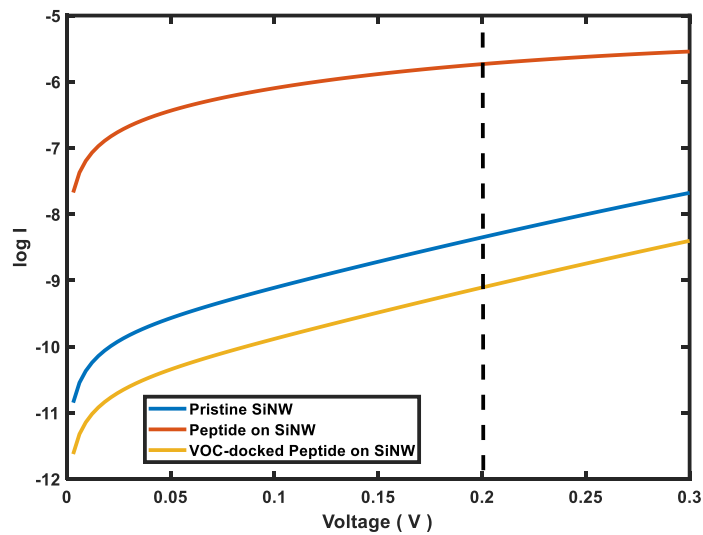


Figure 8.17: The current ($\log I$) - voltage plot of the SiNW nano-transistor for three different cases, pristine SiNW, SiNW with peptide and SiNW with VOC docked-peptide.

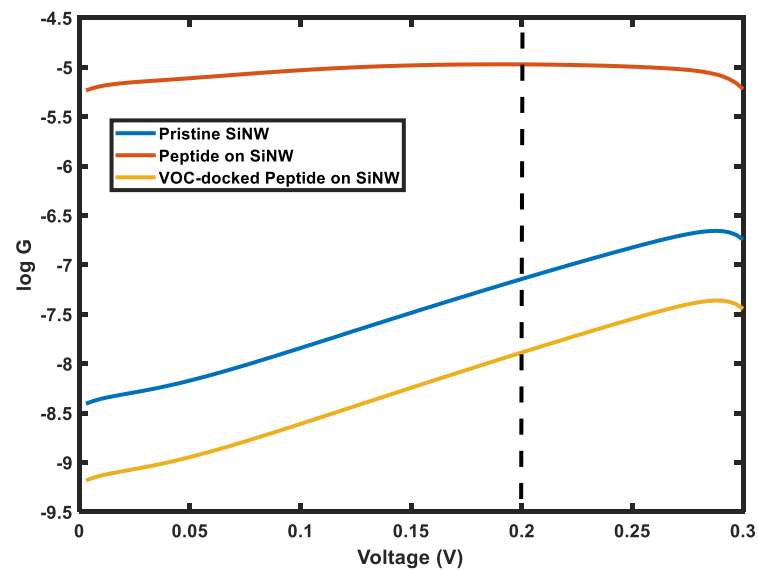


Figure 8.18: The conductance ($\log G$) -voltage plot of the SiNW nano-transistor for three different cases, pristine SiNW, SiNW with peptide and SiNW with VOC docked-peptide.

Figure 8.18 reveals that the bare SiNW-FET has lower conductance than the SiNW-FET + peptide and higher than the SiNW-FET + docked-VOC. The addition of the peptide and docked peptide together modifies the surface of the SiNW-FET resulting in a conductance change in the lower bias region. This change in conductance results in a unique signature due to the physical and chemical structures of the target molecule. SiNW-FET shows a change in conductance of 3 orders at 200 mV. Thereafter, the conductivity gets reduced with the docking of VOC. Every molecule possesses distinct electronic characteristics, dimensions, and interactions with the SiNW-FET channel. The contribution of every molecule is unique, primarily because of its composition and variations in the spatial extension of these molecules.

8.6 Conclusion

Computer vision technology-based sensors for food freshness detection are an upcoming sensing technology. They use the visual medium and compare the picture of the product to the pictures in the database. The visual medium can be misleading, so the need arises to look for other freshness biomarkers. The best way is to look at Volatile organic compounds (VOC) emitted by fruits, vegetables, and plants. It is important to identify a sensing material that will interact with these compounds to make a sensor.

Olfactory Receptors-based electronic nose sensors are evolving as many scientific prototypes exist, but it still is a topic of active research. The first step was identifying the fruit of interest, *Mangifera Indica* (mango). Common knowledge and scientific literature suggest that *Drosophila melanogaster* (fruit fly) gets attracted to fruit, especially MI. To design a sensor array, we tried using the 25 olfactory receptors present on the antenna of the fruit fly. The olfactory receptors interact with the 16 molecules present in the VOC profile of MI.

Since information about the 3-D structure of the olfactory receptor is limited, the homology modeling technique was used to generate the 3-D structure of ORs. Modeling the binding of the receptor protein with the VOCs is a two-step process; first, the binding site is identified, and then the binding energy is calculated. AutoDock VINA is a package for identifying the binding site and energy. The response matrix was generated, including the binding site, energy, and type of interaction between the receptor and the VOC.

A device design based on Silicon nanowires was suggested to make the actual working sensor that detects VOCs emitted by MI. SiNW-based biosensors are utilized for various types of detection, including viruses, cancer biomarkers, small molecules, and DNA sequences. The sensing material used in the sensor design was a peptide designed from the olfactory receptor of the fruit fly.

The device design is only a proof of concept that shows the change in the electrostatic potential of the channel can lead to change in current and conductivity of the nano-transistor with the introduction of peptide (sensing material) and VOC (analyte). This causes the sensing action but more elaborate calculations are required to design the sensor.

Chapter 9

9. Conclusion and Future Work

The following paragraphs summarize the particular conclusions and suggest a way forward from the three investigations:

1. In the first part we have used Chemical Graph theory to establish a link between molecular structure and vibrational spectra. We tried to design an algorithm to understand the physical basis of olfactory mapping from input to output. We proposed a new molecular descriptor called **PD-EVA** to bring physical insight into the odor classification process, but the dataset used is very small. The future work entails to:
 - a. This study can lay the path for understanding the molecular basis of olfaction with a larger dataset and more physical descriptors (work in progress). This can help in low-tech industries like fragrance and cosmetics. A function that maps the molecule to its smell can fill the gap in generic odor sensing.
 - b. A similar study can be done to understand the molecular basis of flavor and taste. These studies hugely impact markets like the artificial flavor industry, plant-based meat, and other food products.
 - c. Realizing an actual IETS-based sensor is ambitious because room temperature IETS is difficult. The active research in making devices and setup that can perform room temp IETS can help in accomplishing vibration-based sensors.
2. A limitation of the VTO is that it cannot explain why enantiomers smell differently, even though their vibrational spectra are similar. In the second part of the thesis, we discussed that the inclusion of spin polarization in chiral systems could lead to enantioselectivity. We have investigated chiral transducers for enantioselective olfactory sensing within the framework inspired by the Vibration Theory of Olfaction, viz. detecting molecular vibrations through inelastic electron tunnelling spectroscopy (IETS). Broadly, we predict that the combined effect of chirality-induced spin selectivity (CISS) with IETS can form the basis of enantioselectivity in olfactory sensors. This conclusion obtains through the following steps. Firstly, the experimental findings reported in literature show that charge polarization can be accompanied by spin polarization. This formed the basis of interaction mechanism between chiral

molecules. This interaction is more repulsive for opposite handedness and less repulsive for alike chirality. The overall interaction has an exchange-dispersion term which is based on exchange interaction, a pure quantum-mechanical effect. This term is spin-dependent and is the reason for origin of the enantiospecific term. This enantiospecific term between chiral odorants is calculated using SAPT calculations which can be extended to the situation of a chiral olfactory transducer with a chiral odorant molecule adsorbed upon it, thereby confirming the chirality-dependent spin polarization due to CISS.

Secondly, the idea of vibration-based sensing for electronic-nose sensors was extended to chiral odorants. We show how the inclusion of exchange-dispersion term in the interaction can lead to a chirality-dependent, or enantioselective, coupling between the electrons in the transducer and localized vibrational modes due to the odorant. Thirdly, we present the design of an enantioselective sensor with source, drain and a chiral channel, where the channel interacts with a chiral odorant. We perform NEGF calculations of the current through the transducer to show that enantioselective electron-vibron coupling can lead to an enantioselective Inelastic Electron Tunnelling current. Thus, we show that this simple expedient, of making IETS based sensors chiral, suffices to address two standing concerns about the vibration framework – lack of enantioselectivity, and lack of shape/conformation information. In conclusion, our work suggests a promising route towards enantioselective ‘quantum biomimetic’ electronic nose sensors. Future work in this comprises of:

- a. Atomistic simulation to understand the combination of CISS and IETS.
- b. Experimental setup that can combine IETS and CISS in realizing a sensor that can be differentiate between enantiomers.
3. As IETS based sensors are still in nascent stage so in the third part we explored olfactory receptor-based sensors for a more practical application. The idea is to make a freshness detection sensor for MI (mango) based on its VOC profile. The VOC profile is the group of volatile organic compounds emitted by mango during its ripening process. The design of biomaterial was based on the olfactory receptor (OR) of *Drosophila melanogaster* and homology modelling was used to generate the 3D structure of these olfactory receptors. The binding pocket of OR and VOCs were identified using AutoDock VINA and the peptide for biomaterial was designed using Chimera builder. The final design of sensor was using Silicon nanowire as the

transducer. The voltage profile and current of the device was calculated using DFT-NEGF. The presence of the receptor and VOC-docked receptor shows modulation of the voltage profile and hence the current through the device, illustrating the sensing mechanism. Here, future work can be

- a. Design of transducers compatible with olfactory receptors.
- b. Synthesis of peptide and making an actual OR-sensor to detect VOCs.

Understanding Olfaction is a difficult but important problem from a technological as well as a scientific point of view. The sophistication of the olfactory systems of polar bears, dogs, or fruit flies compels us to understand the dynamics of the system as a whole. However, there is only so much that theory can do, especially when our interest is to realize the one environment that can see different odorant molecules distinctly. The tools used in this thesis only form a part of the great problem but can help achieve the ultimate goal, mimicking a biological nose. The problem is interesting and full of potential and opportunities, so even with little understanding of the system as a whole, we will continue to solve the problems we can.

Bibliography

- [1] A. G. Bell, “Pamphlet by Alexander Graham Bell,” *Library of Congress*, 1914.
- [2] G. M. Dyson, “The scientific basis of order,” *J. Chem. Technol. Biotechnol.* vol. 57, pp. 647-651, 1938.
- [3] L. Pauling, “Molecular architecture and Biological Reactions,” *Chem. Eng. News*, vol. 24, no. 10, pp. 1375-77, 1946.
- [4] L. Turin, “A spectroscopic mechanism for primary olfactory reception,” *Chemical Senses*, Volume 21, Issue 6, pp. 773–791, 1996. doi: <https://doi.org/10.1093/chemse/21.6.773>
- [5] P. Ball, “Physics of life: The dawn of quantum biology,” *Nature* 474, pp. 272-274, 2011. doi: <https://doi.org/10.1038/474272a>
- [6] M. Saberi, H. Seyed-Allaei, “Odorant receptors of drosophila are sensitive to the molecular volume of odorants,” *Sci. Rep.* vol. 6, 25103, 2016. doi: <https://doi.org/10.1038/srep25103>
- [7] E. Block, et al., “Implausibility of the vibrational theory of olfaction,” *PNAS*, vol. 112, pp. E2766–E2774, 2015. doi: <https://doi.org/10.1073/pnas.1503054112>
- [8] A. Keller, L. B. Vosshall, “A psychophysical test of the vibration theory of olfaction,” *Nat. Neurosci.* 7, pp. 337-338, 2004. doi: <https://doi.org/10.1038/nn1215>
- [9] M. I. Franco, L. Turin, A. Mershin, E. M. C. Skoulakis, “Molecular vibration-sensing component in drosophila melanogaster olfaction,” *PNAS*, vol. 108, pp. 3797–3802, 2011. doi: <https://doi.org/10.1073/pnas.1012293108>
- [10] L. Haffenden, V. Yaylayan, J. Fortin, “Investigation of vibrational theory of olfaction with variously labelled benzaldehydes,” *Food Chem.* vol. 73, pp. 67–72, 2001. doi: [https://doi.org/10.1016/S0308-8146\(00\)00287-9](https://doi.org/10.1016/S0308-8146(00)00287-9)

- [11] B. R. Havens, C. E. Meloan, "The application of deuterated sex pheromone mimics of the American cockroach (*periplaneta americana*, l.), to the study of wright's vibrational theory of olfaction," *Developments in Food Science*, vol. 37, pp. 497–524, 1995. doi: [https://doi.org/10.1016/S0167-4501\(06\)80176-7](https://doi.org/10.1016/S0167-4501(06)80176-7)
- [12] R. R. Togunov, A. E. Derocher, N. J. Lunn, "Windscapes and olfactory foraging in a large carnivore," *Scientific Reports*, vol. 7, 46332, 2017. doi: <https://doi.org/10.1038/srep46332>
- [13] M. A. Craven, J. W. Gardner, P. N. Bartlett. "Electronic noses-development and future prospects." *TrAC Trends in Analytical Chemistry*, vol. 15, no. 9, pp. 486–493, 1996. doi:10.1016/S0165-9936(96)00061-1.
- [14] D. Karakaya, O. Ulucan, M. Turkan, "Electronic Nose and Its Applications: A Survey", *International Journal of Automation and Computing* 17(2), pp. 179-209, 2020. doi:10.1007/s11633-019-1212-9
- [15] Beghi, et al, "Electronic nose and visible-near infrared spectroscopy in fruit and vegetable monitoring" *Reviews in Analytical Chemistry*, vol. 36, no. 4, 2017, pp. 20160016. doi: <https://doi.org/10.1515/revac-2016-0016>
- [16] S. Kesarwani, A. Mahajan and S. Ganguly, "IETS in MIS Contacts: Towards a Quantum Biomimetic Electronic Nose," 2018 IEEE SENSORS, New Delhi, India, 2018, pp. 1-4, doi: 10.1109/ICSENS.2018.8589860.
- [17] M. Reed, "Inelastic Electron Tunneling Spectroscopy", *Materials today*, pp. 46-50, 2008. doi: [https://doi.org/10.1016/S1369-7021\(08\)70238-4](https://doi.org/10.1016/S1369-7021(08)70238-4)
- [18] A. S. Barwich, "A Critique of Olfactory Objects", *Front Psychol.* vol. 10:1337, 2019. doi: 10.3389/fpsyg.2019.01337.
- [19] R. A. Dielenberg, I. S. McGregor, "Defensive behavior in rats towards predatory odors: a review", *Neurosci Biobehav Rev*, vol. 25, pp. 597–609, 2001. doi: [https://doi.org/10.1016/S0149-7634\(01\)00044-6](https://doi.org/10.1016/S0149-7634(01)00044-6)
- [20] E. Fischer, "Einfluss der Configuration auf die Wirkung der Enzyme", *Ber. Dtsch. Chem. Ges.*, 27 (3), pp. 2985-2993, 1894. doi: <https://doi.org/10.1002/cber.18940270364>

- [21] R.W. Moncrieff, “The Chemical Senses” NY: John Wiley and Sons, 1944.
- [22] J. E. Amoore, J. W. Johnston Jr., M. Rubin, “The Stereochemical Theory of Odor”, *Sci. Am.* 210, pp. 42-49, 1964. doi: <http://www.jstor.org/stable/24936014>.
- [23] F. Yoshii, S. Hirono, I. Moriguchi, “Relations between the odor of (r)ethyl citronellyl oxalate and its stable conformations”, *Quantitative structure-activity relationships*, 13(2), pp. 144-147, 1994. doi: <https://doi.org/10.1002/qsar.19940130203>
- [24] S. Kim, J. Chen, T. Cheng, et al., “PubChem 2019 update: improved access to chemical data”, *Nucleic Acids Res.* vol. 47, pp. D1102–D1109, 2019. doi: [10.1093/nar/gky1033](https://doi.org/10.1093/nar/gky1033)
- [25] K. Mori, G. M. Shepard, “Emerging principles of molecular signal processing by mitral tufted cells in the olfactory bulb”, *Semin. Cell. Biol.*, pp. 65-74, 1994. doi: [10.1006/scel.1994.1009](https://doi.org/10.1006/scel.1994.1009)
- [26] J. C. Brookes, “A microscopic model of signal transduction mechanisms: olfaction”, Ph.D. Dissertation, Department of Physics and Astronomy, University College London, 2008. Available: <https://discovery.ucl.ac.uk/id/eprint/15786>
- [27] R. H. Wright, “Odor and molecular vibrations: neural coding of olfactory information”, *Journal of theoretical biology*, vol. 64, pp. 473-502, 1977. doi: [https://doi.org/10.1016/0022-5193\(77\)90283-1](https://doi.org/10.1016/0022-5193(77)90283-1)
- [28] P. P. C. Graziadei, Handbook of sensory physiology, Chemical Senses, part1, Olfaction, vol 4, New York Springer, 1971.
- [29] L.C. Briand, C. Eloit, V. Nespolos, J.-C. Huet, C. Henry, “Evidence of an odorant-binding protein in the human olfactory mucus: location, structural characterization, and odorant-binding properties”, *Biochemistry*, vol. 41, pp. 7241-7252, 2002. doi: <https://doi.org/10.1021/bi015916c>
- [30] L.B. Buck, “Unravelling the sense of smell”, Nobel Lecture, 2004. doi: [10.1002/anie.200501120](https://doi.org/10.1002/anie.200501120)
- [31] L. Buck and R. Axel, “A novel multi-gene family may encode odorant receptors” *Cell*, vol. 65, pp. 175-187, 1999. doi: [https://doi.org/10.1016/0092-8674\(91\)90418-X](https://doi.org/10.1016/0092-8674(91)90418-X).
- [32] R. R. Reed, “After the holy grail: Establishing a molecular basis for mammalian olfaction” *Review Cell*, vol. 116, pp. 329-336, 2004. doi: [10.1016/s0092-8674\(04\)00047-9](https://doi.org/10.1016/s0092-8674(04)00047-9).

- [33] Patrick J. Lynch, medical illustrator Available [File:Head olfactory nerve.jpg](#).
- [34] S. N. Narayanan, P. Shivappa, P., S. Padiyath, A. Bhaskar, Y. W. Li, T. H. Merghani, “The Prevalence and Pathophysiology of Chemical Sense Disorder Caused by the Novel Coronavirus,” *Frontiers in Public Health*, vol. 10, 2022. doi <https://doi.org/10.3389/fpubh.2022.839182>
- [35] NaNa Kang, JaeHyung Koo, “Olfactory receptors in non-chemosensory tissues,” BMB Reports, vol. 45, pp. 612-622, 2012. doi: <http://dx.doi.org/10.5483/BMBRep.2012.45.11>.
- [36] OpenWetWare, “BIO254: ORs”, 2006. Available: <https://openwetware.org/mediawiki/index.php?title=BIO254:ORs&oldid=86883>.
- [37] F. M. Simoes deSouza and G. Antunes, “Biophysics of olfaction,” *Reports on Progress in Physics*, vol. 70, pp. 451-491, 2007. doi: 10.1088/0034-4885/70/3/R04.
- [38] N. E. Rawson and M. G. Gomez, “Cell and molecular biology of human olfaction,” *Microscopy research and technique*, vol. 58, pp. 142-151, 2002. doi: [10.1002/jemt.10132](https://doi.org/10.1002/jemt.10132).
- [39] S. Kaczanowski, P. Zielenkiewicz, “Why similar protein sequences encode similar three-dimensional structures?” *Theoretical Chemistry Accounts*, vol. 125 (3–6), pp. 643–650, 2010. doi:[10.1007/s00214-009-0656-3](https://doi.org/10.1007/s00214-009-0656-3).
- [40] T. Fuchs, G. Glusman, S. HornSaban, D. Lancet, Y. Pilpel, “The human olfactory sub genome: from sequence to structure and evolution,” *Human genetics*, vol. 108, pp. 1-13, 2001. doi: 10.1007/s004390000436.
- [41] F. Ballante, A. J. Kooistra, S. Kampen, C. Graaf, J. Carlsson, “Structure-Based Virtual Screening for Ligands of G Protein-Coupled Receptors: What Can Molecular Docking Do for You?” *Pharmacol. Rev.* vol. 73, pp. 1698–1736, 2021. doi: <https://doi.org/10.1124/pharmrev.120.000246>.
- [42] A. Lewis and L. V. DelPrioire, “The biophysics of visual photoreception,” *Physics Today*, pp. 38-46, 1988. doi:10.1063/1.881152.
- [43] A. Szabo, N. S. Ostlund, Modern Quantum Chemistry: Introduction to advanced electronic structure theory. McGraw-Hill, Inc, 1989.
- [44] C. Cohen-Tannoudji, B. Diu and F. Laloe, Quantum Mechanics, John Wiley & Sons, New York, 1977.

- [45] A. M. Stoneham, Theory of defects in solids. Electronic structure of defects in insulators and semiconductors, Oxford University Press, 1975.
- [46] E. Estrada, Mathematical Tools for Physicists, Wiley-VCH, 2015.
- [47] S. Smidstrup et al., “QuantumATK: An integrated platform of electronic and atomic-scale modelling tools,” *J. Phys.: Condens. Matter*, vol. 32, no. 1, 015901, 2020. doi: 10.1088/1361-648X/ab4007
- [48] N. M. Harrison, An Introduction to Density Functional Theory, Department of Chemistry, Imperial College of Science Technology and Medicine, London. Available: https://www.imperial.ac.uk/media/imperial-college/research-centres-and-groups/computational-materials-science/teaching/DFT_NATO.pdf
- [49] D. J. Griffiths and D. F. Schroeter, *Introduction to Quantum Mechanics*, 3rd ed. Cambridge: Cambridge University Press, 2018.
- [50] P. Hohenburg and W. Kohn, “Inhomogeneous Electron Gas,” *Phys. Rev.* 1 vol. 36, pp. B864-71, 1964. doi: <https://doi.org/10.1103/PhysRev.136.B864>.
- [51] D. Turner, P. Willetta, A. M. Ferguson, T. W. Heritage, “Evaluation of a novel molecular vibration-based descriptor (EVA) for QSAR studies: 2. Model validation using a benchmark steroid dataset,” *J. Comput. Aided Mol. Des.* 13, pp. 271–296, 1999. doi: 10.1023/a:1008012732081.
- [52] R. M. Khan, et al. “Predicting Odor Pleasantness from Odorant Structure: Pleasantness as a Reflection of the Physical World.”, *J. Neurosci.* vol. 27, pp. 10015-10023, 2007. doi: <https://doi.org/10.1523/JNEUROSCI.1158-07.2007>
- [53] R. Todeschini, V. Consonni, Handbook of Molecular Descriptors, Wiley-VCH, Weinheim (Federal Republic of Germany), 2000.
- [54] The Good Scents Company - Flavor, Fragrance, Food And Cosmetics Ingredients Information. Available: <http://thegoodscentscompany.com/>.
- [55] F. Hamdache, G. Vergoten, P. Lagant, A. Benosman, “Normal Modes Calculation for Benzene in a Local Symmetry Force Field,” *J. RAMAN SPECTROSC.* vol. 20, pp. 297-301, 1989. doi:[10.1002/JRS.1250200505](https://doi.org/10.1002/JRS.1250200505)

- [56] P. Durlak, S. Berski, Z. Latajka, “Theoretical studies on the molecular structure, conformational preferences, topological and vibrational analysis of allicin,” *Chem. Phys. Lett.* vol. 644, pp. 5-13, 2016. doi:[10.1016/j.cplett.2015.11.038](https://doi.org/10.1016/j.cplett.2015.11.038)
- [57] D. B. Turner, P. Willett, “The EVA Spectral Descriptor,” *Eur. J. Med. Chem.* vol. 35, pp. 367–375, 2000. doi: [https://doi.org/10.1016/S0223-5234\(00\)00141-0](https://doi.org/10.1016/S0223-5234(00)00141-0).
- [58] A. Banerjee, “The Spectrum of the Graph Laplacian as a Tool for Analyzing Structure and Evolution of Networks,” Ph.D. Dissertation, Max Planck Institute for Mathematics in the Sciences, University of Leipzig, Germany, 2008. Available: https://www.iiserkol.ac.in/~anirban.banerjee/Banerjee_PhD_Thesis.pdf
- [59] P. Patil, “Design and fabrication of electron energy filters for room temperature inelastic electron tunneling spectroscopy,” Master’s thesis, Massachusetts Institute of Technology, Cambridge, 2013. Available: <http://cba.mit.edu/docs/theses/13.09.Patil.pdf>.
- [60] A. Patil, D. Saha, D. S. Ganguly, “A Quantum Biomimetic Electronic Nose Sensor,” *Sci. Rep.* vol. 8, 128, 2018. doi: <https://doi.org/10.1038/s41598-017-18346-2>.
- [61] IR Spectrum Table & Chart, Sigma-Aldrich
Available: <https://www.sigmaaldrich.com/technical-documents/articles/biology/ir-spectrum-table.html>
- [62] Origin 2019b, OriginLab Corporation, Northampton, MA, USA.
- [63] U. V. Luxburg, “A tutorial on spectral clustering,” *Stat. Comput.* 17, pp. 395-416, 2007.
- [64] S. Takane, J. B. O. Mitchell, “A structure-odour relationship study using EVA descriptors and hierarchical clustering,” *Org. Biomol. Chem.* 2, pp. 3250–3255, 2004. doi: <https://doi.org/10.1039/B409802A>.
- [65] Chirality and Optical Activity. Available: <http://chemed.chem.psu.edu/genchem/topicreview/bp/1organic/chirality.html>.
- [66] E. U. Condon. “Theories of Optical Rotatory Power,” *Reviews of Modern Physics* 9.4, pp. 432–457, 1937. doi:<https://doi.org/10.1103/RevModPhys.9.432>.
- [67] Tatyana Karabencheva, Christo Christov, “Mechanisms of protein circular dichroism: insights from computational modelling,” *Advances in Protein Chemistry and Structural Biology*, Academic Press, Volume 80, 2010, ch. 3, pp.85-115. doi: <https://doi.org/10.1016/B978-0-12-381264-3.00003-5>

- [68] Ronald Bentley, “The Nose as a Stereochemist. Enantiomers and Odor,” *Chem. Rev.* 106, 9, pp. 4099–4112, 2006. doi:10.1021/cr050049t.
- [69] J. Chela-Flores, “The origin of chirality in protein amino acids,” *Chirality*, vol. 6, pp. 165-168, 1994. doi: <https://doi.org/10.1002/chir.530060302>
- [70] Kiss W. Mwamwitwa et al., “A retrospective cross-sectional study to determine chirality status of registered medicines in Tanzania,” *Scientific Reports*, vol. 10, 17834, 2020. Doi <https://doi.org/10.1038/s41598-020-74932-x>.
- [71] Karen Michaeli, Nirit Kantor Uriel, Ron Naaman and David H. Waldeck, “The electron's spin and molecular chirality –how are they related and how do they affect life processes?” *Chem. Soc. Rev.* 45, pp. 6478-6487, 2016. doi:10.1039/C6CS00369A.33
- [72] G. Dresselhaus. “Spin-Orbit Coupling Effects in Zinc Blende Structures,” *Physical Review* vol. 100, issue 2, pp. 580–586, 1955. doi: <https://doi.org/10.1103/PhysRev.100.580>
- [73] Y. A. Bychkov and E. I. Rashba, “Properties of a 2D electron gas with lifted spectral degeneracy,” *P. Zh. Eksp. Teor. Fiz.*, vol. 39, p. 66, 1984.
- [74] R. Gutierrez, E. Díaz, R. Naaman, and G. Cuniberti, “Spin-selective transport through helical molecular systems,” *Phys. Rev. B* 85, 081404(R), 2012.
- [75] B. Gohler et al. “Spin Selectivity in Electron Transmission Through Self-Assembled Monolayers of Double-Stranded DNA”. *Science* 331.6019, pp. 894–897, 2011.
- [76] Zouti Xie et al. “Spin Specific Electron Conduction through DNA Oligomers,” *NanoLetters*, pp. 4652–4655, 2011.
- [77] R. Naaman, Y. Paltiel, and D. H. Waldeck, “Chiral molecules and the electron spin.” *Nat. Rev. Chem* 3, pp. 250–260, 2019. doi: <https://doi.org/10.1038/s41570-019-0087-1>
- [78] Ernesto Medina et al. “Continuum model for chiral induced spin selectivity in helical molecules”. *The Journal of Chemical Physics* 142.19(2015), p. 194308. doi:10.1063/1.4921310
- [79] M.P. Rebergen, “A Study of Induced Spin Selectivity in Chiral Molecules,” M. S. Thesis, Delft University of Technology, 2018. Available: <http://repository.tudelft.nl/>.
- [80] Konrad Patkowski. “Recent developments in symmetry-adapted perturbation theory”. *WIREs Computational Molecular Science* 10.3, e1452, 2020. doi: <https://doi.org/10.1002/wcms.1452>.

- [81] S. Datta, Electronic Transport in Mesoscopic Systems. first. Cambridge University Press, 1995.
- [82] S. Datta, Lessons from Nanoelectronics: A New Perspective on Transport Vol. 1, World Scientific, Singapore, 2012.
- [83] Tao Ji, “Inelastic Electron Tunneling Spectroscopy in Molecular Electronic Devices from First-Principles,” Ph.D. Dissertation, Centre for the Physics of Materials, Department of Physics McGill University, Canada, 2010. Available: <https://escholarship.mcgill.ca/concern/theses/w9505091b>.
- [84] N. Pandey, D. Pal, D. Saha, and S. Ganguly, “Vibration-based biomimetic odor classification” *Sci Rep* 11, 11389, 2021.
- [85] Leffingwell and associates. Available: <http://www.leffingwell.com>
- [86] A. C. Aragonès et al., “Measuring the Spin-Polarization Power of a Single Chiral Molecule.” *Small* 13, 2017.
- [87] Anup Kumara et al., “Chirality-induced spin polarization places symmetry constraints on biomolecular interactions,” *PNAS* vol. 114, no. 10, pp. 2474–2478, 2017. doi: <https://doi.org/10.1073/pnas.1611467114>
- [88] Daniel G. A. Smith et al., “PSI4 1.4: Open-source software for high-throughput quantum chemistry,” *J. Chem. Phys.* 152, 184108, 2020.
- [89] Esmer Jongedijk et. al. “Biotechnological production of limonene in microorganisms”. English. *Applied Microbiology and Biotechnology* 100.7, pp. 2927–2938, 2016. doi:10.1007/s00253-016-7337-7
- [90] Luca Turin and Fumiko Yoshii, “Structure-odor relations: A modern perspective,” Handbook of Olfaction and Gustation, 2003.
- [91] S. Datta, Quantum Transport: Atom to Transistor. Cambridge University Press, 2005.
- [92] M. D. Hanwell et al., “Avogadro: an advanced semantic chemical editor, visualization, and analysis platform,” *J. Cheminform* 4, 17, 2012.
- [93] R. Naaman, Y. Paltiel, and D. H. Waldeck. “Chiral Molecules and the Spin Selectivity Effect,” *The Journal of Physical Chemistry Letters* 11.9, pp. 3660–3666, 2020. doi:10.1021/acs.jpclett.0c00474

- [94] A. U. Alam, P. Rathi, H. Beshai, G. K. Sarabha, M. J. Deen, “Fruit Quality Monitoring with Smart Packaging,” *Sensors* 21(4), 1509, 2021. DOI; <https://doi.org/10.3390/s21041509>.
- [95] J. Zhu, K. Park, and T. C. Baker, “Identification of odors from overripe mango that attract vinegar flies, *Drosophila melanogaster*,” *Journal of Chemical Ecology* 29(4), pp. 899-909, 2003.
- [96] Shikha Tiwari, Adinath Kate, Debabandya Mohapatra, Manoj Kumar Tripathi, et. al., “Volatile organic compounds (VOCs): Biomarkers for quality management of horticultural commodities during storage through e-sensing,” *Trends in Food Science & Technology* 106, pp. 417-433, 2020.
- [97] Haocheng Liu, et. al., “Aromatic Characterization of Mangoes (*Mangifera indicaL.*) Using Solid Phase Extraction Coupled with Gas Chromatography–Mass Spectrometry and Olfactometry and Sensory Analyses,” *Food* 9(1), 75, 2020.
- [98] F. Scolari, F. Valerio, G. Benelli, et. al., “Tephritid Fruit Fly Semiochemicals: Current Knowledge and Future Perspectives,” *Insects*, 12(5), pp. 408, 2021. doi: 10.3390/insects12050408.
- [99] Elissa A. Hallem¹ and John R. Carlson¹, “Coding of Odors by a Receptor Repertoire,” *Cell* 125, 2006.
- [100] Flavio Ballante, Albert J Kooistra, Stefanie Kampen, Chris de Graaf, and Jens Carlsson, “Structure-Based Virtual Screening for Ligands of G Protein–Coupled Receptors: What Can Molecular Docking Do for You?” *Pharmacol Rev* 73, pp. 1698–1736, 2021.
- [101] A. J. M. Barbosa, A. R. Oliveira, A. C. A. Roque, “Protein- and Peptide-Based Biosensors in Artificial Olfaction,” *Trends Biotechnol.* vol. 36, issue 12, pp. 1244-1258, 2018. doi: 10.1016/j.tibtech.2018.07.004.
- [102] J. Jumper, et al., “Highly accurate protein structure prediction with AlphaFold,” *Nature* 596, pp. 583–589, 2021.
- [103] O. Trott, A. J. Olson, “AutoDock Vina: improving the speed and accuracy of docking with a new scoring function, efficient optimization and multithreading,” *Journal of Computational Chemistry* 31, pp. 455-461, 2019.

- [104] S. Yuan, T. Dahoun, M. Brugarolas, *et al.*, "Computational modeling of the olfactory receptor Olfr73 suggests a molecular basis for low potency of olfactory receptor-activating compounds," *Commun Biol* 2, 141, 2019. doi: <https://doi.org/10.1038/s42003-019-0384-8>
- [105] Enade P. Istyastono, Muhammad Radifar, N. Yuniarti, V. D. Prasasty, and S. Mungkasi, "PyPLIF HIPPOS: A Molecular Interaction Fingerprinting Tool for Docking Results of AutoDock Vina and PLANTS," *Journal of Chemical Information and Modeling* 60 (8), pp. 3697-3702, 2020. DOI: 10.1021/acs.jcim.0c00305
- [106] A. Wasfi, F. Awwad, J. G. Gelovani, N. Qamhieh, and A. I. Ayesh, "COVID-19 Detection via Silicon Nanowire Field-Effect Transistor: Setup and Modeling of Its Function," *Nanomaterials*, vol. 12, no. 15, p. 2638, Jul. 2022, doi: 10.3390/nano12152638. [Online]. Available: <http://dx.doi.org/10.3390/nano12152638>.
- [107] T. Z. Wu, Y. R. Lo, "Synthetic peptide mimicking of binding sites on olfactory receptor protein for use in 'electronic nose'," *J Biotechnol.* vol. 80, issue 1, pp. 63-73, 2000. doi: 10.1016/s0168-1656(00)00228-5.
- [108] E. F. Pettersen, et. al., "UCSF Chimera--a visualization system for exploratory research and analysis," *J Comput Chem.* 25(13), pp. 1605-12, 2004.
- [109] P. R. Nair and M. A. Alam, "Design Considerations of Silicon Nanowire Biosensors," in *IEEE Transactions on Electron Devices*, vol. 54, no. 12, pp. 3400-3408, 2007, doi: 10.1109/TED.2007.909059.
- [110] Salman Seyedi et. al., "Screening of Coulomb interactions in liquid dielectrics" *J. Phys.: Condens. Matter* 31, 325101, 2019.